Struct Bond (2018) 178: 91–154
DOI: 10.1007/430_2018_24

Characterization of Metal Centers in Zeolites for Partial Oxidation Reactions

G. Berlier, V. Crocellà, M. Signorile, E. Borfecchia, F. Bonino, and S. Bordiga

Abstract This chapter addresses the power and possibilities provided by an appropriate combination of advanced characterization techniques in understanding the environment of metal ions in different metal-zeolites, as well as in the role played by them in different catalytic reactions. Three different classes of materials are considered as case studies: (1) Cu-zeolites, where Cu^{I} and Cu^{II} ions are mainly present as counterions; (2) Fe-zeolites, often containing a wide variety of isolated, oligonuclear, and aggregated (oxide/hydroxide) Fe^{II}/Fe^{III} species; and (3) TS-1, which is the closest to a "single-site" catalyst, mainly containing framework Ti^{IV} sites. TS-1 is studied in relation to its activity in the propene epoxidation reaction in the presence of aqueous H_2O_2, while Cu- and Fe-zeolites are here considered in relation to the direct conversion of methane to methanol (MTM) (a so-called dream reaction) with O_2, N_2O, or H_2O_2 as oxidizing agents. Main focus is into the nature of the active site precursors (i.e., mono or di-/trinuclear ions, oxidation state, and local environment) and into the electronic and geometric structure of the oxo species formed upon interaction with the oxidizing agents. Moreover, examples about in situ or operando experiments following changes during the reaction are reviewed. The main considered techniques are X-ray absorption spectroscopy (XAS) and resonance Raman (rR) and diffuse reflectance UV-Vis spectroscopies, often coupled to density functional theory (DFT) modeling. Depending on the studied system, results obtained with infrared, Mössbauer, X-ray emission (XES) and electron paramagnetic resonance (EPR) spectroscopies are also described. The discussion includes the open debates, the main drawbacks and potentialities of the techniques, and the related characterization challenges.

G. Berlier, V. Crocellà, M. Signorile, E. Borfecchia, F. Bonino, and S. Bordiga (✉)
Department of Chemistry, INSTM Reference Center, and NIS Inter-Departmental Centre,
University of Turin, Turin, Italy
e-mail: silvia.bordiga@unito.it

Keywords Benzene to phenol · Cu-zeolites · Diffuse reflectance UV-Vis spectroscopy · Fe-zeolites · Hydrogen peroxide · In situ spectroscopy · Infrared spectroscopy · Methane to methanol · Operando techniques · Propylene to propylene oxide · Resonance Raman spectroscopy · Selective oxidation · Ti-silicalite-1 · X-ray absorption spectroscopy

Contents

1 Introduction

1.1 Transition Metal Ions in Zeolites

Metal centers in zeolites for partial oxidation reactions are usually transition metal ions (TMIs) with redox activity, which can be introduced as counterions by chemical vapor deposition/impregnation (CVD/CVI) and liquid or solid ion exchange (LIE or SSIE). These procedures are often carried out on H^+- or NH_4^+-zeolites, where the TMIs exchange for Brønsted acid sites (which in NH_4^+-zeolite are generated by thermal treatment with consequent NH_3 release) or on Na^+ (or other alkaline/alkaline earth metal ions) zeolites. Alternatively, TMI can be directly inserted during the synthesis into framework positions, resulting into neutral frameworks in the case of tetravalent ions (as for Ti^{IV} in TS-1) or in negatively charged frameworks usually compensated by protons or other cations in the case of trivalent ions as in the case of Fe^{III} in Fe-zeolites. This TMI incorporation within frameworks is usually found in MeAlPO zeotypes, where redox-active TMIs can be easily and reversibly converted between the +2 and +3 oxidation state (as in the case of CoAlPO, MnAlPO, FeAlPO, etc. [1–4]) depending on the activation treatment. This also implies the generation of

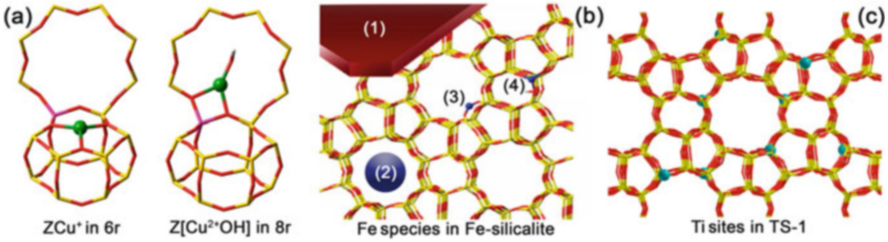

Fig. 1 Examples of possible transition metal ion (TMI) location and structures in different zeolites active in selective oxidation reactions. (**a**) Metals introduced as counterions by ion exchange: density functional theory (DFT)-optimized structures of Cu^I and $[CuOH]^+$ sites stabilized by one negative framework charge (Z) in the 6r and 8r units of CHA framework (Cu in green, Si in yellow, O in red, Al in pink, H in white). (**b**) Variety of species observed in thermally treated Fe-silicate samples: (1) Fe_2O_3 particles on the zeolite external surface, (2) Fe_xO_y clusters, (3) grafted Fe^{II} dispersed in the pores, and (4) framework Fe^{III} (Fe in blue, O in red, Si in yellow). Reproduced from [10] with permission from the PCCP Owner Societies. (**c**) Representation of the isomorphous substitution of Si atoms of MFI framework by Ti^{IV} in TS-1 (Ti in light blue, O in red, Si in yellow)

Brønsted acid sites when the TMI is reduced to the divalent state. This class of materials is extensively discussed in this book in the chapter by Sankar and will thus not be addressed hereafter. It is only important to mention that the reactivity of TMIs introduced as heteroatoms in zeolites is different with respect to what has been observed in AlPOs. Namely, Ti^{IV} in TS-1 is stable in framework positions and cannot be reduced to Ti^{III} (at variance with what observed in TiAlPO-5 [5–8]), while Fe^{III} is not stable as heteroatom and moves to extraframework positions generating a variety of Fe^{II}/Fe^{III} species during thermal treatments, as extensively discussed in Sect. 3 [9, 10].

In this contribution, we will thus mainly deal with Cu-exchanged zeolites, which are being deeply investigated in recent years for the direct conversion of methane to methanol (MTM) using O_2 as oxidizing agent, and with Fe-zeolites (both prepared by direct synthesis and ion exchange) which are instead active in the same reaction using N_2O or H_2O_2. Moreover, a section will be devoted to TS-1, which is active in selective partial oxidation reactions (e.g., in the epoxidation of propylene) using H_2O_2 as oxidizing agent. Examples of possible location and structures of TMI ions in the three different case studies are shown in Fig. 1.

1.2 Main Characterization Techniques

Usually, the routine characterization of this class of zeolite-based catalysts includes textural and structural properties (specific surface area, porosity, and crystallinity). Moreover, X-ray diffraction (XRD) can be also employed to assess the positions of counterions into the zeolite channels and pores or reticular positions. However, in this chapter, we will mainly focus on the characterization results concerning the structure and properties of the redox-active centers, which are usually studied by spectroscopic techniques. Namely, these are diffuse reflectance UV-Vis (for information on the TMI oxidation state and ligand symmetry); X-ray absorption and emission (oxidation state and geometry, detailed information on the shells of ligands surrounding the metal center); Raman, also in resonance mode (nature of oxo moieties); and infrared (mainly indirect information on oxidation, coordination, and nuclearity by using probe molecules).

To give a realistic description of the active sites during the reaction, these techniques are often used in operando or in situ conditions. These approaches represent the current frontier for the application of spectroscopic techniques, since their goal is the characterization of the catalytic system while chemical reaction/ transformations are occurring (i.e., calling for a significant time resolution). Furthermore, the complexity of the reaction environment (potentially aggressive chemicals are present; high temperature and/or pressure is requested) leads to the development of specific spectroscopic setups able to deal with it. Despite such difficulties, in situ and operando approaches open to valuable information, poorly accessible through conventional methods: some relevant examples will be given along this chapter. Information on the metal ions' redox properties and activity obtained by different techniques, such as electron paramagnetic resonance (EPR) and Mössbauer spectroscopies, will be also mentioned, where relevant.

For more details about the concepts, experimental setups, and issues related to the use of spectroscopies in operando or in situ conditions, readers are referred to [11–14] (DR UV-Vis), [11, 13–17] (Raman), [11, 14, 18] (XAS), and [17, 19, 20] (infrared).

2 Transition Metal Ion-Exchanged Zeolites for Direct Conversion of Methane to Methanol

The direct conversion of MTM represents an important challenge among partial oxidation reactions. This can be considered as a "dream reaction," in relation to the higher chemical inertness of the reactant with respect to the product [21]. Indeed, methane is a symmetric molecule, without low-energy empty orbitals and high-energy filled ones, and is characterized by the highest C-H bond energy among hydrocarbons (413 kJ mol^{-1}). On the contrary, methanol is characterized by a significant dipole moment, and it interacts more easily with available active sites on the catalysts. Thus, kinetic protection or selective separation of the product is necessary to avoid over-oxidation [22]. Moreover, if molecular oxygen is selected as the oxidant, several fundamental issues are encountered: (1) O_2 is a four-electron oxidant that needs to be used as a two-electron one; (2) the reaction has an unbalanced stoichiometry – there is one extra oxygen atom for each molecule of methanol produced; (3) since CH_4 and CH_3OH possess singlet ground states, the reaction is spin forbidden when O_2 is used as terminal oxidant, the so-called spin dilemma [23].

The current industrial process for methane conversion is based on steam reforming to form syngas (a CO/H_2 mixture), which is then converted to methanol.

This two-step process is demanding in terms of energy supply, materials, and technology, due to the high temperature and pressure required. A more direct and less energy-intensive conversion of MTM is thus desirable, particularly to exploit methane where it is naturally abundant. Based on recent estimations, 140 billion cubic meters of methane (approximately 1/3 of the annual methane consumption of Europe) per year are flared or vented into our planet atmosphere [24]. This is not only a waste, but has also a tremendous effect on climate change, considering that methane has a global warming potential 20 times higher than CO_2. Its direct conversion on-site into liquid methanol, an important feedstock for the chemical industry (more than 48 million tonnes produced yearly [25]), would also solve the safety and cost issues related to storage and transport.

In this context, in 2005 medium and large pore Cu-exchanged zeolites (MFI and MOR) were first shown to be able to form methanol upon methane adsorption on samples pretreated in O_2 by Groothaert et al. [26]. Many other reports followed about Cu-zeolite materials, which will be reviewed hereafter. However, it is worth to mention that other TMI containing zeolites were proposed for the same reaction. Namely, Fe-containing zeolites were shown to catalyze the MTM conversion when using N_2O as oxidizing agent, since the pioneering work by Panov and coworkers [27–29]. However, in this case, the interest moved to the application of the same materials in the N_2O-mediated benzene to phenol conversion, due to the difficulties related to methanol extraction from the catalysts' surface [30, 31]. More recently, the same materials were shown to be able to partially oxygenate methane at low temperature with H_2O_2 [32]. In this case, Cu^{II} ions were added to Fe-MFI systems to avoid over-oxidation and obtain 90% selectivity to methanol. Other examples of TMI-containing zeolites for the methane oxidation with O_2 include Co-ZSM-5 [33, 34] and Ni-ZSM-5 [35]. In the following paragraphs, the main results discussed in the literature about the characterization of active sites or active site precursors in Cu-zeolites will be discussed.

2.1 Cu-Zeolites with O_2 as Oxidizing Agent: The Starting Point

The first report about the potentiality of Cu-exchanged zeolites in the selective oxidation of methane appeared in 2005 [26]. In their short communication, Groothaert et al. studied the reactivity of methane on an O_2-activated Cu-ZSM-5 sample (MFI framework, Cu/Al = 0.6, Si/Al = 12). Low-temperature (125°C) CH_4 dosage resulted in the formation of methanol, which was extracted from the catalysts' surface in a solvent mixture. The intensity of the UV-Vis band at 22,700 cm^{-1}, which is peculiar of the O_2-activated Cu-ZSM-5 samples [36, 37], was shown to decrease upon methane exposure (Fig. 2a), and a correlation between the intensity of this band in samples with different Cu content and their methanol productivity was also reported. Moreover, Cu-MOR (Si/Al = 9, Cu/Al = 0.43) which is characterized

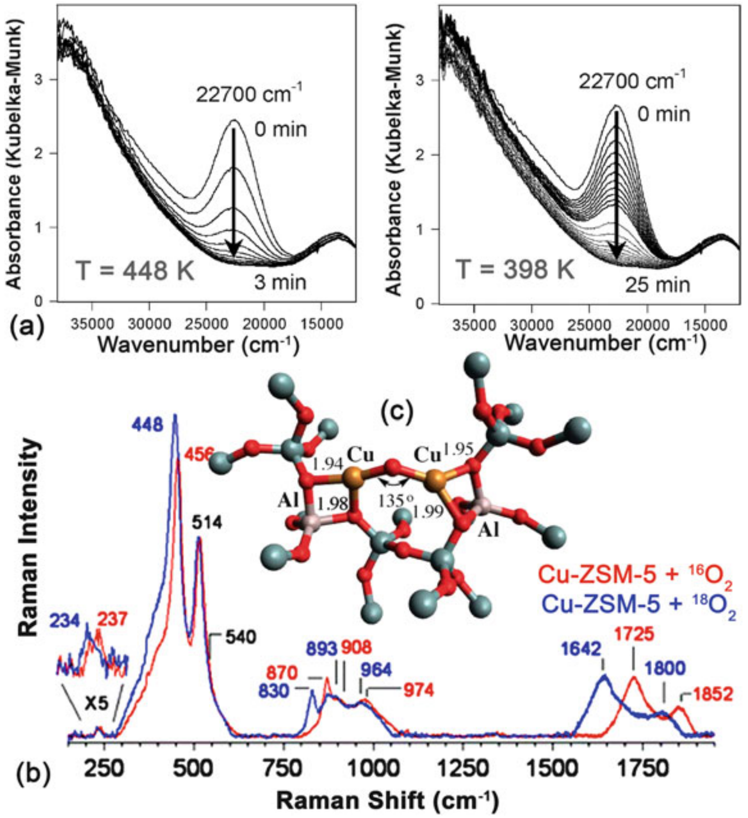

Fig. 2 Spectroscopic fingerprints and proposed structure of copper cores in O_2-activated Cu-ZSM-5: (**a**) UV-Vis fingerprint at 22,700 cm^{-1}, evolving during CH_4 contact at different temperatures. Adapted with permission from [26]. Copyright 2015 American Chemical Society. (**b**) rR spectra in the presence of $^{16}O_2$ (red) and $^{18}O_2$ (blue). Adapted from the Journal of Catalysis, vol 284, P. Vanelderen et al., Cu-ZSM-5: A biomimetic inorganic model for methane oxidation, 157–164, Copyright 2011, with permission from Elsevier [38]. (**c**) DFT-optimized model for the mono(μ-oxo)dicopper core (Cu atoms in yellow, Si atoms in gray, Al atoms in white, O atoms in red). Reprinted with permission from [39]. Copyright 2014 American Chemical Society

by an intense band at 22,200 cm^{-1} when oxidized resulted in even higher methanol yield with respect to Cu-ZSM-5, at variance with inactive Cu-Y and Cu-silica [26].

On these bases, the UV-Vis feature at 22,700–22,200 cm^{-1} was proposed as a fingerprint of the active Cu-oxo precursors. The structural assignment of the spectroscopic feature was based on the comparison with thoroughly characterized Cu cores in enzyme and synthetic models, with the support of EPR and XAS results [40]. More in detail, a Cu-Cu second shell distance ~2.86 Å was measured by EXAFS in a series of Cu-ZSM-5 samples with a Cu/Al ≅ 0.6 (Si/Al = 12 and 31). This was compared with the same parameter in bis(μ-oxo)dicopper $[Cu_2(\mu\text{-}O)_2]^{2+}$

cores in synthetic model complexes [41, 42] and with the (μ-η^2:η^2-peroxo)dicopper $[Cu_2(\mu\text{-}\eta^2\text{:}\eta^2\text{-}O_2)]^{2+}$ active sites in proteins (hemocyanin, tyrosinase, and catechol oxidase) [43] and in synthetic models [44]. The Cu-Cu distance in both planar and bent (μ-η^2:η^2-peroxo)-dicopper complexes was found to be higher with respect to that measured in Cu-ZSM-5 (3.2–3.8 vs 2.79–2.92 Å), pointing to the presence of the bis(μ-oxo)dicopper core (2.73–2.91 Å) in the zeolite. This was found to be in agreement with the spectroscopic features of the synthetic complexes (particularly a relatively intense band in the 22,300–25,000 cm^{-1} range) and with a negative correlation with the EPR signal intensity. The latter was explained on the basis of ab initio calculations indicating a singlet ground state for the bis(μ-oxo)dicopper (structure **A** in Scheme 1) [42].

Notwithstanding the similarities of spectroscopic features and structural parameters described above, the presence of bis(μ-oxo)dicopper cores in Cu-ZSM-5 still presented some weaknesses/inconsistencies. First, the oxidation state indicated by XANES data was found to be lower than the formal Cu^{III} expected for the bis(μ-oxo) dicopper cores (four electrons would need to be transferred from the O_2 ligand to Cu^I ions during the oxidation treatment), and this was explained by the twofold coordination of framework oxygen ligands, carrying a negative charge. Moreover, the authors clearly stated that the resulting XAS data were averaging a mixture of both dicopper and monomeric Cu sites, so that the measured Cu-O coordination number of 4.5 was explained with a mixture of fourfold-coordinated Cu ions in the bis (μ-oxo)dicopper cores (two O ligands from O_2 and two from the framework) and fivefold-coordinated monomeric Cu^{II} ions [40]. Even if there are examples in the literature about metal ions coordinated by several of the O atoms forming the zeolite rings, this explanation is somewhat doubtful for Cu^{II} ions in ZSM-5. Indeed, these were shown to be able to accommodate up to three CO ligands, suggesting a highly unsaturated coordination sphere [37]. Also, even if the authors addressed this aspect by invoking the probability of having short-distance Al-Al pairs ($r < 5.5$ Å) in ZSM-5 even at high Si/Al ratio, this seems highly unlikely in a sample with

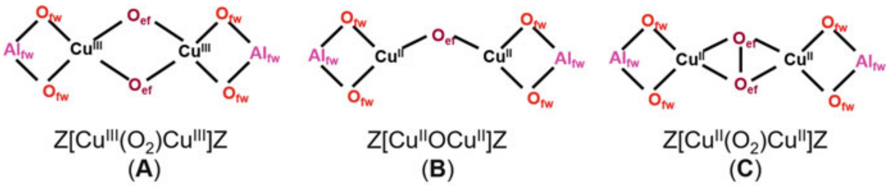

Scheme 1 Binuclear structures proposed as active sites in Cu-ZSM-5. Al_{fw} and O_{fw} represent Al and O framework atoms, respectively, generating a negative charge which stabilizes the positively charged Cu counterions. O_{ef} indicates extraframework oxygen atoms, resulting from the interaction with O_2. (**A**), bis(μ-oxo)dicopper core proposed in [26]; (**B**), mono(μ-oxo)dicopper core proposed in [45]; (**C**), μ-(μ^2:μ^2)peroxodicopper core [46]. The displayed charge of the Cu counterions has been calculated assuming an overall neutral structure, considering −2 as formal charge for μ-oxo ligands and −1 for the peroxo one (see Sect. 2.2 for comments about the alleged Cu^{III} ions in structure **A**).

Si/Al = 31, which showed the same (or similar) UV-Vis and XAS features as described above [47].

One of the main problems in establishing the nature of active sites in catalysis is related to the “single-site” issue, in that most catalysts are often characterized by a variety of sites with different coordination number, ligand geometry, and nuclearity. This implies the intrinsic difficulty in discriminating active sites from “spectators.” This also holds for metal-exchanged zeolites, even if they can be often considered as model systems, due to the fact that TMIs are easily stabilized as counterions and many structural information can be found in the literature about their location in the zeolite channels and cavities (see, for instance, [48, 49]). In this case, the distribution of TMIs is affected by the zeolite topology and chemical composition, that is, Me/Al and Si/Al ratios. The influence of chemical composition on the distribution (and redox behavior) of Cu ions in the CHA framework has been recently addressed by Paolucci et al. in the field of the selective catalytic reduction (SCR) of NO_x [50]. The same authors demonstrated that, under reaction conditions in Cu-CHA, multinuclear sites are reversibly formed from mobilized single atoms. This implies that in SCR reaction, the Cu-zeolite cannot be considered as a “single-site catalyst.” Moreover, the authors pointed out that the dynamic of Cu ions “falls outside the conventional boundaries of a heterogeneous or homogeneous catalyst” [51]. Even if these works focus on a different reaction, they clearly indicate the difficulty in pinpointing the “true” active sites in complex systems, so that a multi-technique approach, often coupled to modeling, is fundamental to get a realistic picture of the studied system.

This problem is also evident while studying Cu-zeolites in the MTM reaction. Indeed, the reaction should be in principle ideal for characterization studies since it is not a real catalytic process but a multiple step one, including (1) pretreatment of the catalyst in O_2, (2) methane dosage, and (3) subsequent methanol extraction. However, the reaction yield is quite low, in that the methanol productivity normalized to Cu content is often below 0.1 mol_{CH3OH}/mol_{Cu} [26, 52], with the highest values reported up to now of 0.20 [53] and 0.35 mol_{CH3OH}/mol_{Cu} [54, 55] on Cu-ZSM-5 and Cu-MOR, respectively. This would imply that, assuming that one copper atom is needed to produce one methanol molecule, only a small fraction of Cu (varying from 10 to 30%, depending on the zeolite topology, pretreatment, and reaction conditions) is active in the title reaction. On the contrary, the 0.35 mol_{CH3OH}/mol_{Cu} productivity measured in MOR was interpreted by Grundner et al. as a proof of the presence of single-site trinuclear copper oxygen clusters [54, 55]. The lively debate about the different structures proposed as active Cu-oxo sites in the title reaction, following the first hypothesis of a bis(μ-oxo)dicopper core mentioned above, will be thus reviewed in the following section, trying to focus on weak and strong points of each hypothesis and of the corresponding characterization techniques.

2.2 Nature of Cu-Oxo Species in Medium and Large Pore Zeolites: Cu-ZSM-5 and Cu-MOR

As mentioned above, the first structure proposed as active site for the MTM reaction in Cu-zeolites is the bis(μ-oxo)dicopper core (structure **A** in Scheme 1). This structure however poses a problem about the charge of the involved Cu ions. Structure **A** can indeed be labeled as $ZCu^{III}(O_2)Cu^{III}Z$, where Z stands for a negative charge on the framework oxygen atoms (O_{fw}), generated by the presence of one Al^{III} heteroatom (A_{fw}). Since the formal charge of oxygen in the μ-oxo ligands is −2, a total −6 charge should be compensated by the two trivalent Cu ions, without any evidence for this unusual oxidation state in zeolites. This assignment was thus successively called into question by the same authors who firstly proposed it, thanks to the use of resonance Raman (rR), in collaboration with Solomon's group [45]. Namely, the rR spectra of an O_2-activated Cu-ZSM-5 were found to be well correlated with the intensity of the UV-Vis band at 22,700 cm^{-1} (Fig. 2a), which in turn was confirmed to be related to the active sites in the methanol formation on the basis of kinetic isotope effect (KIE) analysis as a function of reaction temperature.

The authors pointed out that EXAFS alone cannot provide structural information on the structure of the active Cu core, since this accounts for only a small fraction of the total Cu content (~5% in the studied Cu-ZSM-5, based on the methanol productivity). Being an average technique, EXAFS cannot distinguish the contribution of a minority of active sites from that of abundantly present spectator ones. The main rR bands at 456, 870, and 1,725 cm^{-1} could be safely assigned to a bent mono(μ-oxo) dicopper core (structure **B** in Scheme 1), based on the spectral changes observed when using a mixed isotope $^{16}O_2/^{18}O_2$, which clearly pointed to exclude the presence of μ-1,2-peroxo or hydroperoxo dicopper sites (Fig. 2b). Moreover, normal coordinate analysis (NCA) and density functional theory (DFT) calculations pointed to a Cu-O-Cu bending angle around 140°, which could only be compatible with a mono(μ-oxo) compound (Fig. 2c). Indeed, a Cu-O-Cu angle of 100° was found to be responsible for the Raman band around 600 cm^{-1} typical of bis(μ-oxo)dicopper cores, where the insertion of a second oxo ligand causes the tightening of the bending angles. A μ-(μ^2:μ^2)peroxodicopper core (structure **C** in Scheme 1) was also observed on a pre-reduced Cu-ZSM-5, after O_2 treatment at room temperature (RT). This is characterized by a broad UV-Vis absorption centered at 29,000 cm^{-1} and by rR bands at 736 and 269 cm^{-1}, and it was proposed as a precursor of the mono(μ-oxo)dicopper active sites [46]. For a more comprehensive review of the spectroscopic fingerprints and Cu··Cu distances of mono and dinuclear Cu/O_2 complexes, readers are referred to the following [37, 38, 56, 57].

The mono(μ-oxo)dicopper core (structure **B**) was also proposed as active site in Cu-MOR, which is characterized by larger pores with respect to ZSM-5 and by a higher density of actives sites [58, 59], resulting in the highest reported values of normalized methanol productivity (mol_{CH3OH}/mol_{Cu}) [54, 55]. Indeed, Cu-MOR is characterized by spectroscopic features very similar to Cu-ZSM-5: a UV-Vis band centered at 22,200 cm^{-1} and isotope sensitive rR bands at 450, 850, 1,700, and

1,850 cm^{-1} [60]. Based on the differences between spectra measured in O_2 at different temperatures, it was proposed that the UV-Vis feature in MOR is composed of two components, one centered at 21,900 cm^{-1}, unstable above 330°C, and a persistent one with maximum at 23,000 cm^{-1}. Moreover, kinetic measurements showed that the two copper sites responsible for these bands have different activation enthalpies for methane oxidation. The proposed bent mono(μ-oxo)dicopper core (structure **B**) was found to be very similar to those present in ZSM-5, regarding geometry (Cu-O-Cu bending angle) and electronic structures, so that the different kinetic behavior was explained invoking second-sphere effects related to the zeolite topology [60].

The $[Cu_2O]^{2+}$ core (**B**) in ZSM-5 is proposed to be located at the intersection of straight and sinusoidal ten-membered rings (10r) (Fig. 2c) [39, 45]. Namely, the Cu··Cu distance in the binuclear Cu^I precursor is 4.17 Å, which is reported to be in agreement with the location of Cu^I sites determined by crystal structure analysis [61]. In this structure, Cu ions have a twofold coordination to O_{fw}, with a $O_{fw(Si)}$-Cu-$O_{fw(Al)}$ bite angle ~149° and a Cu-O-Cu bend angle in the $[Cu_2O]^{2+}$ core of 135°. This structure was found to be more stable with respect to other possible structures in the MFI framework, indicating that it is stabilized by a particular framework structural entity.

A similar conformation of O_{fw} was searched for in the MOR framework, notwithstanding the differences in pore size (10r in ZSM-5 vs 12r in MOR) and pore connectivity (3D pore system consisting of straight 10r channels connected by sinusoidal ones vs straight 12r channels with 8r side pockets). Two possible structural motifs were identified at the intersection of the side pocket with the 12r and 8r channels, with adjacent Al framework atoms (Al-Si-Si-Al units with Al··Al distances around 7.55 Å, similarly to what was calculated for ZSM-5) located at the T3 or T4 tetrahedral sites. Thus, the proposed mono(μ-oxo)dicopper core (structure **B**) would be formed at specific framework structural motifs, identified in both ZSM-5 and MOR, with a very precise structural and electronic configuration. The observed differences in activity could be then ascribed to second-sphere effects, meaning that the zeolite lattice could play a role analogous to the active pocket of a metalloenzyme (directing methane approach to the active site, stabilizing transition states, etc.) [60]. The same $[Cu_2O]^{2+}$ core (**B**) in ZSM-5 was also shown to be formed upon N_2O decomposition [39].

2.3 *Studying the Modification of Cu Structure During Reaction: Operando X-Ray Absorption Spectroscopy in Cu-MOR*

The characterization studies reviewed in the previous paragraph mainly focused on the structure of the Cu-oxo complexes formed during the catalysts' pretreatments in O_2, and the correlation with the catalytic activity was mainly based on kinetic measurements concerning the evolution of the UV-Vis band around 22,000–23,000 cm^{-1} during reaction with methane [45]. A different and complementary approach to get further insights into the nature of the active sites was proposed by the group of van Bokhoven, mainly focusing on a high-loading Cu-MOR (Si/Al = 11, 4.3 Cu wt%, Cu/Al = 0.38) studied by XAS spectroscopy with the support of DFT calculations [59, 62–64]. A breakthrough communication from this group appeared in 2012, proposing methanol extraction from the surface of the catalyst by a wet stream of He [62]. This approach is alternative to the previous studies based on methanol extraction with solvents. With the goal to move from an intriguing academic playground to a process with potential industrial applications, the same group then showed the possibility to carry out reaction under isothermal conditions at 200°C [65] and very recently made a step forward by carrying out the reaction in anaerobic conditions, using water as selective oxidant [66].

Coming back to the characterization approach, the work by van Bokhoven and coworkers is mainly based on the use of XAS spectroscopy, measured in operando-like conditions, that is, while heating the sample in the presence of gas flows, monitoring the product gas with a mass spectrometer. With this setup, the authors followed the evolution of Cu oxidation state and local environment in Cu-MOR during O_2 treatment, CH_4 interaction, and steam-assisted methanol desorption. Based on the XANES spectra measured under steady-state conditions, the authors showed the reduction of a large fraction of the Cu^{II} sites formed during O_2 activation to Cu^{I}, as a consequence of CH_4 interaction at 200°C [62].

In a more detailed characterization work, the fraction of Cu^{II} reduced to Cu^{I} by CH_4 was quantified as >60%, by applying a linear combination fit (LCF) procedure to high-energy resolution fluorescence-detected (HERFD) XANES spectra [59]. The authors suggested that these could be the active sites, which modify their electronic structure during the reaction with methane, forming adsorbed product intermediates. The large discrepancy between the amount of reduced Cu^{II} sites in their Cu-MOR sample (>60%) and the fraction of active sites estimated in Cu-ZSM-5 on the basis of methanol productivity (~4%, calculated assuming two Cu sites per methanol produced [26]) was explained invoking a different cationic distribution in Cu-MOR, which is usually characterized by lower Si/Al ratios.

The reoxidation of a small fraction of Cu^{I} to Cu^{II} was also observed during extraction with water at 200°C, which was attributed to small contamination of O_2 in the wet He flow [59]. This was proposed to have important implications for a real catalytic process, since it would imply that the oxidation with O_2 at high temperature (400–500°C) is not mandatory for the catalyst reactivation in a continuous cycle, as subsequently shown in [66]. The fact that most of the XANES features remained unchanged after water interaction was explained with the difficulty (kinetic limitation) in desorbing the stable adsorbed intermediates. In the same publication, the authors also used conventional EXAFS to follow the different reaction steps in Cu-MOR [59]. As a general comment, the first shell coordination number (CN) of Cu activated in O_2 at higher temperature was between 4.5 and 5 and only slightly decreased after CH_4 interaction (3.9 ± 0.3). Even if the authors mentioned that the Cu^{II} state observed after O_2 activation is in agreement with the dicopper **B** core proposed by the groups of Schoonheydt and Solomon on the basis of rR spectra [45, 46], it is important to point out that the measured CN of 4.5 ± 0.4 does not fit with the local environment expected for Cu^{II} in the mono(μ-oxo)dicopper core. As mentioned above, in this structure, Cu has a threefold coordination, with two O_{fw} and one O_{ef} from the oxo ligand. Moreover, the authors clearly stated that second shell contributions were barely observable and could not be unambiguously fitted [59].

A further step to follow the electronic and geometric structural changes of Cu sites in Cu-MOR during the reaction steps consisted in the use of quick XAS (time resolution of about 5 s) [63]. In the related paper, the discussion was mainly based on the XANES features, focusing on desorption of the methane conversion intermediate as methanol in the wet stream. EXAFS data were only mentioned in relation to the small changes observed in the intensity of the first and second shell of Cu sites (at 1.4 and 2.6 Å), implying no changes in the first two coordination spheres during methanol desorption, but clear information about the Cu coordination number was not given. Some representative XANES spectra measured during some of the reaction steps are reported in Fig. 3a, with labels indicating the Cu^{II} and Cu^{I} XANES fingerprints.

In the used experimental conditions, XANES LCF assessed the presence of 41% Cu^{I} after methane interaction at 200°C, with the remaining copper present as “Cu^{II}-

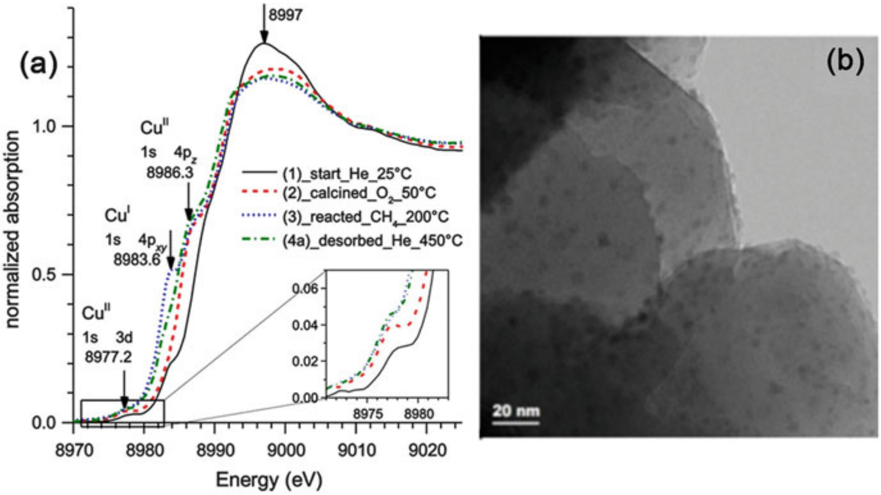

Fig. 3 (**a**) XANES spectra of Cu-MOR measured at different steps of the MTM reaction: (1) starting material at RT, (2) calcined in O_2, (3) reacted with methane, and (4) after product desorption in dry He. Arrows indicate the typical Cu^{II} and Cu^{I} XANES fingerprints with the corresponding involved core levels. Reprinted with permission from [63]. Copyright 2014 American Chemical Society. (**b**) TEM of high-loaded Cu-MOR (Si/Al = 11, Cu/Al = 0.38) after O_2 treatment at 450°C, showing the presence of small ($\leq$3 nm) copper oxide nanoparticles. Adapted from [64] with permission of the PCCP Owner Societies. Similar results were obtained on a Cu-MOR with similar Cu loading (4.7 wt% Cu, Si/Al = 6) after activation at 200°C [65]

O-like" sites and a significant fraction (20%) of hydrated Cu^{II}. The authors observed a noticeable desorption of methanol during the first 5 min of treatment with a He flow saturated with water, which was virtually finished after 20 min [63]. At this point, the amount of Cu^{I} was found to be almost halved, indicating a reoxidation of the sites involved in the intermediate formation and methanol formation. Interestingly, together with a major amount of hydrated Cu^{II} sites (62%), a fraction of "Cu^{II}-O-like" sites was still present. Moreover, analysis of the Cu^{I} and Cu^{II}-O evolution during methanol desorption under both wet (water saturated) and dry He flows suggested that some of the latter were formed by oxidation of the former. This aspect was stressed by the authors, since the mono(μ-oxo)dicopper cores proposed by the group of Schoonheydt are supposed to be water-unstable. It was thus proposed that "Cu^{II}-O-like" sites, whose structure could not be determined, are present in Cu-MOR together with the mono(μ-oxo)dicopper **B** ones and that they are also active for methanol formation [63].

Notwithstanding these evidences, the main XANES results were interpreted in terms of the mono(μ-oxo)dicopper **B** core, with the support of DFT calculations [63]. Namely, the reduction of half of Cu^{II} to Cu^{I} during methane flow was explained with the formation of a mixed-valent dicopper [Cu^{I}-OCH_3-Cu^{II}] stable methoxy intermediate, with the abstracted H atom stabilized as [Cu^{I}-OH-Cu^{II}] on vicinal Cu··Cu pairs. This would imply that, apart from a minor fraction of the "Cu^{II}-O-like" sites resistant to hydration, most of copper ions in the zeolite are involved in the reaction. This hypothesis cannot completely explain the generally low methanol productivity of Cu-zeolites (up to 0.20 and 0.35 mol_{CH3OH}/mol_{Cu} for MFI and MOR, respectively [53–55]). A different interpretation of operando XAS data during the reaction was very recently proposed by Pappas et al. on small-pore zeolite Cu-CHA, as will be discussed below [57].

A similar approach (in situ time-resolved XAS measurements coupled to DFT calculations) was successively used by the same authors to shed new light into the generation of the Cu-oxo active sites prior to methane activation [64]. The work was mainly inspired by the study from Smeets et al., who followed by diffuse reflectance (DR) UV-Vis and rR the formation of the mono(μ-oxo)dicopper **B** core, passing through the evolution of the μ-(μ^2:μ^2)peroxodicopper **C** precursor, by dosing O_2 on a pre-reduced Cu-ZSM-5 [46]. The possible mechanisms for Cu^{II} self-reduction during dehydration (disproportionation and condensation) were briefly discussed, starting from a $[CuOH]^+$ site, similarly to what was well established in Cu-CHA [50, 67]. The authors followed and compared Cu-MOR activation in He and O_2, with the aim to determine the minimum temperature for self-reduction and active site formation (estimated in 200°C). Moreover, LCF was again applied to XANES spectra to quantify the amount of Cu^{I} sites formed by self-reduction in He stream at this temperature, which are supposed to be able to activate O_2 forming the active Cu-oxo sites. The obtained amount (43%) was in good agreement with the fraction of copper sites (>40%) reduced upon methane interaction, supporting the hypothesis that these are the active site precursors [64].

Concerning EXAFS data, the authors included in the fitting model up to four shells in the coordination sphere of Cu when heated in O_2, including two shells of Cu atomic neighbors, which were taken as an indication of the presence of Cu··Cu dimers. The presence of an O_{ef} scattering path (at longer distance with respect to O_{fw}) was related to a bridging oxo ligand, even though the technique could not discriminate between the bis and mono(μ-oxo)dicopper cores (**A** and **B**) previously proposed in the literature. This aspect was thus dealt with by DFT calculations, which showed how the mono(μ-oxo)dicopper **B** core is favored in zeolites, at variance with homogeneous complexes where the most stable structure is the bis (μ-oxo) one [64].

The XAS features described above for a high Cu-loaded Cu-MOR, namely, a high average coordination number for the oxygen shell (ca 3.2) and small changes in the local geometric coordination sphere of Cu while heating or during the reaction, were successively found to be in agreement with the presence of significant fraction of copper oxide clusters and particles [65]. TEM analysis measured on Cu-MOR after activation at 200°C clearly showed the presence of finely dispersed nanoparticles, too small to be detected by XRD (≤3 nm, with a fraction smaller than 1 nm, Fig. 3b). The authors thus proposed that the observed copper oxide clusters/nanoparticles were active after activation in O_2 at 200°C, in the presence of high methane pressure (36–50 bar).

The DR UV-Vis spectra of Cu-MOR after activation at 200°C mainly consisted in a broad band centered around 13,000 cm^{-1}, which was assigned to Cu^{II} sites stabilized by one and two negative charges on the framework (i.e., in correspondence of one or two Al_{fw} atoms) [65]. Due to the absence of the fingerprint around 22,200 cm^{-1}, it was proposed that the mono(μ-oxo)dicopper cores, which are active at low methane pressure, are only formed after high temperature activation (450°C) [64]. On the contrary, the small copper oxide particles observed after activation at 200°C become active only in the presence of high reactant pressure. These results are in agreement with that previously reported by Beznis et al. on Cu-ZSM-5, who proposed that copper oxide clusters dispersed on the zeolite outer surface (observed by TEM) were not involved in the selective oxidation of methane at ambient pressure [36].

Other interesting and new characterization results were reported by Sushkevich et al., showing the possibility to carry out MTM conversion with water in anaerobic conditions [66]. The authors followed by XANES the redox changes undergone by copper during reaction with methane and successive interaction with water vapor, confirming the $Cu^{II}/Cu^{I}/Cu^{II}$ redox cycle during O_2 activation/CH_4 interaction/wet stream desorption. Importantly, thanks to in situ FTIR spectroscopy it was possible to follow the formation of molecular methanol and methoxy groups adsorbed on the catalyst surface during methane interaction. The growth of the bands related to reaction products was accompanied by a parallel increase of the typical OH stretching (νOH) of Si(OH)Al Brønsted sites. This indicates that the C-H cleavage corresponds to the formation of methoxy groups stabilized by copper sites and Brønsted sites formation, giving important information about the reaction mechanism. The authors also used CO and NO probe molecules to follow the changes of copper oxidation state during the reaction, to give further support to the changes observed by XANES [66]. For details about the typical spectral features and information which could be obtained with these techniques, readers are referred to the work by Giordanino et al. and references therein [37].

2.4 *Nuclearity of Cu-Oxo Active Sites: Size Matters?*

The characterization results described in the previous paragraphs were mainly based on the hypothesis of dinuclear Cu-oxo cores as active sites (Scheme 1), focusing on the electronic and geometric structure of the selective oxo ligand(s). This hypothesis was not called into question even when the authors observed different Cu sites, such as the copper oxide clusters reported by van Bokhoven and coworkers [65]. Indeed, the works from van Bokhoven's group are mainly based on XAS spectroscopy, which being an average technique cannot by itself discriminate between active and spectators sites, especially if the former are a minor fraction.

A different hypothesis about the structure of active Cu-oxo sites in large pore MOR and medium pore ZSM-5 zeolites was put forth in the group led by Lercher [54, 55, 68, 69]. In their very important contribution in Nature Communications, Grundner et al. based their discussion on the correlation between methanol yield and Cu concentration, in Cu-MOR with different Si/Al ratios [55]. This resulted in a linear correlation, with a slope around 0.33, which was taken as an indication that three atoms of Cu are needed to form one methanol molecule (Fig. 4b). Importantly, the reported methanol productivity is the highest so far reported in the literature (0.35 mol_{CH3OH}/mol_{Cu}, corresponding to 160 μmol/g), which was explained on the basis of the peculiar MOR topology motif and the controlled exchange procedure, minimizing copper hydrolysis and precipitation and the competition from alkaline cations. More in detail, the authors used infrared spectroscopy to quantify the amount of framework Al atoms (Al_{fw}) stabilizing Cu ions, by measuring the amount of Brønsted acid sites before and after Cu exchange on a sample with Si/Al = 11 and different Cu/Al ratios (Fig. 4a). Moreover, the use of different probes (pyridine and n-hexane) allowed the authors to conclude that Cu ions are preferentially exchanging

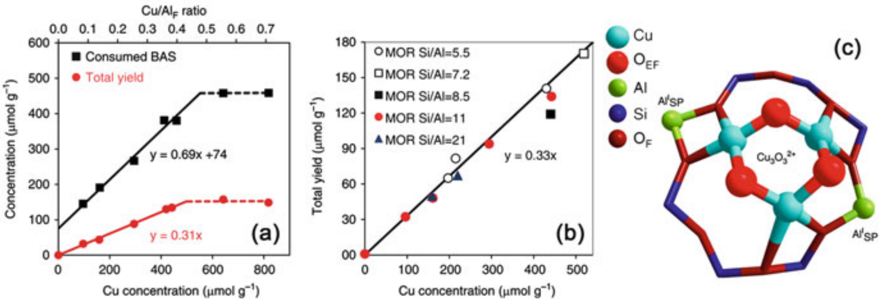

Fig. 4 (**a**) Estimation of the number of residual Brønsted acid sites measured by pyridine adsorption on a sample with Si/Al = 11 and different Cu/Al ratio (square symbols). The slope of 0.69 indicates that 2 H^+ are exchanged by three Cu ions; methanol yield on the same samples (circles). (**b**) Methanol yield as a function of Cu concentration on samples with different Si/Al ratios. The slope of 0.33 suggests that three Cu atoms are needed to obtain one methanol molecule. (**c**) DFT-optimized structure of the tris(μ-oxo)tricopper core (**D**) stabilized by two Al_{fw} at the 8r entrance of MOR side pocket (SP). The three active O_{ef} ligands point to the main 12r channel. From Grundner et al. [55], licensed under CC BY 4.0 (http://creativecommons.org/licenses/by/4.0/)

Brønsted sites located near the 8r pore mouth of the MOR side pockets. They also proposed that the exchange selectivity is related to the relatively high concentration of Al_{fw} in the side pockets (65% of the total, giving the Brønsted νOH band at 3,590 cm^{-1}). These considerations were supported by the observation that the νOH band related to the Brønsted sites in the main 12r channels (3,612 cm^{-1}) was not affected by Cu ion exchange. The quantitative data obtained from the abovementioned studies pointed to the conclusion that two Brønsted sites stabilize three Cu ions, which act as trinuclear single sites in the MTM reaction (core **D** in Scheme 2). This hypothesis was further supported by the observation that a majority of Al_{fw} atoms in samples with Si/Al 11 and 21 are separated by only one or two Si framework atoms.

These interesting findings were rationalized in terms of tris(μ-oxo)tricopper $[Cu_3(\mu\text{-}O)_3]^{2+}$ complexes, on the basis of DFT calculations (structure **D**, Fig. 4c). The structure obtained by DFT, characterized by a low symmetry (i.e., the Cu atoms in the clusters are not equivalent), was found to fit well with the EXAFS data measured on an O_2-activated Cu-MOR. More in detail, different Cu-O distances were fitted in the first shell, in agreement with the presence of O_{fw} and O_{ef} ligands. This was fitted assuming both Cu-Cu and Cu-O scattering path in a low symmetry core, that is, with a nuclearity higher than 2. Importantly, the authors acknowledged the intrinsic limitation of XAS spectroscopy, which gives an average information on all present Cu sites. However, the clear correlation between Cu loading and productivity allowed them to conclude that the analyzed data were related to a trinuclear single site [55].

Interestingly, the authors observed in in situ XAS studies that a second shell in the coordination sphere of Cu is starting to develop at 200°C, indicating that the Cu^{II} ions are moving to form stable oxo clusters in O_2 from this temperature [55]. In the same conditions, the band at 22,700 cm^{-1} assigned to the mono(μ-oxo)dicopper core (structure **B**) was not observed, in agreement with that found by Tomkins et al. [65]. Instead, a broad component was found at 31,000 cm^{-1}, slowly decreasing upon methane interaction. No significant changes were observed in the EXAFS spectra during the same treatment, suggesting that the local structure of copper is not affected by the formation of oxidized adsorbed intermediates.

In another interesting contribution from the same research group, EXAFS was used to assess the presence of tris(μ-oxo)tricopper complexes also in Cu-ZSM-5. In

Scheme 2 The tris(μ-oxo) tricopper core (**D**) proposed by Lercher and coworkers in Cu-MOR [55]

this sample, the trinuclear cores were proposed to coexist with mono and dinuclear clusters, or with copper oxide nanoparticles, depending on Cu loading. Moreover, 50% of the $[Cu_3(\mu\text{-}O)_3]^{2+}$ cores were found to be inactive, suggesting that the reactivity is not only related to the cluster structure, but it is strongly influenced by the ability of the zeolite framework to stabilize them [69].

The intriguing debate about the nuclearity of active copper sites was then addressed by modeling, considering Cu location, structure, and reactivity on different zeolite topology such as MFI [68], MOR [70], and on a series of zeolites with different pore sizes and shapes (MOR, MFI, CHA, AFI, and TON) [71]. A detailed computational study about the structure and reactivity of the mono(μ-oxo)dicopper and tris(μ-oxo)tricopper complexes (structures **B** and **D**, respectively) in Cu-ZSM-5 was carried out by Li et al. [68]. The γ-site, with two Al sites at T7 and T2 lattice positions of the sinusoidal channel of MFI framework, was proposed as representative location for the di- and trinuclear oxo complexes. These were supposed to be formed via self-organization of extraframework mononuclear Cu sites during high temperature activation in O_2. Based on thermodynamic analysis, $[Cu_3(\mu\text{-}O)_3]^{2+}$ structures were found to be more stable at high O_2 pressure, while relatively low chemical potential of O_2 would favor the formation of $[Cu(\mu\text{-}O)Cu]^{2+}$ clusters.

Interestingly, computed Bader atomic charges showed for both complexes a formal charge different from that expected from stoichiometry (two Cu^{II} in the **B** binuclear core, two Cu^{III} and one Cu^{II} in the **D** trimer). Indeed a Bader charge around $-0.7/-0.77$ *e* was calculated for the oxo ligands (di- and trinuclear, respectively), which is lower in comparison to the value of -1.09 *e* for CuO. This points to a radical character of the bridging O_{ef}, necessary to promote homolytic C-H activation and cleavage. This would result in Cu^{II}/Cu^{I} formal charge in the dimer and of a mixture of Cu^{II}/Cu^{I} in the trinuclear. Both structures were however found to be stabilized by charge delocalization, making the Cu sites indistinguishable. Finally, the activation barrier for C-H cleavage was found to be sensibly lower (and close to the experimental value of 64–68 kJ/mol) for the tris(μ-oxo)tricopper **D** complexes with respect to the mono(μ-oxo)dicopper **B** ones. The formation of methanol was proposed to involve the direct radical rebound mechanism for the former and the formation of strongly adsorbed methoxy groups on the latter [68].

In answer to this interesting report, a DFT-based geometry optimization was successively reported by Palagin et al. for Cu-MOR [70]. The authors observed a general trend in the relative stability of copper oxide clusters, with tetra- and pentamers in the 8r channel of MOR being more stable than dimers. This would suggest that, by carefully tuning Al_{fw} content and distribution, one could design catalysts embedding large clusters, stabilized by multiple Cu-O linkages, and allowing for the stabilization of the OH and CH_3 fragments during methane activation, resulting in higher activity.

2.5 Cu-Oxo Moieties in Small-Pore Zeolites: Cu-CHA

Further insights about the properties of Cu-oxo complexes stabilized in zeolites came from the report by Lobo's group about the catalytic activity in the MTM reaction of small-pore zeolites and zeotypes, namely, Cu-SSZ-13 and Cu-SAPO-34 (CHA), Cu-SSZ-16 (AFX), and Cu-SSZ-39 (AEI), all characterized by 8r pore opening [72]. More in detail, the authors measured a relatively high methanol productivity on the three small-pore zeolites, ranging from 28 to 39 μmol of methanol per gram of zeolite, corresponding to 0.03–0.09 mol_{CH3OH}/mol_{Cu}. These values are considerably lower in comparison with the results by Lercher and coworkers on high-loaded Cu-MOR (Si/Al = 11 and 21, Cu/Al = 0.4 and 0.6) [55]. However, they were among the highest conversions reported at the time of publication and point to the fact that the reaction can be obtained also on small-pore zeolites, such as Cu-SSZ-13, where the presence of monomeric extraframework Cu sites had been well established by parallel studies focused on NO_x SCR [37, 50, 67, 73–78].

The DR UV-Vis spectra measured by Wulfers et al. on the tested samples after activation in O_2 are reported in Fig. 5 [72]. It is evident that the feature assigned to the mono(μ-oxo)dicopper cores at 22,700 cm^{-1} is only present in Cu-ZSM-5, which

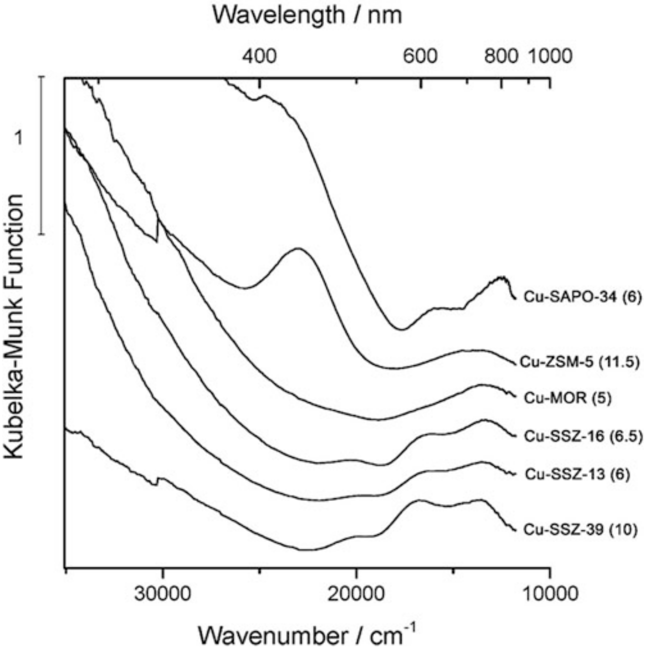

Fig. 5 DR UV-Vis spectra measured at RT on different Cu-exchanged zeolites and zeotypes after activation in O_2 at 450°C. Numbers in brackets refer to the Si/Al ratio (Al + P/Si ratio for SAPO-34). Reproduced from [72] with permission of the Royal Society of Chemistry

showed a lower or comparable productivity with respect to the small-pore zeolites tested in similar conditions (16 μmol/g, corresponding to 0.03 mol_{CH3OH}/mol_{Cu}). Moreover, the DR UV-Vis spectra of the three 8r pore zeolites are characterized by a very similar shape of the low-frequency bands, assigned to ligand field *d-d* transitions, with bands centered around 11,000, 13,600, 16,500, and 19,700 cm^{-1} (the so-called quadruplet) [37]. This would point to a similar geometry of monomeric Cu sites stabilized by the negatively charged framework. The structure of these sites will be discussed in more detail in the following section. However, it is important to underline the fact that this milestone work by Lobo's group extended the discussion about the nuclearity of Cu-oxo active sites in MTM to the lower limit, i.e., to monomeric Cu counterions. Interestingly, Cu-SSZ-13 was also shown to be active in MTM while using N_2O as oxidizing agent (methanol productivity up to 35 μmol/g) [79].

The structure of the Cu-oxo species possibly forming in Cu-SSZ-13 was analyzed by Vilella et al. by DFT calculations [71]. The authors calculated the relative Gibbs energies, geometry (Cu-Cu and O-O bond lengths), spin densities (expressed as Cu/O magnetization), and vibrational frequencies of different monomeric and dimeric Cu-oxo complexes, proposed in the literature as active sites in Cu-zeolites and experimentally characterized. The side-on $[Cu(\eta^2\text{-}O_2)]^+$ monomeric core was found to be more stable than the end-on $[Cu(\eta^1\text{-}O_2)]^+$ one (**F** and **E**, respectively, in Scheme 3). The structure of the mono(μ-oxo)dicopper cores (**B**) was also calculated, and the relative stability of $Cu_2\text{-}O_2$ complexes (which have been characterized in homogeneous complexes or enzymes but discarded as active sites in zeolites by the previously reviewed studies) compared. Moreover, the effect of the zeolite topology on the stability (and presumed reactivity) of the complexes was studied. The side-on $[Cu(\eta^2\text{-}O_2)]^+$ core (**F**) was found to be strongly bonded in correspondence of one

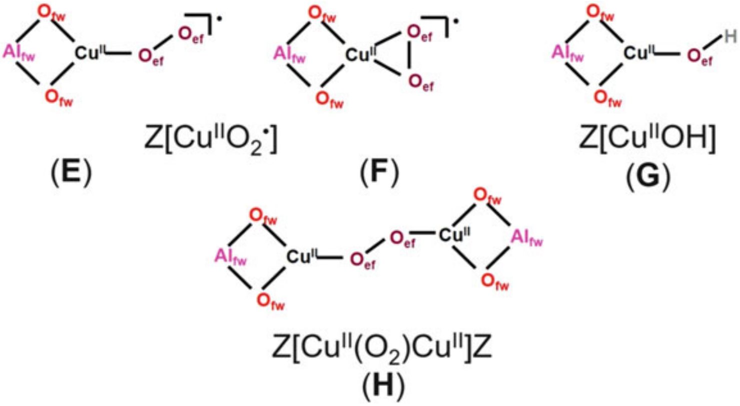

Scheme 3 Mononuclear and dinuclear Cu-oxo structures discussed in relation to small-pore zeolites, particularly CHA: **E**, side-on $[Cu(\eta^2\text{-}O_2)]^+$; **F**, end-on $[Cu(\eta^1\text{-}O_2)]^+$; **G**, $[Cu(OH)]^+$; **H**, *trans*-(μ-1,2-peroxo)dicopper cores [56, 57, 71]. Al_{fw} and O_{fw} represent Al and O framework atoms, respectively, generating a negative charge which stabilizes the Cu^{II} counterions. O_{ef} indicates extraframework oxygen atoms, resulting from the interaction with O_2

Al_{fw} atom in all the considered structures, with a higher adsorption Gibbs energy (−1.56 eV) in the 8r of CHA. On the contrary, the adsorption energy of O_2 was similar (−1.3 eV) in most of the studied structures (apart from MOR, with a value of −1.03 eV), suggesting that the framework is not affecting the introduction of the O_2 ligand on the Cu sites. Moreover, the adsorption energy of O_{ef} in the mono (μ-oxo)dicopper cores **B** was found to be lower in CHA and MOR with respect to the other considered frameworks. In small-pore CHA, the higher stability of the dinuclear core was calculated when the two Al_{fw} atoms necessary for charge compensation were spaced by three Si_{fw} atoms [71]. Further DFT calculations from the same group proposed the $[Cu(OH)]^+$ site (species **G**) as responsible for the MTM activity in Cu-CHA zeolites [80].

The stability of different Cu-oxo structures in CHA was also addressed with DFT calculations by Ipek et al., who carried out a detailed characterization work based on XRD, DR UV-Vis, and Raman spectroscopies on Cu-SSZ-13 samples with Si/Al = 12 and Si/Al = 5 [56]. The authors reported the higher stability of the $[Cu(OH)]^+$ **G** site in CHA, with respect to the mono(μ-oxo)dicopper core **B** and two slightly different *trans*-(μ-1,2-peroxo)dicopper complexes (**H** in Scheme 3), which were however proposed to be also likely present on Cu-CHA after activation in O_2 at 450°C.

The Raman feature at 617 cm^{-1} was assigned to structure **B**, while bands at 476, 510, and 580 cm^{-1} were related to complexes **H** (Fig. 6a). Moreover, the authors assigned the UV-Vis features observed on the different O_2-activated Cu-SSZ-13 catalysts at 34,700, 30,000, 19,700, 16,500, and 13,600 cm^{-1}. Based

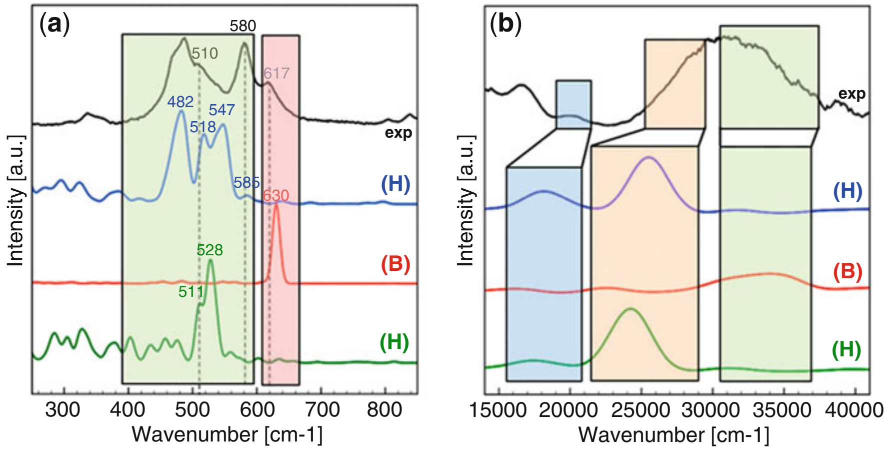

Fig. 6 Comparison of experimental and calculated Raman (**a**) and UV-Vis spectra (**b**) measured on O_2-activated Cu-SSZ-13 samples. Calculations were based on the optimized structures of the mono (μ-oxo)dicopper core **B** and two slightly different *trans*-(μ-1,2-peroxo)dicopper complexes (**H**). The experimental Raman spectrum was measured on a Cu-SSZ-13 sample with Si/Al = 12 and Cu/Al = 0.4; the plotted experimental UV-Vis is the difference spectrum between a sample with Si/Al = 12 and Cu/Al = 0.4 and one with same Al content and Cu/Al = 0.18. Adapted with permission from [56]. Copyright 2017 American Chemical Society

on the difference spectrum between two samples with the same Si/Al ratio and different Cu content, the broad absorption between 22,200 and 37,000 cm^{-1} (Fig. 6b) was assigned to the contribution of the two *trans*-(μ-1,2-peroxo)dicopper complexes **H**, which were proposed to be involved in methane activation based on their disappearance upon methane contact, and to the mono(μ-oxo)dicopper core **B**. The $[Cu(OH)]^+$ site was instead related to the *d-d* band at 13,600 cm^{-1}, not consumed during the interaction with methane [56].

Structure-activity relationships on Cu-CHA were recently addressed by Pappas et al., who combined XAS spectroscopy with a systematic work about the effect of the different experimental parameters (O_2 and methane activation temperature, partial pressure and activation/contact time, water-assisted extraction temperature) to a set of Cu-SSZ-13 catalysts with different Si/Al and Cu/Al ratios (from 5 to 29 and from 0.14 to 0.5, respectively) [57]. Infrared and rR spectroscopies were also used as complementary techniques. By optimizing the experimental conditions, the highest methanol productivity measured on Cu-SSZ-13 catalysts was obtained: 0.2 mol_{CH3OH}/mol_{Cu}, corresponding to 125 μmol/g. Similarly to what was previously done by Ayalon et al. on Cu-MOR [63], the authors followed by XANES and EXAFS the changes in the oxidation and coordination sphere of copper during O_2 activation, He flush, subsequent methane dosage, and water-mediated extraction. XANES LCF allowed estimating the relative fractions of framework-interacting Cu^{II}, hydrated Cu^{II}, and Cu^{I} sites during the different steps to be quantified, evidencing a linear correlation between the catalysts' reducibility and their methanol productivity [57].

However, at variance with the results reported for Cu-MOR, the EXAFS data obtained on Cu-SSZ-13 could be mainly explained in terms of monomeric extraframework Cu sites (Fig. 1a). More in detail, previous characterization studies clearly showed that activation in O_2 at 400°C causes the formation of a monomeric $Z[Cu(OH)]^+$ **G** sites (Fig. 7a and Scheme 3), with a lower fraction of $ZCu^{II}Z$ sites (where Z stands for a negative charge on the framework oxygen atoms generated by the presence of one Al_{fw}) [67], whose relative concentration depends on the Si/Al and Cu/Al ratios [50, 76]. Monomeric ZCu^{I} sites located at both 6r and 8r units were instead formed by self-reduction of $[Cu(OH)]^+$ sites during activation in inert flow (Fig. 1a, left) [50, 67, 74, 76]. These findings were corroborated by using DFT-optimized structures as input for the fit of the EXAFS data. Namely, the second shell of Cu could be satisfactorily described with one Al_{fw} atom, with distances around 2.7–2.8 Å, ruling out a major contribution from Cu-Cu scattering paths in the second shell region (Fig. 7a–c).

Starting from these evidences, in the work related to the activity of Cu-SSZ-13 in MTM, Pappas et al. focused their attention on the formation of Cu-oxo sites as a function of the activation conditions, also decoupling Cu^{II} dehydration/self-reduction and subsequent O_2 interaction [57]. Very similar XAS features and methanol productivity were observed on the catalyst (Si/Al = 12, Cu/Al = 0.5) directly activated in O_2 at 500°C and contacted with O_2 at the same temperature after activation in He flow (Fig. 7d, e). These consisted in the typical pre-edge features of Cu^{II} (red and burgundy XANES spectra, Fig. 7d), with a residual amount of Cu^{I}

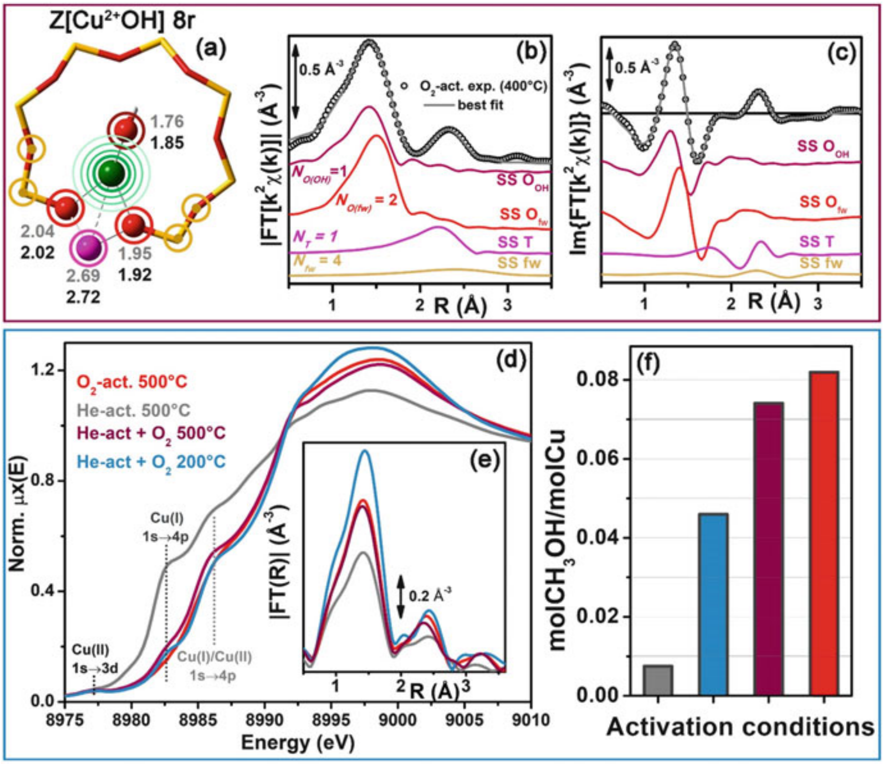

Fig. 7 (**a**) DFT-optimized structure of the most stable Z[Cu(OH)]$^+$ **G** sites in Cu-CHA (Cu, green; O, red; Al, pink; Si, yellow); colored circles highlight the different shells of neighboring atoms, with DFT-optimized distances, (**b**) and (**c**) report the experimental FT-EXAFS spectra (modulus and imaginary parts, black circles) of an O_2-activated Cu-SSZ-13 catalyst (Si/Al = 12, Cu/Al = 0.44), with the best fit (gray curve) corresponding to the DFT model. Single scattering paths for each coordination shells are reported, with the same color code as in part (**a**) [67]. (**d**) XANES and (**e**) FT-EXAFS spectra of a Cu-SSZ-13 with similar composition, after activation in He at 500°C, in O_2 at 500°C, and decoupled dehydration/oxidation steps: activation in He followed by O_2 dosage at 200 and 500°C; (**f**) corresponding methanol productivity [57]

around 10%. A similar Cu^{II}/Cu^{I} ratio was observed on the sample oxidized at 200°C after He treatment, but in this case, the spectrum was characterized by a higher white line intensity (blue curve).

Accordingly, fits of the EXAFS spectra after activation at 500°C resulted in Cu^{II} sites with CN $\cong$ 3, while reoxidation at 200°C caused an increase to ~4, indicating a different coordination of oxo ligands to the Cu^{II} sites, testified by the higher intensity of the first shell FT-peak (Fig. 7e). While the second shell peak could be assigned to Al_{fw} atoms, as discussed above, the high quality of the spectra allowed the authors to assess the presence of a third FT-EXAFS peak, which was best-fitted including Cu-Cu scattering paths at around 3.4 Å. This suggested the presence of a fraction (estimated around 30%) of Cu_xO_y moieties [57].

The different coordination of oxygen on the monomeric Cu^{II} sites was explained in terms of end-on $[Cu(\eta^1\text{-}O_2)]^+$ **E** and side-on $[Cu(\eta^2\text{-}O_2)]^+$ **F** structures, whose presence was confirmed by rR spectroscopy ($\nu_{O\text{-}O}$ broad bands with maxima at 1,100 and 1,155 cm^{-1}). More in detail, the authors proposed that the former (**E**) is formed by insertion of O_2 on pre-reduced Cu^I sites or by internal pathways involving the $[Cu(OH)]^+$ **G** sites, while the latter is only stable at lower temperature and is thus formed by reaction of Cu^I with O_2 at 200°C or by cooling down the sample in O_2 atmosphere. Due to the higher activity measured on the catalysts activated at 500°C, the tridentate end-on **E** complex was proposed as the most favorable site geometry for methane conversion.

As far as the Cu_xO_y moieties are concerned (accounting for 30% of copper and characterized by Cu-Cu distances around 3.4 Å), different mono(μ-oxo)dicopper (**B**), *trans*-(μ-1,2-peroxo)dicopper (**H**), and μ-(μ^2:μ^2)peroxodicopper (**C**) complexes were considered in the reaction mechanism. In agreement with Ipek et al. [79], rR measurements confirmed the presence of the first two, with bands at 830 cm^{-1} ($\nu_{O\text{-}O}$), 507 and 580 cm^{-1} ($\nu_{Cu\text{-}O}$) for the *trans*-(μ-1,2-peroxo)dicopper core, and the $\nu_{Cu\text{-}O}$ at 618 cm^{-1} for the mono(μ-oxo)dicopper ones. Structure **C**, not experimentally observed by the authors, was proposed to evolve into the more stable mono (μ-oxo)dicopper (**B**), by release of one O_{ef} atom [57].

3 Fe-Zeolites for Selective Oxidations of Methane and Benzene

3.1 N_2O as Oxidizing Agent

The catalytic activity of Fe-containing zeolites in the MTM reaction was firstly reported by the group of Panov at the beginning of the 1990s [28, 29, 31]. Methanol was extracted (with water or water solution of acetonitrile) from the surface of a Fe-exchanged H-ZSM-5. Similarly to what was carried out on Cu-zeolites in more recent years, the product was formed by interaction of methane (at RT) with a sample previously oxidized. The reactivity of Fe-zeolites (mainly MFI, but also BEA and FER [81–88]) was related to the formation of the so-called α-oxygen, an active and selective oxo species adsorbed on Fe sites upon N_2O interaction at relatively low temperature (200–250°C). N_2O was selected as oxidizing agent in relation to the observed activity and selectivity and for the potential application in the cleanup of tail gases of nitric acid plants [89, 90].

Due to the issues related to the methanol extraction from the catalyst surface, the research interest moved to the benzene to phenol reaction, an important process traditionally carried out by within a three-stage cumene technology. However, the active sites responsible for the selective hydroxylation reactions, through formation of α-oxygen, were supposed to be the same for both methane and benzene [91]. The focus of the abundant literature on the subject was mainly on the nature of α-oxygen, formed upon N_2O interaction/decomposition, and on the electronic and geometric structure of the so-called Fe-based α-sites.

As pointed out in the short review by Zecchina et al., the determination of α-sites structure needs to be guided by well-established facts about the catalytic activity in N_2O decomposition [10]. Namely, (1) Fe-ZSM-5 (containing Al_{fw} and the related Brønsted sites) are always more active than Al-free Fe-silicalite with the same iron loading; (2) active sites are formed during the treatment under inert (particularly at high temperature), resulting in the formation of Fe^{II} α-sites (implying a self-reduction of Fe^{III}, as occurred for copper); (3) when contacted with N_2O at low temperature, Fe^{II} α-sites form α-oxygen species on Fe^{III} sites; (4) α-oxygen able to give selective hydroxylation reactions is not formed when using O_2; and (5) activity normalized to Fe content increases with dilution, pointing to exclude the catalytic activity of clustered/aggregated Fe_xO_y/Fe_2O_3 species: instead, it is believed that they catalyze nonselective over-oxidation reactions.

Even if the reversible redox Fe^{II}/Fe^{III} cycle and related activity in selective oxidation reactions show many resemblance with the Cu^{I}/Cu^{II} one, the chemistry of iron is much more complex. Indeed, Fe^{II} ions are easily oxidized to Fe^{III} in aqueous solution. The latter cannot be easily stabilized as counterion, since three negative charges on the zeolite framework would be required. Moreover, it shows a high tendency to agglomerate in aqueous medium, forming hydroxide suspensions easily evolving into iron oxide/hydroxide clusters or aggregates, dispersed within the zeolite porosity or deposited on the particle external surface (Fig. 1b). Thus, many different exchange procedures were proposed to obtain highly dispersed species, such as sublimation/chemical vapor deposition (CVD) of volatile precursors such as $FeCl_3$ [92–94], aqueous exchange of ferrous salts in inert atmosphere to avoid oxidation from Fe^{II} to Fe^{III} [88, 95], and use of oxalate or similar salts to contrast agglomeration, thanks to the chelating ligand [96, 97].

Then, careful thermal treatments of low-loaded Fe-zeolites (less than 0.6 wt%) initially containing only framework Fe^{III} atoms introduced during the synthesis (Fe_{fw}, Fig. 1b) were found to be one of the most effective ways to obtain highly dispersed and selective α-sites [87]. When iron is inserted as Fe_{fw}, Fe(OH)Si Brønsted sites are generated, with lower acid strength and thermal stability with respect to Al(OH)Si ones [98]. These sites do not show catalytic activity in partial oxidation reactions, being coordinatively saturated [91], but they are transformed into extraframework species (Fe_{ef}) during calcination and successive thermal treatments [10, 91, 98, 99].

A particularly lively debate focused on the nuclearity of α-sites, similarly to that discussed above for Cu-zeolites [10, 87, 88, 100]. Indeed, since the first reports about the possibility to carry out the selective hydroxylation of hydrocarbons with Fe-zeolites, the similarity with the reactivity of monooxygenase (MO) enzymes was pointed out [91]. Methane monooxygenase (MMO), containing two iron atoms, is able to generate oxygen species of outstanding reactivity, capable to selectively form methanol by RT oxidation of methane. Thus, different research groups proposed evidences of the presence of dinuclear Fe moieties stabilized by the zeolite frameworks, mimicking the structure and oxygen activation ability of metal cores in MMO

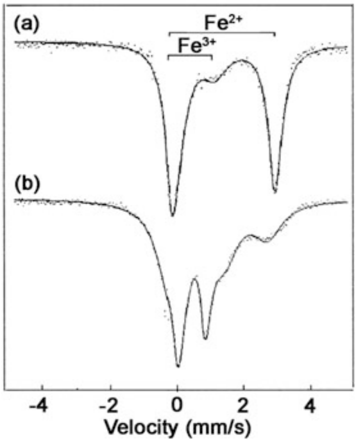

Fig. 8 Mössbauer spectra of ^{57}Fe-ZSM-5 before (**a**) and after (**b**) α-oxygen loading. Reprinted from, Catalysis Today, 41, G. I. Panov et al., Generation of active oxygen species on solid surfaces. Opportunity for novel oxidation technologies over zeolites, 365–385, Copyright 1998, with permission from Elsevier [91]

[91, 101–105]. For instance, Panov reported Mössbauer spectra of ^{57}Fe-ZSM-5 samples before and after loading with α-oxygen (Fig. 8) [91]. Transformation from a broad doublet assigned to Fe^{II} to a narrow one typical of Fe^{III} was observed upon N_2O interaction. Spectra of the supposedly formed α-oxygen complexes could be interpreted either involving two states of Fe^{III} or assuming the nonequivalence of the ligand environment of two Fe^{III} ions of the same complex. Moreover, the good agreement between the spectral parameters of both reduced and oxidized states of iron in ^{57}Fe-ZSM-5 and those of diiron MMO complexes was pointed out [91].

Concerning the α-oxygen properties, the main experimental studies involved KIE measurements and microkinetic analysis with the temporal analysis of products (TAP) approach [91, 106–109]. On the contrary, different spectroscopic techniques were used by different research groups around the world to get insights about the geometric and electronic structure of the Fe α-sites, able to decompose N_2O at low temperature to form the adsorbed and active α-oxygen. The extremely abundant literature which appeared in almost three decades on the subject cannot be reviewed in this contribution. The very recent publication in Nature Communication by Schoonheydt and Solomon groups testifies alone for the still intriguing and controversial scientific debate on the nature of α-sites [88]. Thus, only some examples concerning the most representative techniques used for the characterization of iron sites active in selective hydroxylation reactions with N_2O are here discussed, without trying to give a definite answer to the mono/dinuclear debate about α-sites structure. Generally speaking, the main characterization techniques are the same discussed in relation to Cu-zeolites: DR UV-Vis [81, 82, 84, 86, 100, 110–113], XAS [9, 86, 92, 94, 100, 113–115], infrared [9, 82, 84, 86, 87, 94, 110, 113, 116–123], and Raman [124–127], together with EPR [104, 110, 111, 117], Mössbauer [91, 94, 103–105, 128], voltammetry [82, 128], magnetic circular dichroism (MCD) [88], and resonant inelastic X-ray scattering (RIXS) [129] spectroscopies, often supported by DFT modeling [84, 88, 130–134].

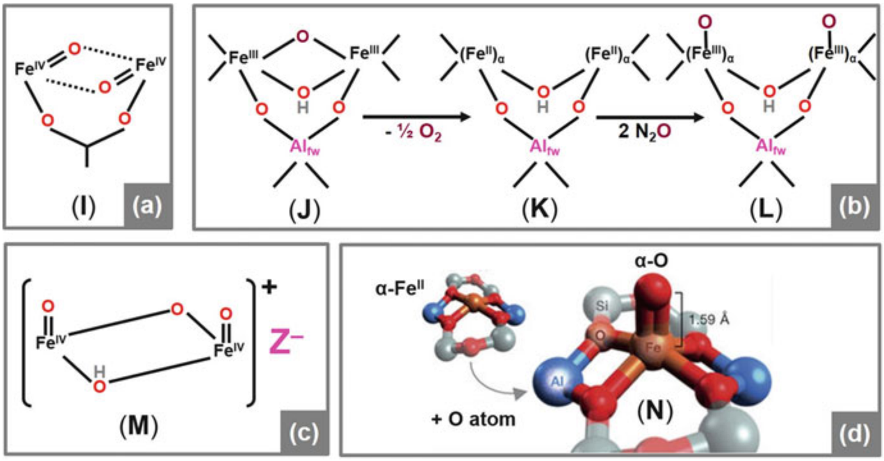

Scheme 4 (**a**) Fe^{IV} Fe$_2$(μ-O)$_2$ core proposed as intermediate Q in MMO (**I**) [102]. (**b**) Ferric mono(μ-oxo)mono(μ-hydroxo)diiron (**J**) evolving into ferrous mono(μ-hydroxo)diiron (**K**) by self-reduction and into complex (**L**) by successive N$_2$O adsorption [92, 105]. (**c**) Dinuclear "ferryl-like" [Fe$_2$O$_2$H$^+$] cluster (**M**) proposed by Kiwi-Minker et al. [135]; (**d**) DTF-optimized structure of a mononuclear "ferryl-like" α-Fe^{IV}=O site in the BEA 6r window (**N**). Adapted by permission from Macmillan Publishers Ltd.: Nature [88], Copyright 2016

Clearly, the proposed structures of α-oxygen were related to the assumed nuclearity of the involved α-sites. It is not possible to fully review in this contribution the lively debate on the subject. We only mention some of the dinuclear oxo α-sites inspired by what was observed in MMO enzymes [101, 102] and proposed on the basis of experimental results such as XAS and Mössbauer spectroscopy. Scheme 4 reports the high-valent (Fe^{IV}) Fe$_2$(μ-O)$_2$ diamond core proposed as key intermediate Q in MMO [102] (core **I**). On the basis of Mössbauer measurements, a ferric mono(μ-oxo)mono(μ-hydroxo)diiron complex (core **J**, similar to that proposed by Marturano et al. on the basis of XAS [92]) was suggested to evolve into a reduced form during activation (core **K**) and then into core (**L**) after N$_2$O interaction (Scheme 4) [105]. Indeed, quantitative evaluations about the amount of α-oxygen pointed to the fact that each Fe atom in the complex was capable of generating one α-oxygen (structure **L**). This would mean that α-sites are monatomic entities in a paired arrangement registered by Mössbauer spectroscopy as dinuclear complexes [105].

The presence of coupled "ferryl-like" Fe^{IV}=O structures was instead proposed by Kiwi-Minsker et al. (core **M** in Scheme 4) [135], and successively questioned by Pirngruber et al. on the basis of RIXS measurements, favoring the presence of Fe^{III}-O$^-$ radicals [129]. On the contrary, Zecchina et al. proposed a "ferryl-like" structure, formed upon N$_2$O reaction on monomeric grafted Fe^{II} sites [10]. A similar monomeric α-site was very recently proposed by Snyder et al., assuming a Fe^{II}

ion stabilized by two negative charges in a 6r window of BEA (structure **N** in Scheme 4; see later for a more detailed discussion) [88].

At the basis of the lively debate about the structure of α-sites, apart from the interesting activity that could possibly mimic that of MMO enzymes, a key issue is that Fe-zeolites are very far from what is generally considered as a "single-site" catalysts. In fact, as resumed in the pictorial representation by Zecchina et al. (Fig. 1b), a variety of Fe_{ef} species are generated by ion exchange or during the thermal treatments causing the breaking of framework bonds and the migration of Fe_{fw}, including grafted/anchored Fe^{II} sites, small $Fe_xO_y(OH)_z$ clusters, and larger Fe_2O_3 particles [10]. This means that averaged techniques, such as XAS, are likely to give a misleading description of the active sites, since the studied material is often characterized by a heterogeneous distribution of Fe species, including isolated/dispersed sites and clusters/agglomerates of different size. Indeed, Zecchina et al. analyzed a large number of literature XAS data on Fe-zeolites, showing a large scattering of the reported Fe-O, Fe-Fe, and Fe-Al distances, indicating a high heterogeneity of Fe speciation [10], as successively confirmed by rR measurements [125].

The problem of Fe species heterogeneity is also encountered using DR UV-Vis spectroscopy. Indeed, UV-Vis spectra of Fe-zeolites are often characterized by complex and broad absorptions, depending on the preparation method, iron content, and activation conditions. This was rationalized by Kumar et al., who carried out spectra deconvolution to assign distinct sub-bands to the variety of isolated/clustered/aggregated iron sites formed in zeolites. Namely, bands between 200 and 250 nm (50,000–40,000 cm^{-1}) were assigned to isolated Fe^{III} sites (Fe_{fw}) and absorptions between 250 and 350 nm (40,000–29,000 cm^{-1}) to small oligonuclear and larger (350–450 nm, i.e., 29,000–22,000 cm^{-1}) Fe_xO_y moieties inside the micropores, while bands above 450 nm (<22,000 cm^{-1}) can be related to extended Fe_2O_3-like agglomerates on the external particles' surface (Fig. 9a) [111, 136]. However, as pointed out in [10], the information that can be extracted from UV-Vis spectra of active Fe-zeolites is intrinsically limited. Indeed, the ligand field *d-d* transitions of Fe^{III} ions (d5 configuration) are very weak, being both Laporte and spin forbidden (inset of Fig. 9b; see also [98] for a more detailed discussion about the expected transitions for Fe^{III} ions and related issues). The corresponding ligand to metal charge transfer (LMCT) bands for isolated Fe^{III} ions (such as those observed in as-prepared Fe-zeolites with Fe_{fw} as unique species, Fig. 9b) are centered at 46,500 and 41,500 cm^{-1}, overlapping to the spectroscopic fingerprints of clustered/agglomerated sites (compare parts a and b of Fig. 9).

On the basis of the smaller ligand field and lower oxidation state of Fe^{II} with respect to Fe^{III}, the corresponding *d-d* transitions are expected at lower frequency (NIR region), and LMCT at higher ones, making them difficult to be detected [10]. Indeed, a clear evidence for Fe^{II} α-sites was only recently reported by Snyder et al., who measured DR UV-Vis spectra on a Fe-BEA zeolite with low Fe content (0.3 wt%, Si/Al = 12) [88]. The sample (activated in He at 900°C and subsequently reduced with H_2 at 700°C) showed three weak ligand-field bands at 15,900, 9,000, and <5,000 cm^{-1}. The band at 15,900 cm^{-1} (observed also on Fe-ZSM-5 and on

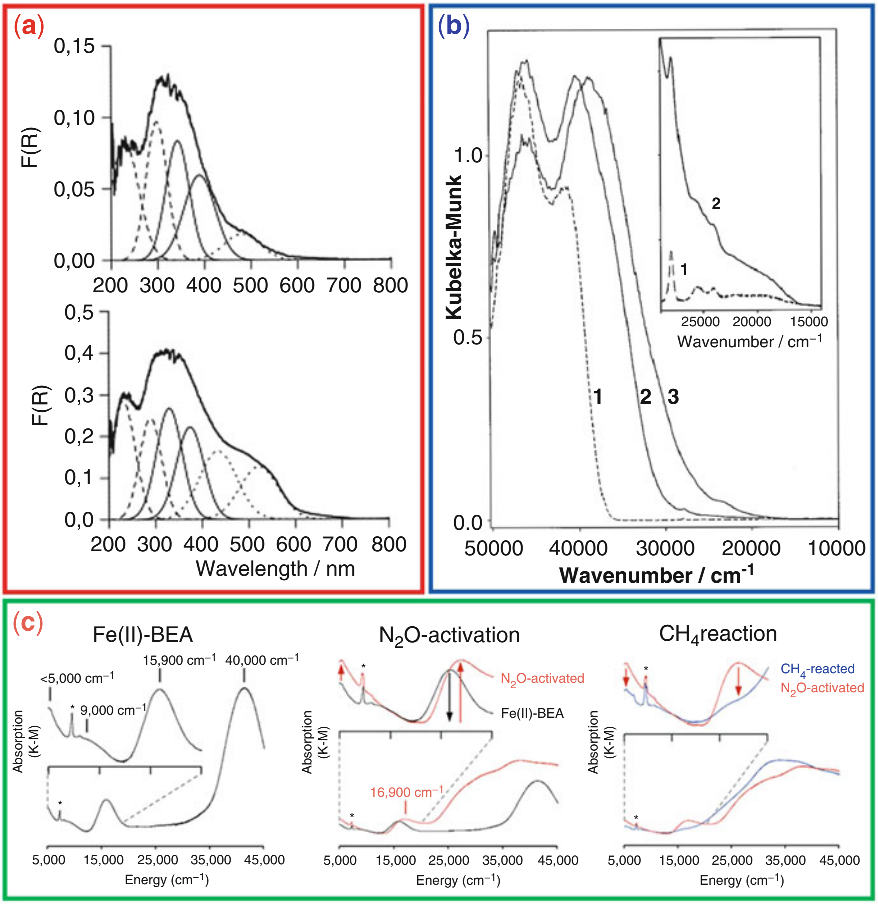

Fig. 9 Examples of DR UV-Vis spectra of Fe-zeolites. (**a**) Spectra of hydrated as-prepared Fe-ZSM-5 samples, prepared by CVD or SSIE (top and down, respectively). Thick solid lines are the experimental spectra, while thin ones are deconvoluted components assigned to: - - - isolated Fe^{III}, — small oligonuclear Fe_xO_y moieties, · · · extended Fe_2O_3-like clusters. Adapted from the Journal of Catalysis, 227, S. M. Kumar et al., On the nature of different iron sites and their catalytic role in Fe-ZSM-5 $deNO_x$ catalysts: new insights by a combined EPR and UV/VIS spectroscopic approach, 384–397, Copyright 2004, with permission from Elsevier [111]. (**b**) Spectra measured in controlled atmosphere on a Fe-silicalite sample as prepared (1) and after calcination at 500 (2) and 700°C (3). The inset reports a magnification of the weak Fe^{III} *d-d* ligand field bands, related to Fe_{fw} sites which are transformed during calcination into clustered/aggregated Fe_xO_y/Fe_2O_3 (responsible for the shift to lower energy of the LMCT absorption passing from 1 to 3) and into silent Fe^{II} sites. Reprinted from the Journal of Catalysis, 158, S. Bordiga et al., Structure and reactivity of framework and extraframework iron in Fe-silicalite as investigated by spectroscopic and physico-chemical methods, 486–501. Copyright 1996, with permission from Elsevier [98]. (**c**) Spectra of (left) reduced Fe-BEA; (middle) activation with N_2O at 250°C; (right) effect of methane interaction at RT. * = OH overtone. Adapted by permission from Macmillan Publishers Ltd.: Nature [88], Copyright 2016

Fe-FER, though with lower intensity) was shifted at 16,900 cm^{-1} upon N_2O activation at 250°C and disappeared by methane interaction at RT (Fig. 9c), supporting its assignment to α-sites.

On the basis of variable-temperature variable-field magnetic circular dichroism (VTVH-MCD), Mössbauer and DTF calculations, the authors assigned these features to a high-spin mononuclear, square planar Fe^{II} sites stabilized in a 6r BEA window [88]. The square planar configuration of the ferrous ion was proposed to be responsible for the unusual high energy of the observed ligand field band at 15,900 cm^{-1}. Moreover, DFT calculations were also in agreement with the formation of a highly covalent square-pyramidal "ferryl-like" $Fe^{IV}{=}O$ unit (Fe-O bond length 1.59 Å). This structure, unstable in the absence of the framework constraint due to the vacant *trans* axial position, would explain the high reactivity toward H-atom abstraction from methane, in agreement with the RT activity. This rigid framework constraint has been proposed to be similar to that found in some enzymes, known as the "entatic" state [88]. These breakthrough results, in favor of the mononuclear/ferryl hypothesis (structure **N** in Scheme 4), were obtained on a sample prepared by diffusion impregnation of a H-BEA zeolite with highly diluted $Fe(acac)_3$ (acac = acetylacetonate) toluene solutions, to minimize oxide/hydroxide formation. Liquid extraction of methanol resulted in 30–35 μmol of methanol per gram of zeolite (70–80% methanol yield), which is a value similar to that initially measured on Cu-CHA [72].

Finally, it is worth mentioning the use of FTIR spectroscopy coupled to NO as a probe molecule as representative technique to study the coordination environment of iron in Fe-zeolites. This experimental approach was systematically used in the group of Zecchina, to study the nature of Fe_{ef} species formed upon migration of Fe_{fw} as a consequence of calcination [9, 10, 137–139] and the effect of Al_{fw} on the Fe_{ef} sites formed in MFI [138]. Moreover, the differences between the results obtained in static and flow conditions were discussed in a joint paper with Mul [118, 120, 140].

Some representative results are reported in Fig. 10a, showing the infrared spectra in the nitrosyl region obtained during the step-wise reduction of NO equilibrium pressure (p_{NO}) on a Fe-ZSM-5 sample (prepared by ion exchange with ferric oxalate) activated in vacuum [97]. The spectra can be explained with the formation of $Fe^{II}(NO)_3$ complexes at high P_{NO} (bands at 1,846 and 1,767 cm^{-1}), evolving into $Fe^{II}(NO)_2$ (1,918 and 1,807 cm^{-1}) and $Fe^{II}NO$ ones (1,840 cm^{-1}) as a function of p_{NO} decrease. This assignment was confirmed by comparison with the nitrosyl frequencies formed in homogeneous systems (including mononuclear "heme" enzymes) or supported oxides (top panel of Fig. 10a) and by experiments with a $^{14}NO/^{15}NO$ 1:1 isotopic mixture [141]. The band around 1,880 cm^{-1} was instead assigned to $Fe^{III}NO$ adducts formed on the surface of small Fe_2O_3 aggregates, as confirmed by comparison with the spectra obtained on bulk iron oxide (see vertically translated spectrum in left-hand panel of Fig. 10b).

Figure 10b shows a comparison of the nitrosyl region of the FTIR spectra obtained on samples with different Fe loading: by increasing Fe dilution, the relative intensity of the bands related to di-/trinitrosyl adducts on Fe^{II} increases with respect to the $Fe^{III}NO$ fingerprint of oxide aggregates (band around 1,880 cm^{-1}). This series

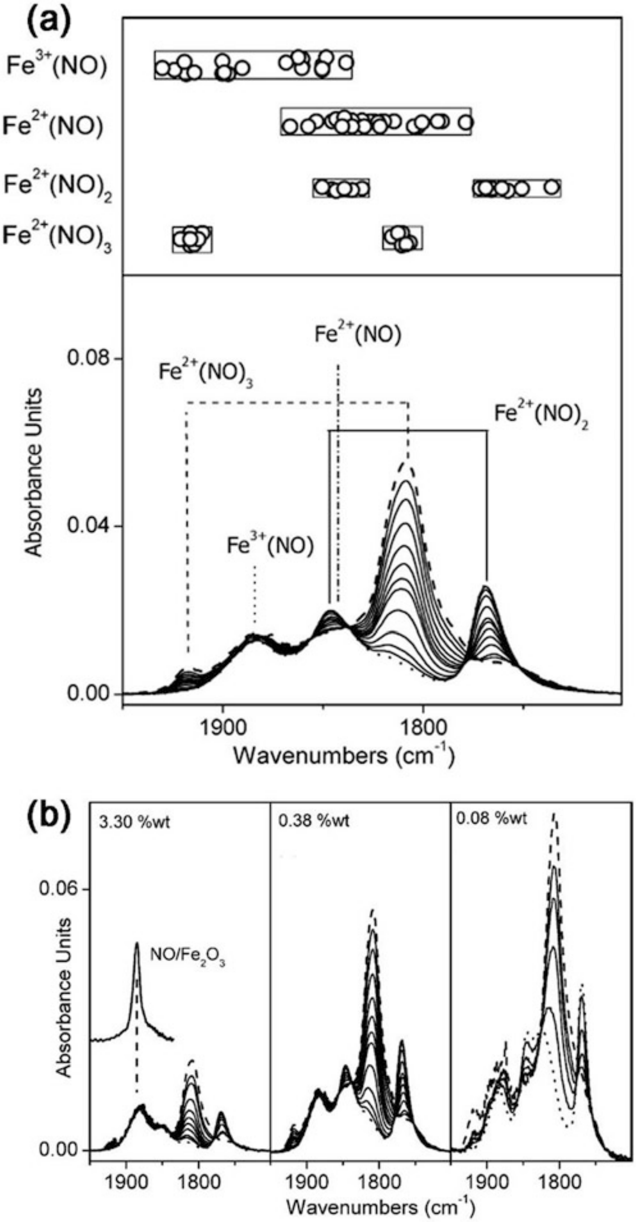

Fig. 10 (**a**) Bottom: FTIR spectra obtained upon NO adsorption at RT under static conditions (varying p_{NO} from 15 Torr, dashed line, to 10^{-3} Torr, dotted line spectrum) on a Fe-ZSM-5 sample prepared by ferric oxalate exchange and activated in vacuum; top: frequencies of Fe nitrosyl complexes in mononuclear homogeneous complexes and supported oxides (see [97]). (**b**) Series of nitrosyl spectra (same conditions and description as in part **a**) obtained on Fe-ZSM-5 samples with different Fe content (see [97] for details). The vertically translated spectrum in left-hand panel

of spectra exemplifies the potential of the technique in selectively pinpointing the presence of highly dispersed Fe^{II} sites. Indeed, the formation of trinitrosyl complexes was interpreted in terms of highly coordinatively unsaturated Fe^{II} sites grafted on the internal zeolite surface. This assignment was also confirmed by comparison with what was observed on amorphous Fe-silica [142], also using rR spectroscopy [125]. Thus, as it is seen by means of the use of NO as a probe molecule, Fe^{II} sites behave as isolated sites. This was also observed by DR-UV-Vis, resulting in relatively intense bands similar to what was observed for the mononuclear $[Fe^{II}(H_2O)_5NO]$ complexes [10]. As a final remark, one cannot in principle exclude that these monomeric sites (each able to form one α-oxygen) have other isolated Fe sites at relatively short distances, resulting in spectroscopic fingerprints compatible with the presence of dinuclear cores, as proposed by Dubkov et al. on the basis of Mössbauer and α-oxygen titration experiments (see above) [105].

3.2 H_2O_2 as Oxidizing Agent

A different reactivity of iron sites in zeolites was reported in more recent years by Hutchings' group, who carried out methane oxidation under mild conditions (50°C, 30 bar CH_4) in aqueous medium with H_2O_2 as oxidizing agent, reaching a 10% conversion with 93% selectivity to methanol [32]. The authors studied a large series of MFI zeolites, both ZSM-5 and silicalite, where Fe and Cu were inserted by different methods, particularly SSIE and hydrothermal synthesis (e.g., Fe insertion in framework positions during the synthesis). The work focused on a Fe-silicalite sample (0.5 Fe wt%), where calcination caused Fe_{fw} migration and formation of Fe_{ef} sites, as discussed above [9, 98]. On this sample, an increase in catalytic activity was observed in relation to the formation of octahedral Fe_{ef} sites, as monitored by XANES spectroscopy [32]. Based on EXAFS measurements (Fe-Fe CN = 1.6), the authors proposed a bis(μ-hydroxo)diiron complex, containing antiferromagnetically coupled high-spin octahedral Fe^{III} centers, in such a way that each Fe atom is coordinated to one additional hydroxo and water ligands, with formula $[Fe_2(\mu_2\text{-}OH)_2(OH)_2(H_2O)_2]^{II}$, thus stabilized by two negative charges on the framework.

A reaction pathway consistent with experimental data was proposed on the basis of DFT calculations, which however did not consider the framework interaction with the dinuclear core. The mechanism involved H_2O_2 coordination to one Fe^{III} atom by a water ligand displacement, evolving by H abstraction and solvent rearrangement into a formally Fe^{IV}/Fe^{II} dimer with a hydroperoxy ligand adsorbed on the Fe^{IV}

◄

Fig. 10 (continued) was obtained on an oxidized bulk Fe_2O_3 (ex-goethite), to confirm the assignment of the band around 1,880 cm^{-1} to $Fe^{III}NO$ adducts on aggregates. Reprinted from Catalysis Letters, vol 103, M.-T. Nechita et al., New precursor for the post-synthesis preparation of Fe-ZSM-5 zeolites with low iron content, pp 33–41. Copyright 2005, with permission from Elsevier [97] atom. Interaction of a second H_2O_2 molecule with the Fe^{II} site was proposed to result in a ferryl $Fe^{IV}{=}O$ (in analogy to the Fe^{II} reactivity with H_2O_2 in Fenton's chemistry), due to the absence of an adjacent ligand for H abstraction. Thus, the active site responsible for methane reaction should be a dimer with a ferryl $Fe^{IV}{=}O$ adjacent to the hydroperoxo Fe-OOH. The reaction was proposed to go through formation of methyl hydroperoxide, formed by immediate reaction of the hydroperoxy ligand with the methyl radical formed by ferryl-mediated H-abstraction, as confirmed by the absence of the EPR signals expected for the methyl radicals. On the contrary, the presence of $^{\bullet}OH$ radicals was correlated to over-oxidation reactions, which were suppressed by insertion of Cu^{II} ions [32].

Further characterization studies were carried out to better understand the nature of the Fe_{ef} sites active in the presence of H_2O_2, mainly by XANES and DR UV-Vis spectroscopy [143]. XANES was used to study the effect of thermal treatments on Fe-ZSM-5 and Al_{fw} free Fe-silicalite samples. The main presence of Fe^{III} sites on active samples was taken as an indication of the different reactivity of the H_2O_2-based catalysis with respect to the N_2O-related one, where Fe^{II} α-sites are instead formed by self-reduction during high temperature treatments under inert atmosphere. The effect of the heat treatments was then followed by UV-Vis, based on the sub-bands obtained by spectral deconvolution, as proposed by Kumar and Perez-Ramirez [111, 136]. Indeed, even if the molar extinction coefficients of each UV-Vis component is unknown, these were supposed to be of the same order of magnitude [136], thus allowing for a semiquantitative evaluation of Fe speciation. Thus, the catalytic activity was found to correlate well with the amount of Fe_{ef} dispersed in the zeolite micropores (absorptions between 250 and 350 nm), with a maximum corresponding to a calcination temperature of 750°C. Accordingly, higher calcination temperature, resulting in the formation of larger clusters and iron oxide aggregates (350–450 nm and $\geq$450 nm, respectively), caused a decrease in the amount of oxygenated products (Fig. 11a) [136].

Deconvolution of UV-Vis spectra into sub-bands for semiquantitative Fe speciation was also used to assess the effect of isomorphous framework substitution of trivalent non-catalytically active atoms (Al^{III} and Ga^{III}) in MFI. The higher activity of Fe-ZSM-5 with respect to Fe-silicalite was related to the role of Al_{fw} (and similarly to Ga_{fw}) in increasing the migration of Fe_{fw} to Fe_{ef} during calcination (in samples prepared by hydrothermal synthesis) and in maximizing the fraction of Fe_{ef} dispersed inside the micropores (bands in the 250–350 nm range) at the expenses of larger aggregates [145]. This can be explained by an inhibition effect toward clustering from the negatively charged framework, favoring the anchoring and the stabilization of dispersed sites. The authors acknowledged the fact that UV-Vis cannot discriminate alone between all the possible Fe_{ef} dispersed inside the zeolite pores (isolated Fe^{III}, dimers, trimers, and small oligomers). However, these spectroscopic features could be compatible with the $[Fe_2(\mu_2\text{-}OH)_2(OH)_2(H_2O)_2]^{II}$ core proposed on the basis of the match between XANES parameters and DFT calculations [32, 145].

Further efforts were devoted to improve the catalytic performances of Fe-zeolites in the selective oxidation of alkanes (methane and ethane) with H_2O_2 and to

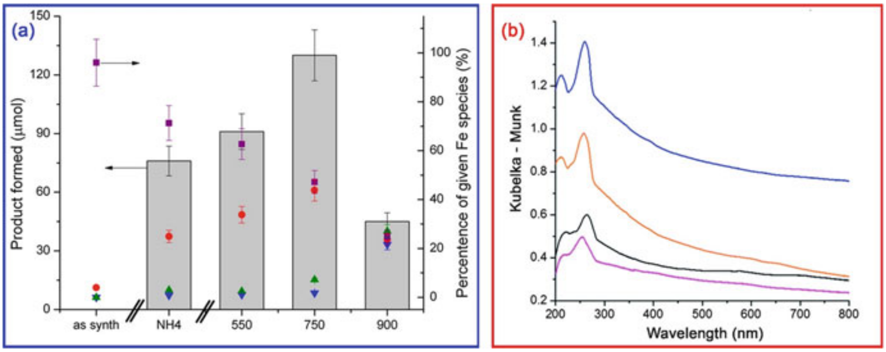

Fig. 11 (**a**) Amount of oxygenated products obtained in H_2O_2 aqueous solution (for details, see [143]) on Fe-silicalite as prepared and after thermal treatments at increasing temperature. The NH_4-form precursor is also shown for comparison. The scatter points refer to Fe speciation calculated from deconvoluted UV-Vis spectra. Key: squares, isolated, tetrahedral framework Fe; circles, extraframework Fe within the micropores; up triangles, larger Fe clusters; down triangles, bulk Fe oxides. Reprinted with permission from [143]. Copyright 2013 American Chemical Society. (**b**) DR UV-Vis spectra of Fe-ZSM-5 samples prepared by CVI from $Fe(acac)_3$ (orange, blue, black, nominal Fe loading 1.1, 2.5, and 0.4 wt%, respectively) and $Fe(acac)_2$ (pink, nominal Fe loading 0.4 wt%), heat treated at 550°C in 5% H_2/Ar for 3 h [144]. Published by the Royal Society of Chemistry, licensed under a Creative Commons Attribution 3.0 Unported License

highlight the nature of active Fe_{ef} sites. Forde et al. carried out a systematic study on a large set of Fe-ZSM-5 samples prepared by CVI with ferric and ferrous acetylacetonate precursors [144]. Interestingly, the samples were heated under hydrogen atmosphere before calcination, in order to reduce the amount of available oxygen in the micropores and thus to limit agglomeration. The samples were shown to be characterized by peculiar DR UV-Vis spectra, with well-defined bands (maxima at 215/235 and 260 nm) in the typical region for LMCT of isolated Fe^{III} sites [98], with less resolved components above 300 nm with respect to the typical Fe-zeolite samples (Fig. 11b). The authors acknowledged the fact, already discussed by Bordiga et al., that these low wavelength bands cannot be used to discriminate between Td and Oh Fe^{III} coordination, which are characterized by similar energy level diagrams [98]. In agreement with previous reports and XANES evidences, they assigned the UV-Vis bands to extraframework Fe^{III} sites in octahedral coordination, both isolated or in small clusters.

Some considerations about these characterization results are the following. First, the discussion of the peak centered at 215–235 nm is doubtful due to the low sensitivity of DR detectors in the high-energy limit, which could cause artifacts, also in relation to luminescence phenomena. Thus, it should be more prudent to consider DR UV-Vis spectra only below 250 nm, for precise band maxima description. Secondly, all the UV-Vis spectra obtained on pre-reduced catalysts appear vertically offset, i.e., although no defined bands are observed above 300 nm, spectra are characterized by an unresolved tail with absorbance never reaching zero, which could be indicative of the presence of additional, highly heterogeneous species, not detected either by TEM or XAS spectroscopy (Fig. 11b).

Notwithstanding these limitations, comparison of the spectroscopic features and catalytic performances (including ethane oxidation) of a large series of samples allowed the authors to pinpoint the novelty of the proposed preparation method, in particular in relation to the reduction treatment. Thus, the role of the previously proposed diiron-oxo-hydroxo species was partially discarded, pointing to the importance of isolated octahedral extraframework iron-oxo clusters and/or Fe^{II} sites (whose structure could not be precisely described) in directing high selectivity to alcohols, also in the absence of Cu^{II} as $^{\bullet}OH$ radical scavengers [144].

Finally, rR spectroscopy was used to study the Fe-silicalite and Fe-ZSM-5 samples previously characterized by DR UV-Vis and XAS spectroscopy [32, 145]. Hammond et al. observed three Fe-specific modes at 521, 1,120, and 1,160 cm^{-1} upon irradiation with $\lambda_{exc} = 325$ nm, that is, in correspondence to the UV-Vis electronic transitions assigned to the dispersed mono-, di-, and/or oligonuclear Fe_{ef} sites correlated to the catalytic activity [146]. In particular, the intensity of the band at 521 cm^{-1} was shown to increase with calcination temperature, reaching a maximum after treatment at 750°C, with a trend similar to that of oxygenated product formation (Fig. 11a). The authors thus questioned the previous assignment of this band by Bonino et al. and Li and coworkers to framework Fe^{III} sites [125, 147] and proposed its assignment to the extraframework $[Fe_2(\mu_2\text{-}OH)_2(OH)_2(H_2O)_2]^{II}$ core established by DFT/XAS [32]. Active Fe-silicalite was also studied in the presence of H_2O_2, showing a new band at 631 cm^{-1} resonant by irradiation in the visible range ($\lambda_{exc} = 514$ nm), which was assigned to the ν(Fe-O) stretch of a Fe^{III}-OOH complex. The 521 cm^{-1} rR band was instead shown to disappear upon H_2O_2 interaction, being regenerated upon laser irradiation or heating at 110°C. This would thus indicate a reversible shift between the di-μ-hydroxo-bridged complexes and two transient mononuclear a Fe^{III}-OOH sites, operating in a cooperative manner in the remaining catalytic cycle [146]. The flexibility of the mono and dinuclear structures would thus be in agreement with the proposed self-organization of cations in zeolites or molecular complexes [148, 149].

4 Characterization of TS-1 Zeolites

Titanium silicalite-1 (TS-1), along its 30-year history, has been widely characterized by numerous experimental techniques. In the first pioneering stages, the researchers from EniChem demonstrated the introduction of the titanium atoms in the siliceous MFI framework of silicalite-1 on the basis of three simple observations: (1) all the synthesized material, independently from their Ti loading, on the basis of diffraction experiments were isostructural with the purely siliceous silicalite-1; (2) the cell volume derived from diffraction was increasing linearly as the Ti loading increased; and (3) a characteristic infrared band, with maximum at 960 cm^{-1}, was observed in Ti-substituted materials, with an intensity linearly increasing with the Ti loading.

These findings, together with the exceptional activity and selectivity in partial oxidation reaction toward numerous organic substrates in the presence of aqueous hydrogen peroxide, brought in the 1983 to patent the synthesis of TS-1 [150].

Since these first discoveries, TS-1 was the object of several characterization studies which progressively enriched the knowledge on this material. Diffraction techniques gave time by time higher-quality results, improving both the instrumental potentialities and the ability in the sample handling [151–153]. The highest point achieved by diffraction techniques has been the attainment of the Ti distribution among the 12 possible sites of the MFI framework: these results were obtained by neutron diffraction, exploiting its superior contrast among Ti and Si atoms with respect to standard X-ray diffractometers [154, 155]. Simultaneously, even larger developments arose from spectroscopic approaches: FTIR [156–158], Raman [159–163], optical [158, 164, 165], X-ray adsorption [164, 166, 167], and emission [168, 169] spectroscopies were diffusely applied, giving rise to a constant enrichment in the understanding of TS-1 and its catalytic sites. It is important to underline that most of these studies actually exploited the complementarity among the different spectroscopic techniques, allowing a better understanding of the system as observed from different points of view.

4.1 *Characterization of Ti Sites*

UV-Vis spectroscopy is one of the most important experimental tools, together with vibrational (IR and Raman) and X-ray-based (XAS and XES) spectroscopies, employed in the study of the structure of $\mathrm{Ti^{IV}}$ active centers in TS-1, both in the absence or in the presence of adsorbates [158, 164, 170–174] and for the evaluation of the existence of both framework and extraframework Ti species [170].

The DR UV-Vis spectrum of a vacuum-activated TS-1 (black curve in the upper part of Fig. 12) is the unequivocal proof of the presence of $\mathrm{Ti^{IV}}$ sites in tetrahedral coordination inside the zeolite framework (see structure (I) in Fig. 12). The black spectrum (dehydrated TS-1) exhibits as unique feature a $\mathrm{Ti^{IV}O^{2-} \rightarrow Ti^{III}O^{-}}$ ligand to metal charge transfer (LMCT) around 200 nm ascribable to the charge transfer transition from the oxygen ligand to an unoccupied orbital of a $\mathrm{Ti^{IV}}$ ion tetrahedrally coordinated in isolated [$\mathrm{TiO_4}$] sites [160, 164, 170, 171, 174, 175], i.e., perfectly tetrahedral $\mathrm{Ti_{fw}}$ centers. The existence of a single band around 200 nm in the UV-Vis spectrum of a vacuum-activated sample can be considered as characteristic of a well-manufactured TS-1, without the presence of extraframework sixfold-coordinated Ti species ($\mathrm{Ti_{ef}}$), which give absorptions at higher wavelengths [170, 176, 177].

The peculiar tetrahedral coordination of framework $\mathrm{Ti^{IV}}$ sites in TS-1 is somewhat unusual, and for this reason, these framework Ti species can easily expand their coordination sphere upon interaction with adsorbates. In fact, it is well known that the pure tetrahedral coordination can be observed only when the TS-1 is activated under vacuum at high temperature, i.e., when all adsorbed water, acting as additional ligand, is totally removed from the material (see black spectrum of Fig. 12). When

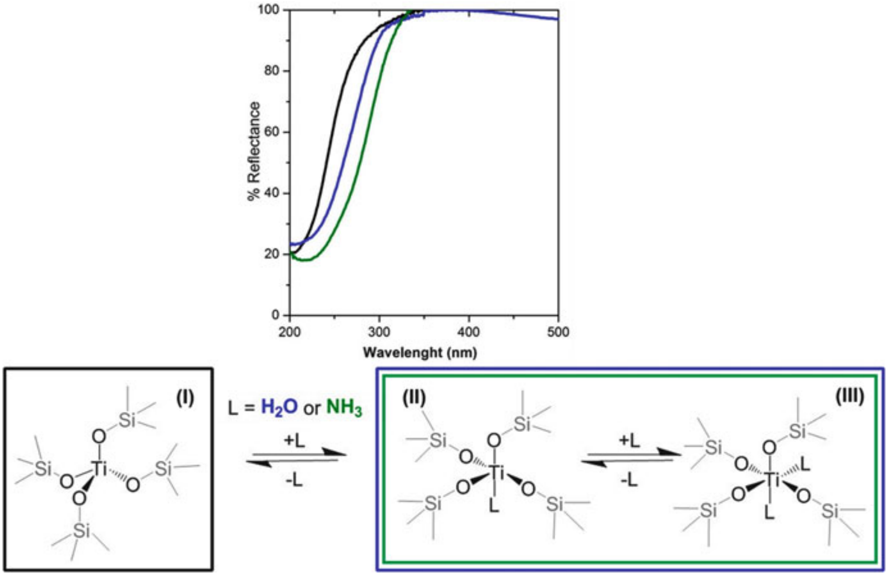

Fig. 12 Top: DR UV-Vis spectra of the TS-1 catalyst vacuum activated at 500°C (black curve) and upon interaction with H_2O (blue curve) and NH_3 (green curve) dosed from the gas phase. Bottom: ability of the Ti^{IV} site to modify its local environment from a tetrahedral-like (structure I) to an octahedral-like (structure III) geometry after interaction with strong ligands ($L = H_2O$ or NH_3), eventually involving intermediate coordination geometries (structure II)

strong ligands, such as water or ammonia, interact with the dehydrated TS-1, they are able to affect the electronic transitions of Ti sites, and therefore, the UV-Vis spectral profile undergoes evident modifications as reported in Fig. 12. The interaction with H_2O molecules from the gas phase (blue spectrum) causes a red shift of the edge, due to the increase of the coordination sphere around the Ti^{IV} centers [158]. At the same time, the interaction with NH_3 from the gas phase (green spectrum) is also responsible of an evident perturbation of the TS-1 UV-Vis spectrum [164]; however, the red shift of the edge is clearly more pronounced in this case. All these spectral variations are generated by the direct interaction of the extra ligands (adsorbates) with the Ti^{IV} atoms, due to the ability of these sites to modify their local environment in a reversible (or nearly reversible) manner from a tetrahedral coordination (structure I in Fig. 12) to an octahedral-like geometry (structure III in Fig. 12) passing through a trigonal bipyramidal coordination (structure II in Fig. 12). The progressive expansion of the Ti coordination sphere is witnessed by the gradual modification of the spectroscopic features toward those of octahedral Ti^{IV} species [156, 159, 164, 170, 174, 178, 179]. In fact, when Ti exhibits six oxygen atoms in its first coordination shell, as in the case of TiO_2 polymorphs, the $Ti^{IV}O^{2-} \rightarrow Ti^{III}O^{-}$ LMCT occurs at around 330 nm [180, 181], i.e., at higher wavelength with respect to the peculiar spectral feature of the perfect tetrahedral Ti^{IV} centers in an activated TS-1 (*ca* 200 nm).

Under the adopted experimental conditions, the interaction with H_2O or NH_3 from the gas phase does not lead to sixfold-coordinated Ti^{IV} species (structure III in Fig. 12). The maximum number of ligands can be obtained just on highly hydrated samples [173] (contacted with water from the liquid phase), in the presence of higher NH_3 pressure or by using aqueous NH_4OH solutions [164, 174].

In conclusion, it is evident that the UV-Vis spectroscopy is a very useful tool as it gives direct information on the chemical events occurring in the first coordination sphere of Ti^{IV}. In fact, by the analysis of the UV-Vis spectra, it has been possible to prove that the Ti^{IV} coordination sphere expands upon adsorption of extra ligands (adsorbates) from the surrounding atmosphere [164]. This statement will be confirmed also in the following sections by the results obtained with other different characterization techniques.

Moving to vibrational spectroscopies, Fig. 13 reports TS-1 infrared and Raman active vibrational modes in the full mid-IR 3,800–700 cm^{-1} range, in comparison with a Ti-free silicalite-1. In part (a) a typical infrared spectrum (in transmission

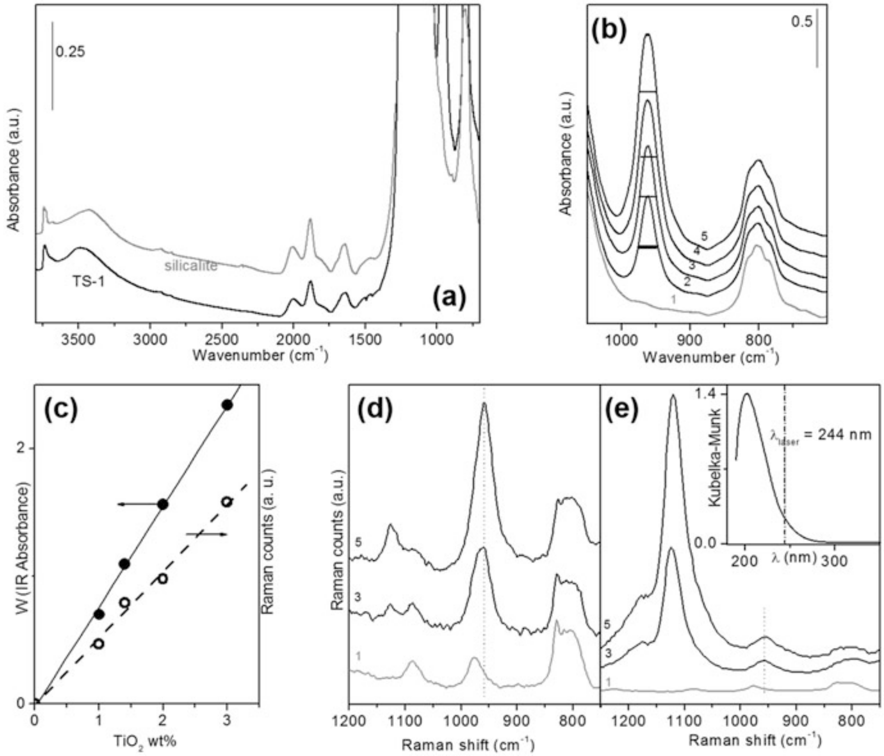

Fig. 13 Infrared (parts **a** and **b**) and Raman (part **d** $\lambda = 1{,}064$ nm and part **e** $\lambda = 244$ nm) spectra of TS-1 samples with different Ti content (black curves) and, for comparison, a silicalite sample (gray curve). Part **c** reports the infrared (full circle) and Raman (empty circle) linear correlation of 960 cm^{-1} fingerprint intensity with Ti content. Parts **b**–**e**: Adapted with permission from [157]. Copyright (2001) American Chemical Society

mode) of TS-1 activated in vacuum (black curve) is compared to the reference silicalite-1 one (gray curve). In the reported range, both spectra are dominated by hydroxyl groups and skeletal Si-O vibrational modes. As previously discussed in [182, 183], absorption bands can be roughly divided into different groups and assigned as it follows: (1) 3,800–3,650 cm^{-1} range to stretching modes of hydroxyl groups not involved in hydrogen bonding (isolated and terminal, either external and internal, OH), (2) 3,650–3,200 cm^{-1} range to stretching modes of hydrogen-bonded OH groups, (3) 2,100–1,300 cm^{-1} to overtones and combination framework modes, and (4) 1,300–700 cm^{-1} to out of scale fundamental framework modes and in particular to asymmetric (broad band centered at 1,150 cm^{-1}) and symmetric (band at 800 cm^{-1}) vibrational modes of [SiO$_4$] units. In this last range, exactly between the two previously described absorptions, a clear difference between TS-1 and silicalite-1 can be identified: the famous fingerprint at 960 cm^{-1}, again reported as an out of scale feature.

The main interest is of course the clear distinction of clear vibrational fingerprint ascribable to the presence of Ti inserted in the framework. To this aim, it is necessary to focus the attention on two different operative aspects: (1) to decrease the thickness of the samples studied in transmission or to adopt ATR modality and (2) to activate properly the samples as intensity and frequency can result distorted. A quantitative correlation between the Ti content and its infrared intensity was reported by Ricchiardi et al. [157]. Figure 13b reports the infrared spectra of four TS-1 samples containing increasing Ti content (x) (curves 2–5) in comparison with pure silicalite-1 (curve 1). In order to be quantitative, a normalization to the pure siliceous framework bands in the 1,500–2,000 cm^{-1} range (not reported in this series of spectra) has to be necessarily applied. It is worth noticing that the accuracy of the normalization procedure is testified by the perfect superimposition of the band centered at 800 cm^{-1}, again not affected by the Ti presence.

Full-width at half-maximum (FWHM) of the 960 cm^{-1} band was measured for the lowest Ti content sample (27 cm^{-1}), by assuming the band completely far from saturation, and then for all the samples, the absorbance (W), at the height where the width of the band corresponds to the fixed value, was considered (see Fig. 13c, full circles), and a linear correlation ($r = 0.9998$) was found.

The existence of the 960 cm^{-1} fingerprint and its linearity with Ti content (see Fig. 13c, empty circles) is further confirmed by Raman spectroscopy, where, in addition, saturation problems are absent. Figure 13d, e report Raman spectra of two TS-1 samples (3 and 5, already measured by means of IR spectroscopy) in comparison with a silicalite-1 sample highly defective (large amount of hydroxyl groups), collected with two different laser lines at 1,064 and 244 nm, respectively. Inset of Fig. 13e shows clearly that, by adopting the mid-UV laser line, resonance occurs as it falls in the $\mathrm{Ti^{IV}O^{2-}} \rightarrow \mathrm{Ti^{III}O^{-}}$ LMCT. It is worth noticing that the Raman spectrum of the silicalite-1 is very similar with both 1,064 nm and 244 nm laser lines as of course no resonance occurs. The features at 1,085 cm^{-1} and the broad band centered at 820 cm^{-1} are ascribable to asymmetric and symmetric vibrational modes of [SiO$_4$] units, already found in the IR spectra (see Fig. 13a). In silicalite-1 sample, the well-distinguishable band at 975 cm^{-1} must not be confused with the 960 cm^{-1}

fingerprint (see vertical lines) as it is assigned to ν_{asym}(T-O-T*), where T* is a T site where an hydroxyl group is connected. [156].

However, the most eye-catching evidence is the presence of a new band at 1,125 cm^{-1}, visible by adopting the two different laser lines and strongly enhanced by rR effect (see Fig. 13d, e). In addition to this, the constant value of the I(1,125)/I (960) ratio (0.25 in the case of 1,064 nm, 11 in the case of 244 nm laser lines) indicates that the two vibrational features are both related to the isomorphous insertion of Ti in the MFI framework. This observation finds good agreement with the work of Li et al. [160, 184], where Ti-related vibrational fingerprints are found to increase during TS-1 crystallization process.

Besides the laboratory techniques previously commented, synchrotron-based X-ray spectroscopies represent a fundamental tool in the characterization of the dispersed Ti centers in Ti-zeolites and related materials, taking advantage from their superior atomic selectivity. These have been exploited in the investigation of various aspects of TS-1 structure and chemistry, e.g., local structure of the Ti sites, their location in the MFI framework, or interaction of Ti with probe molecules of reactants.

XAS is probably the most used technique, because of the structural information it brings. Indeed, the XANES part of the spectrum is sensitive to both the oxidation state and the coordination environment of the emitting atom, whereas the EXAFS portion allows average structural parameters (e.g., bond distances, coordination numbers) to be obtained through fitting procedures.

The first XAS studies concerning Ti-zeolites was reported in 1991 by Behrens and coworkers [185]: they performed Ti K-edge measurements on TS-1 samples synthesized according to the patent recipe [151–153]. Since the quality of the EXAFS data was not sufficient for fitting, the authors focused on the qualitative analysis of the XANES data through an exhaustive comparison with various mineral references (see Fig. 14).

This strategy accounts on the comparative analysis of the pre-edge features of the XANES spectra (associated to $1s \rightarrow 3d$ electronic transitions), which are strongly indicative of the coordination sphere of Ti. When Ti sits in a tetrahedral ligands sphere, a sharp and intense peak is observed. Conversely, if Ti belongs to an octahedral environment (thus possessing an inversion center), the associated transitions will give weak contributions, since these are Laporte forbidden. Other coordination geometries (such as fivefold Ti or high distortions of octahedral/tetrahedral ligand spheres) give intermediate phenomena, with the intensity of the pre-edge peaks strongly influenced by the degree of centrosymmetry of the system. Upon linear combination of the spectra of ramsayite (containing distorted octahedral Ti), fresnoite (with Ti sitting in a square-pyramidal environment), and barium titanate (representative of Ti in tetrahedral coordination), the pre-edge peak of TS-1 was reconstructed. On the basis of this analysis, the authors claimed that Ti is inserted in TS-1 with various coordination geometries, preferentially octahedral for both the samples they considered in the study. The presence of extended Ti oxide phases was however excluded. Another relevant point was the role of hydration of the samples: indeed, a reduction of the content of octahedral species was recognized upon

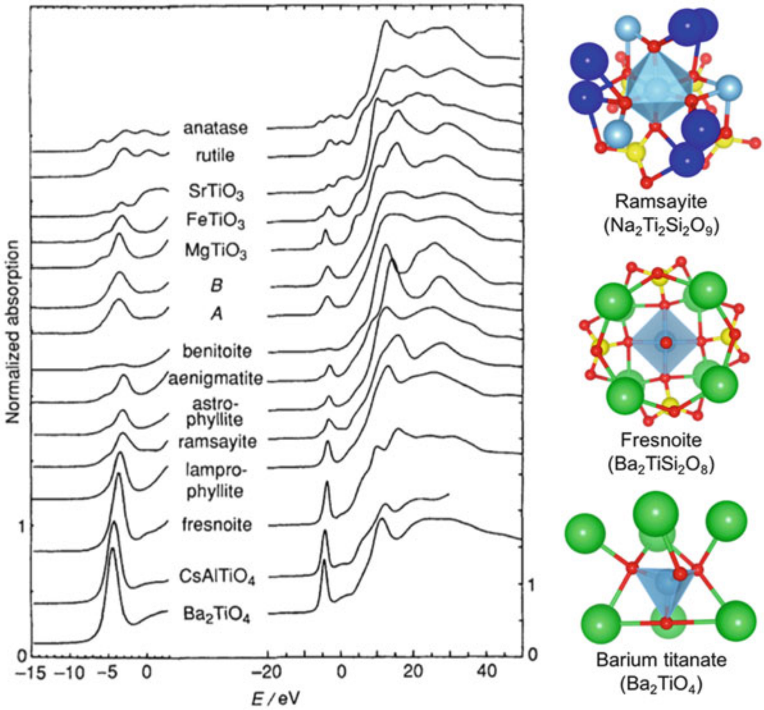

Fig. 14 Ti K-edge XANES spectra of the TS-1 sample as-synthesized (A) and calcined (B) together with those of reference compounds. Spectra are normalized to unity. The zero-point of the energy (*E*) scale was fixed at the first inflection of the K-edge of metallic Ti. Reproduced from [185] with permission of the Royal Society of Chemistry. The Ti local environment for some relevant phases is graphically outlined (Ti in cyan, Si in yellow, Na in blue, Ba in green, O in red)

dehydration, suggesting the coordination sphere of Ti can also contain ancillary ligand (e.g., adsorbed H_2O or neighbor silanol groups) which are desorbed upon appropriate treatment. Similar results were reported by Schultz et al. [186], whereas Pei and coworkers [187] for the first time pointed out that Ti is preferentially inserted as a tetrahedral substituent of Si. The latter inferred that the conclusions from previous reports where biased by the use of a poor-quality sample (i.e., with unexpectedly abundant Ti_{ef} content). With respect to previous reports, they carried out fitting of the EXAFS data, since the pre-edge XANES features alone were not sufficient to unambiguously determine the Ti coordination. The EXAFS analysis revealed a coordination number of 4.1 ± 0.5 for Ti in the first coordination shell, suggesting it preferentially occupies tetrahedral positions. However, due to the large error affecting the result, a five-ligand first coordination sphere cannot be excluded a priori. The final confirmation on the fourfold, almost perfectly tetrahedral first coordination sphere of Ti arose from the works from Lamberti and coworkers [18, 164, 166, 167, 188, 189]: a key step was represented by the careful dehydration procedure (i.e., outgassing at high temperature) they performed on well-

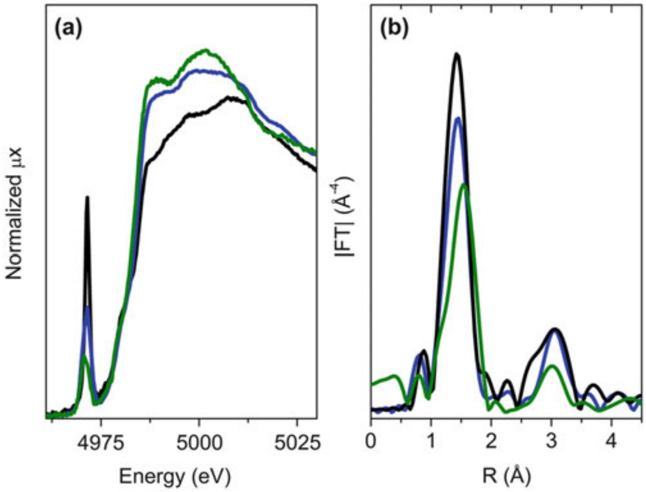

Fig. 15 (**a**) XANES spectra and (**b**) k^3-weighted module Fourier transform of the EXAFS signal for dehydrated TS-1 (black lines), dehydrated TS-1 contacted with H_2O (blue lines), and dehydrated TS-1 contacted with NH_3 (green lines). Unpublished figures reporting data previously published in [167]

manufactured TS-1 samples, thus excluding the influence of the ligands on the local environment of Ti, as well as avoiding the presence of misleading extraframework species. As a cross-check, basic molecules (e.g., H_2O, NH_3) were dosed from the gas phase over the activated materials in order to restore a "hydrated-like" state of the sample. A summary of the main results is given in Fig. 15.

Upon dehydration, the intensity of the *1s* → *3d* peak rises up to an intensity comparable to the white line one, consistently with the establishment of an almost perfect tetrahedral environment for the Ti sites. Upon dosage of H_2O (and even more evidently with NH_3), the intensity of the pre-edge feature decreases by a large extent, testifying the increase of the coordination of Ti toward a more centrosymmetric ligands field. The fit of the EXAFS data further allowed obtaining the Ti-O distances and the number first neighbors of the emitting center: in the case of the bare tetrahedral site, the Ti-O distance was found to be 1.79 ± 0.01 Å, and the coordination number in the first shell resulted to be 4.3 ± 0.3. This latter result definitely demonstrates the preferential tetrahedral coordination of Ti in well-manufactured TS-1, without excluding that a fraction of higher coordination/defective site could however be present. Upon adsorption, the Ti-O distance consistently increases to 1.82 ± 0.02 and 1.88 ± 0.02 Å for H_2O and NH_3, respectively. For the latter molecule, the coordination number relative to N atoms linked to Ti was computed (assuming the number of surrounding O atoms fixed to 4): a value of 1.9 ± 0.3 was found, suggesting that Ti assumes an octahedral coordination at high NH_3 coverages. This last point also confirms the relevance of the activation procedure, since the presence of ancillary ligands adsorbed at the Ti sites has a major effect in determining their XAS features.

Beside the structural information provided by XAS, more recently new insights arose from emission-based techniques, such as X-ray emission spectroscopy (XES). XES allows deeply investigating the electronic features of the sample through a second-order optical process, where (1) an electron is removed from a core level of the emitting atom by the interaction with X-rays and (2) another electron from a higher energy shell fills the vacancy left from the previous, leading to the emission of a photon with characteristic energy. When the filling electron comes from a valence level, the technique is referred as valence-to-core XES (vtc-XES): this has been successfully applied to the characterization of TS-1. The main contributions belong to Gallo et al., who focused on the properties of the bare TS-1 [169], also in interaction with H_2O/NH_3 [168]. The former work elucidated the feasibility of the interpretation of vtc-XES data through a DFT approach, underlining the importance of the structural model and level of theory in the simulation of the emission spectra. On the basis of these results, the latter work exploited the electronic information to derive a more structural insight, i.e., the type of coordination assumed by Ti centers in the presence of basic ligands. This study exploited a further advanced tool, i.e., resonant vtc-XES (rvtc-XES, also referred as resonant inelastic X-ray scattering, RIXS). With respect to regular vtc-XES, rvtc-XES is performed recording the emission profile as a function of the energy of the incident beam, usually in the energy range surrounding a pre-edge feature of the XANES spectrum (in the case of TS-1, the intense *1s* → *3d* peak). In Fig. 16, the case of NH_3 adsorption is reported as an example.

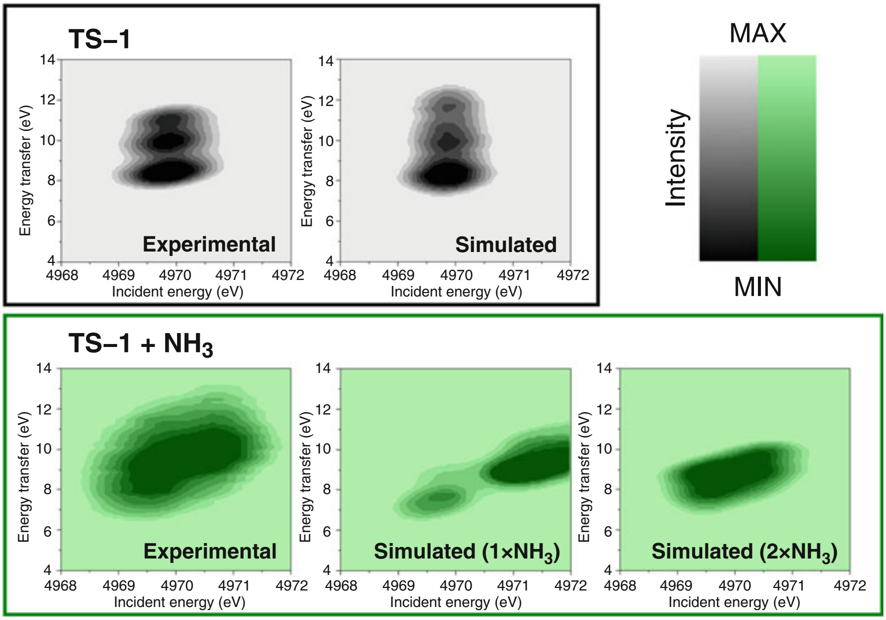

Fig. 16 Experimental rvtc-XES maps of TS-1 (bare and contacted with NH_3) compared with simulations. In the case of NH_3, both single and double NH_3 adsorption at the Ti site have been considered. Unpublished figures reporting data previously published in [168]

Comparison of the experimental rvtc-XES maps with the simulated ones demonstrates (in the case of the bare TS-1) a good agreement of the model with the real system. With respect to NH_3 adsorption, this allowed inferring that the coordination of Ti is most probably fivefold (i.e., allowing the adsorption of a single ligand). Even if this could seem a barely fundamental detail, it could represent a significant datum concerning the catalytic properties of TS-1: indeed, the formation of (hydro)peroxo species upon interaction with H_2O_2/H_2O is most probably affected by the adsorption capability of each Ti site. Furthermore, this outcome sets a discrepancy with respect to previous findings, since a double adsorption was always reported by other techniques [158, 164, 166, 188]. However, it is worth noticing that vtc-XES (and even more rvtc-XES) measurements require a prolonged exposure to the X-rays beam, approximately one order of magnitude longer than in a XAS measurement. Thus, the potential beam damage (or even a simple local heating of the sample) should be taken into account considering this type of data, since it could alter the measured system (and thus the spectroscopic outcome).

4.2 *Characterization of Ti-H_2O_2 Adducts*

TS-1 is an important selective catalyst in low temperature partial oxidation reactions, with aqueous H_2O_2 as the oxidant agent. For this reason, the systematic investigation of the different active species formed in TS-1 upon interaction with hydrogen peroxide is a high priority target. One of the main experimental problems observed in the study of these active species is due to the use of H_2O_2 solutions. The presence of H_2O does not allow the extended use of IR spectroscopy; therefore, DR UV-Vis spectroscopy (not affected by the presence of H_2O) becomes one of the most important experimental techniques in this type of study, due to the possibility to obtain reliable spectra also in the presence of samples fully immersed in water solutions [158, 173, 174].

As previously explained, Ti^{IV} sites exhibit a high propensity to expand their coordination sphere under the action of reactants. The interaction with hydrogen peroxide can also modify the coordination of Ti atoms, leading to the formation of Ti-peroxo species, without the extraction of Ti from the zeolite framework [173, 190]. It is clear that the identification of these active species, formed in the presence of the TS-1/H_2O/H_2O_2 system, and the understanding of how they are affected by the presence of water molecules become key factors when TS-1 works as catalyst in the presence of aqueous H_2O_2. In particular, the study of the effect of H_2O on the nature, the equilibrium, and the stability of the Ti-peroxo species formed on TS-1 assumes great importance.

In this context, the evaluation of TS-1 behavior in the presence of H_2O from the liquid phase becomes essential. Figure 17a reports the DR UV-Vis spectra of TS-1 without activation (as such in air – black curve) and after interaction with water from the liquid phase (blue curve). The spectrum of the nonactivated TS-1 is characterized by a $Ti^{IV}O^{2-} \rightarrow Ti^{III}O^{-}$ LMCT slightly red shifted (220 nm) with respect to that

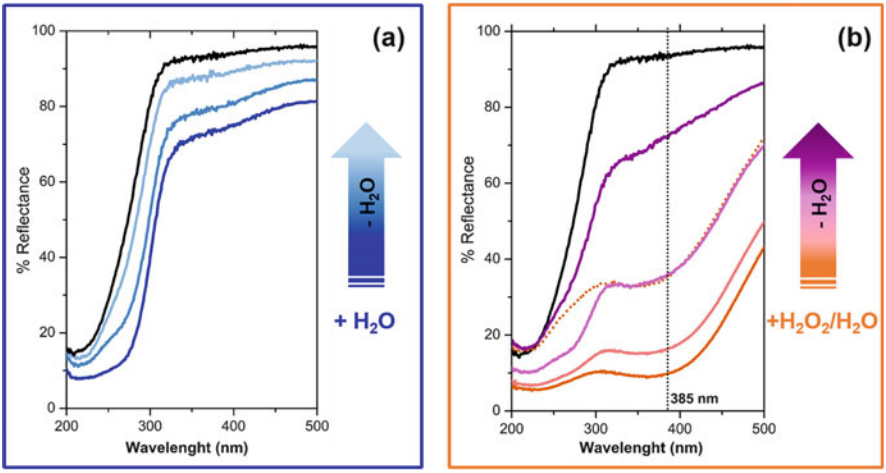

Fig. 17 Section (**a**): DR UV-Vis spectra of the TS-1 catalyst as such in air (black curve), after having been contacted with H_2O drops (blue curve) and after H_2O desorption upon time-lapse in air of 24 h and 7 days (light blue curves). Section (**b**): DR UV-Vis spectra of the TS-1 catalyst as such in air (black curve) and after contact with H_2O_2/H_2O (30 wt%) solution (orange curve). Light orange, pink, and purple curves report the effect of time-lapse in air after 10 h, 24 h, and 15 days, respectively. The orange dotted spectrum refers to the spectrum collected after the longer time elapsed in air (15 days – purple spectrum) upon dosage with H_2O in liquid phase. Unpublished figures reporting data previously published in [173]

measured on the activated material (*ca* 200 nm) because it still contains a fraction of water adsorbed from the atmosphere [173]. After the contact with H_2O drops, a further red shift of the $Ti^{IV}O^{2-} \rightarrow Ti^{III}O^{-}$ LMCT (now at around 280 nm) is observed, due to the increase of the coordination number of Ti^{IV} centers up to six [164]. These spectral modifications are combined with a consistent reduction of the reflectance signal in the whole 300–550 nm range due to the presence of liquid water in the space between adjacent zeolite crystals that causes a reduction of the scattering power of the sample. The following time evolution (light blue curves) of the UV-Vis spectra of TS-1 after interaction with water from the liquid phase shows the progressive evaporation of water molecules. It is evident that these spectra (light blue curves) progressively move toward the spectrum of the nonactivated material (black). The complexity of the spectra collected upon time-lapse in air reflects the heterogeneity of the atoms present in the first coordination sphere of Ti^{IV}, i.e., both chemically bonded framework oxygen atoms and weakly interacting oxygen atoms of physically adsorbed H_2O [158, 191].

Figure 17b reports the DR UV-Vis spectra obtained upon contact of some drops of a 30 wt% H_2O_2/H_2O solution (orange curve) on a nonactivated TS-1 (black curve). A dramatic modification of the spectral features is evident due to the appearance of a new component at around 385 nm. This band can be ascribed to the LMCT of a “side-on” peroxo ligand to the Ti center of the catalyst which confers

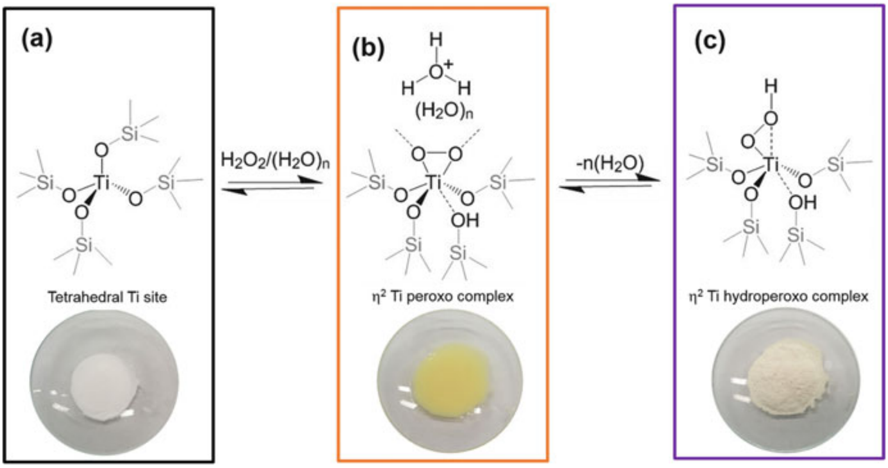

Fig. 18 Schematic representation of the equilibria between tetrahedral Ti^{IV} framework species and "side-on" η^2 Ti-peroxo complexes inside the TS-1 channels upon contact with a H_2O_2/H_2O solution (pictures (**a**) and (**b**)) and between "side-on" η^2 Ti-peroxo and "end-on" Ti-hydroperoxo complexes upon dehydration (pictures (**b**) and (**c**)). The images in the bottom refer to the typical color observed for the TS-1 powder when different complexes with H_2O_2 are formed

to the catalyst a typical yellow color [161, 162, 165, 167, 173, 190], as reported in Fig. 18b.

Clear spectral modifications are evident due to the effect of the progressive water desorption deriving from times elapsed in air of 10 h, 24 h, and 15 days (see Fig. 17b: light orange, pink, and purple spectra, respectively). In fact, upon dehydration, a gradual loss of the yellow color is accompanied by the decrease of the band at 385 nm testifying the progressive consumption of the yellow Ti-peroxo complexes ("side-on" η^2 Ti-peroxo complexes) characterized by a very low stability in the absence of a water excess. The purple spectrum in Fig. 17b reports the effect of a long dehydration time (15 days elapsed in air). In this case, the UV-Vis spectral profile is very similar to that of the material in air without activation (black spectrum); however, some absorption is still present in the 285–485 nm range. The present manifestation reflects the existence of peculiar species, only reversible upon calcination at high temperature. This resistant fraction corresponds to the stable "end-on" η^2 Ti-hydroperoxo complexes, prevailing at low water content and conferring a cream color to the TS-1 powder (Fig. 18c) [161, 162, 167, 173, 190]. Bonino et al. reported that these residual stable species are poorly reactive toward organic substrates [173].

Interestingly, dosing H_2O in the liquid phase on the sample previously contacted with H_2O_2 and then aged for long time in air, it is possible to observe that the component at 385 nm is partially restored, together with the typical yellow color. It means that the yellow "side-on" Ti-peroxo complex is stable only in the presence of an excess of water and, moreover, that the process exhibits a clear reversibility, so proving that the presence of water plays an important role in determining the ratio between the hydroperoxo and the peroxo Ti species on the working catalyst (see equilibria depicted in Fig. 18b, c) [161, 162, 167, 173, 190].

Bonino et al. [173] also proved that the interaction with hydrogen peroxide is not responsible for an extensive damage of the framework tetrahedral Ti^{IV} sites of the TS-1, as in contrast it usually occurs in the presence of Ti^{IV} grafted species (as in the case of Ti-MCM-41 silica) [192]. In fact, after a preliminary contact with H_2O_2 and a long dehydration in air, the "side-on" Ti-peroxo complexes are formed again upon further addition of a H_2O_2 solution. Bonino and coworkers reported that only a small fraction (about 10%) of Ti^{IV} is involved in the formation of very stable species (the cream colored Ti-hydroperoxo species of Fig. 18c) which, in any case, can be removed upon activation at 400°C [173].

Further insights on active Ti-(hydro)peroxo specie arose from vibrational techniques. However, the detection of infrared fingerprints of Ti-peroxo species (formed upon interaction with H_2O_2/H_2O solution) is a very hard task, as, in standard conditions, the infrared highly active modes of the great amount of water overshadow all the other infrared vibrational modes.

Tozzola et al. [159] focused their attention only on peroxo species infrared active modes (see Fig. 19a). Neutral solution of H_2O_2 (curve 2, left part of Fig. 19a) was dosed at -40°C on activated TS-1 (curve 1, left part of Fig. 19a) and a band centered at 880 cm^{-1} grew up. Since a band at 876 cm^{-1} also appears on Ti-free, on silicalite-1, and being ν(O-O) of liquid H_2O_2 at 875 cm^{-1}, this feature is obviously assigned to physisorbed H_2O_2, mainly present in TS-1 channels.

Upon interaction at -160°C with basic aqueous solutions of H_2O_2 (NH_3/H_2O_2 or $NaOH/H_2O_2$), a new infrared band at 864 cm^{-1} can be appreciated in both cases (dotted curves). The subsequent heating of the sample at about -40°C with a parallel continuous decrease of the equilibrium pressure (Fig. 19a, curve 3) leads to the appearance of another band at 836 cm^{-1}, present, this time, only in TS-1 sample. If the temperature is further increased, the band completely disappears, probably because of thermal lability of the formed species. This feature was considered to be a real fingerprint of Ti-peroxo active species stabilized in basic conditions. It is fundamental to notice that the band can be detected only in a small range of temperatures and in the presence of a small amount of water. Hence the adoption of a particular experimental procedure is fundamental in the spectroscopic identification of labile complexes, as expected for an active species in catalysis.

The existence of Ti-peroxo species was further proved by Lin et al. [193] by means of $H_2{}^{18}O_2$ and photolysis of the complex (see Fig. 19b). In this case, a band not present in silicalite-1 (at 837 or 793 cm^{-1} in the case of $H_2{}^{18}O_2$) is observed when the sample, previously contacted with hydrogen peroxide, is evacuated for 12 h (upper part of Fig. 19b). Another proof for the existence of the complex is given by irradiating at 355 nm the formed Ti-peroxo complex and by observing the erosion of the 837 and 793 cm^{-1} bands (lower part of Fig. 19b), the formation of titanol groups (spectral range not shown for sake of brevity), and the consequent formation of oxygen gas.

Bordiga et al. [161] reported a very exhaustive study of Ti-peroxo species in TS-1 by exploiting rR spectroscopy potentialities. Since Ti-peroxo complexes are colored species (see Fig. 18b), a laser source in the corresponding spectral range should be used to enhance the Raman vibrational modes associated to the active species and fulfilling the selection rules.

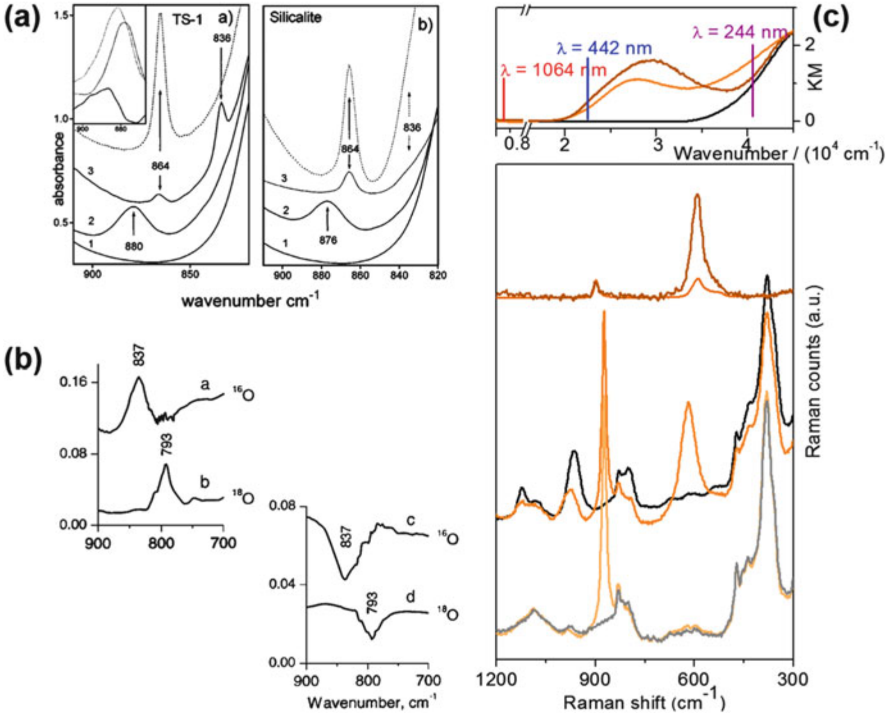

Fig. 19 Infrared (parts **a** and **b**) and Raman spectra (part **c**) of TS-1 interacting with H_2O_2/H_2O. Part **a** shows a comparison between TS-1 and silicalite-1, reporting: dehydrated samples (curves 1), after interaction with H_2O_2/H_2O at −40°C (curves 2), after contact with a solution of NH_3/H_2O_2 at −160°C (dotted curves), and after subsequent heating of the sample at −40°C with parallel outgassing (curves 3). Reprinted from the Journal of Catalysis, vol 179, Tozzola et al., On the structure of the active site of Ti-silicalite in reactions with hydrogen peroxide: A vibrational and computational study, pp 64–71, Copyright 1998, with permission from Elsevier. Part (**b**): TS-1 interacting with aqueous $H_2{}^{16}O_2$ (curve a) and $H_2{}^{18}O_2$ (curve b) and outgassed for 12 h (top); difference spectra recorded after 20 min irradiation of samples a and b at 355 nm (45 $mWcm^{-2}$) (bottom). Adapted with permission from [193]. Copyright 2002 American Chemical Society. Part (**c**): DR-UV-Vis spectra of a TS-1 sample in vacuo (black curve), in contact with a H_2O_2/H_2O solution (orange curve), and of $[NH_4{}^+]_3[TiF_5O_2]^{3-}$ (brown curve) (upper part); Raman spectra of $[NH_4{}^+]_3[TiF_5O_2]^{3-}$ ($\lambda = 1{,}064$ nm dark orange curve and $\lambda = 442$ nm brown curve), pure TS-1 (black curve) and interacting with H_2O_2/H_2O (orange curve), pure silicalite-1 (gray curve) and interacting with H_2O_2/H_2O (light orange curve) (lower part). Adapted from [161] Wiley VCH, under the Creative Commons Attribution License (CC-BY). © 2002 WILEY-VCH Verlag GmbH & Co. KGaA, Weinheim

In this respect, these authors [161] adopted the 442 nm laser line, and they observed for the first time a new band at 618 cm^{-1} (see the central orange curve in Fig. 19c), together with some features already found when a laser line at 1,064 nm was adopted [159]: (1) the decrease and blue shift of the 960 cm^{-1} band, (2) the quenching of 1,125 cm^{-1} fingerprint because of the loss of the tetrahedral symmetry, and (3) the appearance of an intense feature at 875 cm^{-1} due to ν(O-O) of physisorbed H_2O_2 solution in the channels.

To properly assign the new feature at 618 cm^{-1}, rR spectra were measured: (1) silicalite-1 in contact with H_2O_2/H_2O solution (see light orange spectrum in the bottom of Fig. 19c), which gave the band at 875 cm^{-1}, already found in the reported infrared spectra, ascribable to ν(O-O) of hydrogen peroxide physisorbed in the channels, and (2) the $[NH_4^+]_3[TiF_5O_2]^{3-}$ model compound, which showed a very intense band at 595 cm^{-1} undergoing a distinct enhancement when the 442 nm excitation source is used (see brown curve in comparison with dark orange in the upper part of Fig. 19c). The last detected feature was unambiguously assigned to the symmetric breathing mode of the $Ti(O)_2$ cycle present in the crystalline structure of $[NH_4^+]_3[TiF_5O_2]^{3-}$ consisting of TiF_5O_2 units intercalated with NH^{4+} counterions. The similarity between rR and UV-Vis spectra of the model compound and Ti-peroxo species formed in TS-1 contacted with H_2O_2 aqueous solution brings to the conclusion that the species giving an electronic absorption band at 385 nm and a rR mode at 618 cm^{-1} have a side-on geometry as in the $[NH_4^+]_3[TiF_5O_2]^{3-}$ model salt.

As in the case of the bare Ti sites, the use of X-ray spectroscopies in the characterization of active sites in TS-1 (i.e., Ti adducts with H_2O_2) gave a further relevant piece of information toward the understanding of their structure and properties. Indeed, (a) IR studies were carried out in model conditions, fairly reproducing the real reaction environment of TS-1, and (b) rR gave direct access only to the highly symmetric Ti-peroxo species, whereas no information about the peculiar features of the Ti-hydroperoxo moieties can be obtained. Even if XAS represents an optimal tool in the study of Ti-(hydro)peroxo, particular care has to be put in the preservation of the samples, since the already commented lability of these active species could result in their modification under the intense X-rays beam (i.e., they could suffer beam damage). A strategy allowing this undesired side effect to be avoided is represented by cryogenic measurement of the active moieties [173]: the stability of Ti-(hydro)peroxo is logically much higher at liquid N_2 temperature (-196°C), thus allowing the XAS data acquisition to be performed without altering the material. A key point of such procedure is the correct evacuation of the cryostat from air, in order to avoid the desorption of H_2O_2/H_2O before these are stabilized at low temperature. The best strategy has been found in a first cooling stage down to moderate temperature (about 0°C) in air, followed by evacuation and finally by the principal cooling phase toward -196°C. Following this methodology, Prestipino et al. reported an in-depth study of the Ti-peroxo/Ti-hydroperoxo equilibrium as a function of hydration (see Fig. 18b, c) [190]. A further advance achieved in this work was the dosage of nearby anhydrous H_2O_2 vapors, generated through the decomposition of its complex with monobasic potassium phosphate (KH_2PO_4), prepared according to patent literature [194]. When TS-1 is contacted with an aqueous solution of H_2O_2 (Path A in Fig. 20), the XANES spectrum is deeply altered in

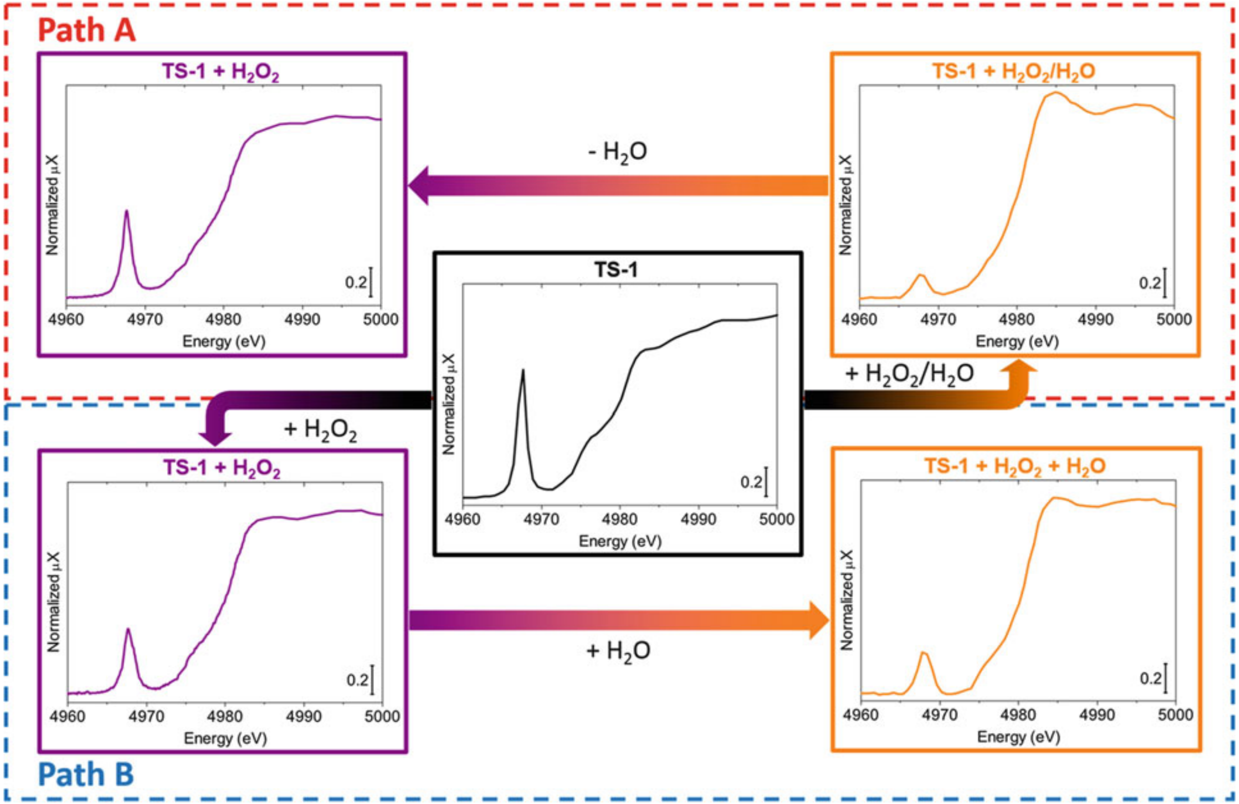

Fig. 20 XANES study of the Ti-peroxo/Ti-hydroperoxo equilibrium as a function of hydration, performed through two different strategies. Path A: from “liquid phase,” forming the Ti-peroxo species from a H_2O_2/H_2O solution and thus dehydrating by H_2O sublimation at −196°C. Path B: from “gas phase,” dosing H_2O_2 from decomposition of its adduct with KH_2PO_4 [194] and then hydrating the sample with H_2O vapor. Unpublished figures reporting data previously published in [190]

comparison with the one of the activated material. The most evident modification in the spectrum is the drop of the pre-edge feature intensity down to ~25% of the original one, with a simultaneous increase of FWHM. Such spectral evolution is a strong evidence of the change in the coordination of Ti, definitely altered from the original tetrahedral environment of the bare TS-1. Furthermore, in the edge region, two prominent maxima appear, ascribed to the formation of the side-on Ti-peroxo species [173].

Upon dehydration (achieved through vacuum sublimation of H_2O at cryogenic temperatures), the pre-edge peak is partially recovered, and the edge maxima decrease toward a flat, unresolved spectrum. Such equilibrium is perfectly reversible, since a dosage of H_2O from gas phase fully restores the previous situation. This insight suggests that the spectrum achieved upon dehydration does not generate from the decomposition of the Ti-peroxo adduct, whereas it most probably accounts for its transformation toward a different structure, possibly a Ti-hydroperoxo. This assumption was checked comparing the spectrum of the supposed Ti-hydroperoxo on TS-1 with the one obtained contacting Ti-MSA (an amorphous, mesoporous Ti silicate) [195, 196] with *tert*-butyl hydroperoxide dissolved in an anhydrous solvent, where a nice overlap was observed. The choice of Ti-MSA was due to the need of a wide porosity system (indeed, the micropores of a regular TS-1 do not allow the diffusion of the *tert*-butyl hydroperoxide to reach the Ti sites) having Ti sites mimicking TS-1 ones. As a further cross-check, the activated TS-1 was contacted with anhydrous H_2O_2 vapor (Path B of Fig. 20), with the aim to verify if the same species previously observed are generated. This was actually the finding, since the spectrum closely resembles the one obtained upon dehydration along Path A. Finally, the dosage of H_2O vapor allowed to produce again Ti-peroxo species, testifying the reliability of the proposed Ti-peroxo/Ti-hydroperoxo equilibrium.

4.3 *Characterization of Amorphous Ti Species*

Besides the characterization of the perfect tetrahedral framework Ti^{IV} sites and their adducts with hydrogen peroxide, the study of the "non-perfect" Ti species (the so-called "amorphous" species) is assuming increasing attention, in order to explain their possible role in catalysis. The nature of these amorphous species can be investigated by means of DR UV-Vis spectroscopy [163, 177, 197].

Su et al. reported the DR UV-Vis spectra of various TS-1 samples characterized by the presence of different Ti species (Fig. 21a) [176]. Three clear absorptions are evident at 200–220, 260–280, and 310–330 nm. The first one is assigned to framework tetrahedral Ti species, whereas the last one can be ascribed to a polymorph of bulk TiO_2. The band in the 260–280 nm spectral range, instead, is derived from the presence of a fraction of peculiar amorphous Ti species that the authors termed non-framework (NFW) Ti species, i.e., Ti oligomers containing hexacoordinated Ti-O-Ti structure.

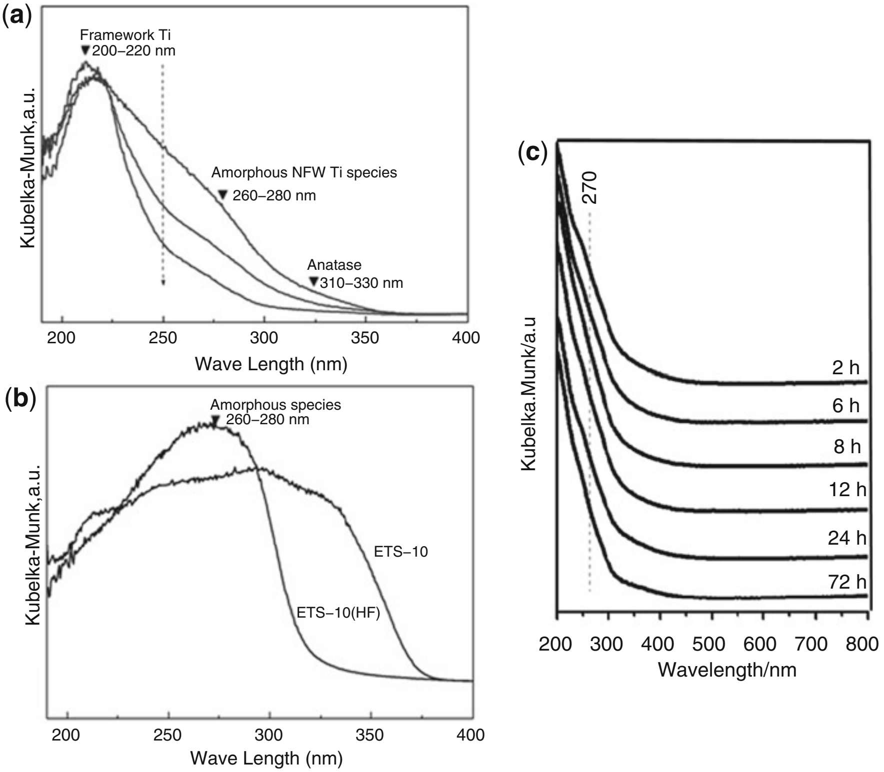

Fig. 21 Section (**a**): DR UV-Vis spectra of different TS-1 catalysts collected without activation. Section (**b**): DR UV-Vis spectra of an ETS-10 sample and of an ETS-10 corroded with a 7 wt.% HF solution. Reprinted from the Journal of Catalysis, vol 288, Su et al., Amorphous Ti species in titanium silicalite-1: Structural features, chemical properties, and inactivation with sulfosalt, pp 1–7, Copyright 2012 with permission from Elsevier [176]. Section (**c**): DR UV-Vis spectra of a TS-1 zeolite (Si/Ti = 50) for different crystallization stages at various times of synthesis. Reprinted with permission from [163]. Copyright 2013 American Chemical Society

In order to confirm their statements, Su and coworkers tried to imitate the structure of these amorphous species by corroding the framework of an ETS-10 titanosilicate with HF solutions. The framework of this titanosilicate is constituted by linear chains of corner-shared TiO_6 octahedra linked by corner-shared SiO_4 tetrahedra [198]. By corroding the ETS-10 framework with a 7 wt.% HF solution, the hexacoordinated Ti-O-Ti chains can be broken up into smaller ones, reproducing in some way the hexacoordinated amorphous NFW Ti-O-Ti species. The DR UV-Vis spectra of an ETS-10 powder before and after the corrosion process with HF are reported in Fig. 21b. It is evident that the amorphous Ti species obtained from the degradation of the ETS-10 are responsible for the appearance of a band centered at around 280 nm.

The intensity of the absorption band generated by NFW amorphous Ti species at around 280 nm obviously increases by decreasing the Si/Ti ratio in the TS-1 [177].

The evolution of different titanium species during the crystallization process of the TS-1 zeolite has been monitored by Guo and coworkers. Figure 21c reports the DR UV-Vis spectra of a TS-1 (Si/Ti = 50) for different crystallization stages at various times of the hydrothermal treatment [163]. All the spectra collected at different time intervals exhibit a similar spectral profile: a strong signal at 210 nm generated by the framework tetrahedral Ti^{IV} sites and a shoulder at 270 nm due to the NFW octahedral amorphous Ti species [197]. This weak shoulder seems to gradually decrease by increasing the crystallization time. Guo et al. tried to explain this phenomenon affirming that a small fraction of tetrahedral Ti species can be "extruded" in the form of isolated amorphous Ti species in octahedral coordination during the framework formation. This species are attached to the solid phase and dissolved into the liquid phase when the coordination environment of the framework Ti centers becomes gradually more rigid [163].

rR spectroscopy was adopted by Guo et al. [197] to characterize the active species formed in two different TS-1 samples: TS-1A and TS-1B (derived from TS-1A upon treatment with NH_4HF_2 and H_2O_2). From the DR UV-Vis spectra of the two samples, it is evident that TS-1B sample shows clearly a new component at 270 nm besides the well-known feature at around 200 nm expected for LMCT of tetrahedral framework Ti. As 244 nm laser line gives rise to resonance for tetrahedral Ti, 266 nm laser line should enhance Raman active vibrational modes of the new detected species, identified as NFW amorphous Ti species [163, 176]. In the case of TS-1B sample, a new intense band appears at 695 cm^{-1} in its rR spectrum. This new signal, not present in a sample showing all the Ti inserted in the framework (e.g. TS-1A), is ascribed to Raman active vibrational modes of the amorphous species giving rise to the electron transition at 270 nm.

To study in depth the structure of the active species and their behavior in the olefin epoxidation reaction, the two samples were also investigated in contact with H_2O_2/H_2O solution to form the active species and then with propylene as a probe reactant, by using UV Raman ($\lambda = 325$ nm) spectroscopy. The active species formed in TS-1A sample shows the same Raman features.

Subsequent interaction with propylene at 60°C gives rise to new Raman bands at 725, 820, 890, 945, 1,021, 1,095, 1,168, and 1,265 cm^{-1}, ascribable to the formation of propylene oxide, whereas the bands at 615 and 875 cm^{-1} disappear and the fingerprint at 1,125 cm^{-1} is restored. This result clearly testifies the formation of active species, upon interaction with H_2O_2/H_2O solution, able to partially oxidize propylene to form propylene oxide.

The same experiment was performed on TS-1B. Upon interaction with H_2O_2/H_2O solution, the already discussed Raman bands at 615 and 875 cm^{-1} appear and the 695 and 1,125 cm^{-1} bands decrease in intensity, suggesting that active species are formed both on tetrahedral and amorphous non-framework Ti. Propylene interaction at 60°C gives rise to new Raman bands at 517, 805, 840, 917, and 983 cm^{-1}, ascribable to the 1,2-propanediol, one of the by-products in the reaction. This assignment is confirmed by the presence of its typical C-H stretching mode around

3,000 cm^{-1} (not discussed for sake of brevity). In this case, the 1,125 cm^{-1} Ti fingerprint seems to be restored after product formation. Guo et al. [197] support their conclusion also with catalytic data, which showed that TS-1A and TS-1B samples have a similar H_2O_2 conversion, but the latter exhibits a lower selectivity toward propylene oxide.

Concerning X-ray spectroscopies, few studies dealt with non-perfect TS-1 materials. Among these, a relevant example is represented by the work by Zuo et al., exploiting the Ti L-edges transition rather than the more conventional K-edge [199]. Considering all the possible L transitions, of particular interest are the so-called L_2 and L_3 edges, generating from the $2p \rightarrow 3d$ transitions from the $2p_{1/2}$ and $2p_{3/2}$, respectively. Each of them is further split in several components, according to the separation of the *d* levels as a consequence of the crystal fields experienced by Ti. Thus, it is clear that this technique has a very high structural sensitivity [200]. The main drawback is due to the energy range where these transitions falls, roughly among 450 and 480 eV (i.e., in the soft X-rays). This implies that experiments should be carried out under ultrahigh vacuum (UHV), imposing constrains which hampers the possibility to run measurements in conditions relevant for catalysis (e.g., in the presence of reactants). Very few studies are available concerning TS-1 and Ti-based materials, but recently Zuo et al. successfully exploited this technique to confirm the presence of a new type of pentahedral Ti site in their TS-1 samples, which they correlated to their higher catalytic activity in propene epoxidation [199]. Recent developments in the soft X-ray experimental tools are progressively opening the application of these measurements at ambient conditions [127], thus making them more accessible and useful to the catalysis community in the near future.

5 Conclusions

The main aim of this chapter was to show the goodness and the potential of combining different advanced characterization techniques in elucidating the metal active sites in metal-zeolites, as well as how the rational design of in situ/operando experiments can provide new catalytic insights. Notwithstanding decades of research efforts, the results described and discussed in this contribution show how the field of metal-exchanged zeolites is still intriguing and open to further findings. This is particularly true in relation to their activity in selective oxidation reactions and the renewed interest in developing closed catalytic cycles for the MTM "dream reaction." Three different kinds of zeolites were considered, with a focus on the geometric and electronic structure of the redox-active TMIs stabilized in the zeolite framework, on the related characterization potentiality and limits, and on the open characterization challenges.

Namely, TS-1 can be considered as an example of "single-site" catalyst, since – when well manufactured – all Ti^{IV} atoms are found in framework positions in a tetrahedral environment. This allowed to precisely define the characteristic spectroscopic fingerprints, to carry out in-depth studies about interaction with ligands of framework Ti^{IV} and its reactivity toward aqueous solution of H_2O_2. However, the reported survey shows how often a multi-technique approach is important to obtain reliable and significant information about the active site properties. Moreover, the study of the reactivity in aqueous medium with H_2O_2 represented a challenge for the involved researchers, who needed to optimize characterization setups and protocols to discriminate between the effect on the spectroscopic features of the H_2O (ligand) and the H_2O_2 (reactant) and their synergic role. Further degrees of complexity derive from the necessity to carry out the experiments on samples activated under controlled atmosphere (vacuum) and from the lability of the active Ti-peroxo/Ti-hydroperoxo complexes. rR still represents one of the main techniques to study these materials, particularly coupled to optimized setups to carry out in situ experiments, with particular care to avoid spectral modifications due to laser irradiation. In this case, averaged techniques such as DR UV-Vis and XAS/XES showed their potentiality in monitoring changes in the "single-site" Ti^{IV} local environment, even if the lability of the Ti-peroxo/Ti-hydroperoxo complexes suggests caution when working with X-rays, especially from an undulator source, in relation to the possibility of beam damage.

In principle, Cu-exchanged zeolites could be considered as model systems, since the Cu^{I}/Cu^{II} ions are stabilized as counterions and many structural information can be found in the literature about their location in the zeolite channels and cavities, also in relation to Al_{fw} content and distribution. However, the lively debate reviewed in this chapter in relation to the activity in the MTM reaction shows how this system is far from being a "single-site" catalyst. DR UV-Vis spectroscopy was particularly relevant in the study of Cu-ZSM-5 (and Cu-MOR), in relation to the peculiar band around 22,700 cm^{-1}, decreasing its intensity when contacted with methane. However, also in this case, more detailed insights into the structure of the Cu-oxo sites responsible for these spectroscopic fingerprints (and likely involved in methane oxidation) could be obtained only by coupling different techniques, such as rR and NCA or DFT calculations. Moreover, there is still a lot of interest in giving a precise assignment of the spectral features of other Cu-zeolites, such as small-pore Cu-CHA (characterized by a very peculiar and intense "quadruplet" in the *d-d* region), particularly by using operando techniques allowing to work under flow and at high temperatures. This is crucial in relation to the stability and possible interplays among different Cu-oxo species.

An important contribution in the field of Cu-zeolites was given by XAS experiments, concerning the "starting point" (pre-activated catalyst), the formation of active Cu-oxo species, their interaction with methane, and subsequent steam-mediated methanol desorption. Also in this respect, it is important to underline the importance of DFT calculations, which should guide data fitting in order to give reliable and consistent information on the local structure of the involved metal centers. Moreover, being an averaged technique applied to materials to which the concept of "single site" is questioned by many authors, XAS analysis output (especially XANES) should be considered with great care.

The third class of catalysts considered in this contribution, Fe-zeolites, represents a further increase in complexity, due to the difficulties in obtaining materials with a homogenous site distribution. In addition to the difficulties discussed for Cu-zeolites, in this case grafted Fe ions were proposed, together with a variety of di-, tri-, and olinuclear oxo/hydroxo clusters dispersed inside the zeolites channels and large iron oxide aggregates formed on the zeolite particles' external surface. This implies that the main averaged techniques discussed above, i.e., XAS and DR-UV-Vis, have intrinsic limitations, notwithstanding the reported efforts of rationalization of UV-Vis deconvoluted sub-bands. rR still represents one of the most powerful techniques for the characterization of oxo species (as in the case of TS-1 and Cu-zeolites), but the optimization of setups and protocols to study partial oxidation reactions is challenging, so that there is still room for new findings. Moreover, very recent developments about Fe-zeolites for the MTM reaction involved the optimization of exchange procedures (or thermal treatments), aimed to improve Fe insertion and ideally obtain "single-site" catalysts with Fe^{II} stabilized as counterion. Clearly, these approaches could open the way to further spectroscopic insights into the nature of active sites in partial oxidation reactions.

As a final remark, it is important to recall the recently proposed concepts about self-organization of extraframework cations in zeolites and about the role of ion mobility during catalysis [51, 149]. These notions could help in the interpretation of many apparently contradictory results reported in literature. Even if adding up to the complexity of the spectroscopic challenge, they testify about a scientific field still active and intriguing, particularly in relation to the possibility to follow the catalyst in operando conditions with a multi-technique approach.

References

1. Sankar G, Raja R, Thomas JM (1998) Redox solid catalysts for the selective oxidation of cyclohexane in air. Catal Lett 55:15–23
2. Thomas JM (2001) On the nature of isolated active sites in open-structure catalysts for the aerial oxidation of alkanes. Top Catal 15:85–91
3. Raja R, Thomas JM, Greenhill-Hooper M et al (2007) A high-performance selective oxidation system for the facile production of fine chemicals. Chem Commun:1924–1926
4. Raja R, Thomas JM, Xu MC et al (2006) Highly efficient one-step conversion of cyclohexane to adipic acid using single-site heterogeneous catalysts. Chem Commun:448–450
5. Maurelli S, Vishnuvarthan M, Berlier G et al (2012) NH_3 and O_2 interaction with tetrahedral Ti^{3+} ions isomorphously substituted in the framework of TiAlPO-5. A combined pulse EPR, pulse ENDOR, UV-Vis and FT-IR study. Phys Chem Chem Phys 14:987–995
6. Maurelli S, Vishnuvarthan M, Chiesa M et al (2011) Elucidating the nature and reactivity of Ti ions incorporated in the framework of AlPO-5 molecular sieves. New evidence from ^{31}P HYSCORE spectroscopy. J Am Chem Soc 133:7340–7343
7. Morra E, Cuko A, Maurelli S et al (2015) Electronic structure of Ti^{3+}-ethylene complexes in microporous aluminophosphate materials. A combined EPR and DFT study elucidating the role of SOMO orbitals in metal-olefin π·complexes. J Phys Chem C 119:26046–26055

8. Novara C, Alfayate A, Berlier G et al (2013) The interaction of H_2O_2 with TiAlPO-5 molecular sieves: probing the catalytic potential of framework substituted Ti ions. Phys Chem Chem Phys 15:11099–11105
9. Berlier G, Spoto G, Bordiga S et al (2002) Evolution of extraframework iron species in Fe silicalite 1. Effect of Fe content, activation temperature, and interaction with redox agents. J Catal 208:64–82
10. Zecchina A, Rivallan M, Berlier G et al (2007) Structure and nuclearity of active sites in Fe-zeolites: comparison with iron sites in enzymes and homogeneous catalysts. Phys Chem Chem Phys 9:3483–3499
11. Beale AM, van der Eerden AMJ, Kervinen K et al (2005) Adding a third dimension to operando spectroscopy: a combined UV-Vis, Raman and XAFS setup to study heterogeneous catalysts under working conditions. Chem Commun:3015–3017
12. Jentoft FC (2009) Ultraviolet-visible-near infrared spectroscopy in catalysis: theory, experiment, analysis, and application under reaction conditions. Adv Catal 52:129–211
13. Tinnemans SJ, Kox MHF, Sletering MW et al (2006) Dealing with a local heating effect when measuring catalytic solids in a reactor with Raman spectroscopy. Phys Chem Chem Phys 8:2413–2420
14. Tinnemans SJ, Mesu JG, Kervinen K et al (2006) Combining operando techniques in one spectroscopic-reaction cell: new opportunities for elucidating the active site and related reaction mechanism in catalysis. Catal Today 113:3–15
15. Beato P, Schachtl E, Barbera K et al (2013) Operando Raman spectroscopy applying novel fluidized bed micro-reactor technology. Catal Today 205:128–133
16. Rasmussen SB, Lopez-Medina R, Portela R et al (2015) Shaping up operando spectroscopy: Raman characterization of a working honeycomb monolith. Cat Sci Technol 5:4942–4945
17. Bordiga S, Lamberti C, Bonino F et al (2015) Probing zeolites by vibrational spectroscopies. Chem Soc Rev 44:7262–7341
18. Bordiga S, Groppo E, Agostini G et al (2013) Reactivity of surface species in heterogeneous catalysts probed by *in situ* X-ray absorption techniques. Chem Rev 113:1736–1850
19. Lamberti C, Groppo E, Spoto G et al (2007) Infrared spectroscopy of transient surface species. Adv Catal 51:1–74
20. Lamberti C, Zecchina A, Groppo E et al (2010) Probing the surfaces of heterogeneous catalysts by *in situ* IR spectroscopy. Chem Soc Rev 39:4951–5001
21. Tang P, Zhu Q, Wu Z et al (2014) Methane activation: the past and future. Energ Environ Sci 7:2580–2591
22. Park D, Lee J (2013) Biological conversion of methane to methanol. Korean J Chem Eng 30:977–987
23. Schwarz H (2011) Chemistry with methane: concepts rather than recipes. Angew Chem Int Ed 50:10096–10115
24. Smeets PJ, Groothaert MH, van Teeffelen RM et al (2007) Direct and NO-assisted N_2O decomposition over Cu-zeolites. In: Xu R, Gao Z, Chen J, Yan W (eds) From zeolites to porous MOF materials: the 40th Anniversary of International Zeolite Conference, Proceedings of the 15th International Zeolite Conference, pp 1080–1087
25. Olah GA, Prakash GKS, Goeppert A (2011) Anthropogenic chemical carbon cycle for a sustainable future. J Am Chem Soc 133:12881–12898
26. Groothaert MH, Smeets PJ, Sels BF et al (2005) Selective oxidation of methane by the bis(mu-oxo)dicopper core stabilized on ZSM-5 and mordenite zeolites. J Am Chem Soc 127:1394–1395
27. Panov GI, Sobolev VI, Kharitonov AS (1990) The role of iron in N_2O decomposition on ZSM-5 zeolite and reactivity of the surface oxygen formed. J Mol Catal 61:85–97
28. Dubkov KA, Sobolev VI, Panov GI (1998) Low-temperature oxidation of methane to methanol on FeZSM-5 zeolite. Kinet Catal 39:72–79
29. Sobolev VI, Dubkov KA, Panna OV et al (1995) Selective oxidation of methane to methanol on a FeZSM-5 surface. Catal Today 24:251–252

30. Kharitonov AS, Sheveleva GA, Panov GI et al (1993) Ferrisilicate analogs of ZSM-5 zeolite as catalysts for one-step oxidation of benzene to phenol. Appl Catal A Gen 98:33–43
31. Panov GI, Kharitonov AS, Sobolev VI (1993) Oxidative hydroxylation using dinitrogen monoxide – a possible route for organic-synthesis over zeolites. Appl Catal A Gen 98:1–20
32. Hammond C, Forde MM, Ab Rahim MH et al (2012) Direct catalytic conversion of methane to methanol in an aqueous medium by using copper-promoted Fe-ZSM-5. Angew Chem Int Ed 51:5129–5133
33. Beznis NV, van Laak ANC, Weckhuysen BM et al (2011) Oxidation of methane to methanol and formaldehyde over Co-ZSM-5 molecular sieves: tuning the reactivity and selectivity by alkaline and acid treatments of the zeolite ZSM-5 agglomerates. Microporous Mesoporous Mater 138:176–183
34. Kung MC, Lin SSY, Kung HH (2012) In situ infrared spectroscopic study of CH_4 oxidation over Co-ZSM-5. Top Catal 55:108–115
35. Shan JJ, Huang WX, Nguyen L et al (2014) Conversion of methane to methanol with a bent mono(μ-oxo)dinickel anchored on the internal surfaces of micropores. Langmuir 30:8558–8569
36. Beznis NV, Weckhuysen BM, Bitter JH (2010) Cu-ZSM-5 zeolites for the formation of methanol from methane and oxygen: probing the active sites and spectator species. Catal Lett 138:14–22
37. Giordanino F, Vennestrom PNR, Lundegaard LF et al (2013) Characterization of Cu-exchanged SSZ-13: a comparative FTIR, UV-Vis, and EPR study with Cu-ZSM-5 and Cu-β with similar Si/Al and Cu/Al ratios. Dalton Trans 42:12741–12761
38. Vanelderen P, Hadt RG, Smeets PJ et al (2011) Cu-ZSM-5: a biomimetic inorganic model for methane oxidation. J Catal 284:157–164
39. Tsai M-L, Hadt RG, Vanelderen P et al (2014) $[Cu_2O]^{2+}$ active site formation in Cu-ZSM-5: geometric and electronic structure requirements for N_2O activation. J Am Chem Soc 136:3522–3529
40. Groothaert MH, van Bokhoven JA, Battiston AA et al (2003) Bis(μ-oxo)dicopper in Cu-ZSM-5 and its role in the decomposition of NO: a combined in situ XAFS, UV-Vis-near-IR, and kinetic study. J Am Chem Soc 125:7629–7640
41. Halfen JA, Mahapatra S, Wilkinson EC et al (1996) Reversible cleavage and formation of the dioxygen O-O band within a dicopper complex. Science 271:1397–1400
42. Que L, Tolman WB (2002) Bis(μ-oxo)dimetal "diamond" cores in copper and iron complexes relevant to biocatalysis. Angew Chem Int Ed 41:1114–1137
43. Solomon EI, Sundaram UM, Machonkin TE (1996) Multicopper oxidases and oxygenases. Chem Rev 96:2563–2605
44. Holland PL, Tolman WB (1999) Dioxygen activation by copper sites: relative stability and reactivity of $(\mu\text{-}\eta^2\text{:}\eta^2)$-peroxo)- and bis(μ-oxo)dicopper cores. Coord Chem Rev 190:855–869
45. Woertink JS, Smeets PJ, Groothaert MH et al (2009) A $[Cu_2O]^{2+}$ core in Cu-ZSM-5, the active site in the oxidation of methane to methanol. Proc Natl Acad Sci U S A 106:18908–18913
46. Smeets PJ, Hadt RG, Woertink JS et al (2010) Oxygen precursor to the reactive intermediate in methanol synthesis by Cu-ZSM-5. J Am Chem Soc 132:14736–14738
47. Smeets PJ, Groothaert MH, Schoonheydt RA (2005) Cu based zeolites: a UV-Vis study of the active site in the selective methane oxidation at low temperatures. Catal Today 110:303–309
48. Smeets PJ, Woertink JS, Sels BF et al (2010) Transition-metal ions in zeolites: coordination and activation of oxygen. Inorg Chem 49:3573–3583
49. Vanelderen P, Vancauwenbergh J, Sels BF et al (2013) Coordination chemistry and reactivity of copper in zeolites. Coord Chem Rev 257:483–494
50. Paolucci C, Parekh AA, Khurana I et al (2016) Catalysis in a cage: condition-dependent speciation and dynamics of exchanged Cu cations in SSZ-13 zeolites. J Am Chem Soc 138:6028–6048
51. Paolucci C, Khurana I, Parekh AA et al (2017) Dynamic multinuclear sites formed by mobilized copper ions in NO_x selective catalytic reduction. Science 357:898–903

52. Sheppard T, Daly H, Goguet A et al (2016) Improved efficiency for partial oxidation of methane by controlled copper deposition on surface-modified ZSM-5. ChemCatChem 8:562–570
53. Narsimhan K, Iyoki K, Dinh K et al (2016) Catalytic oxidation of methane into methanol over copper-exchanged zeolites with oxygen at low temperature. ACS Central Sci 2:424–429
54. Grundner S, Luo W, Sanchez-Sanchez M et al (2016) Synthesis of single-site copper catalysts for methane partial oxidation. Chem Commun 52:2553–2556
55. Grundner S, Markovits MAC, Li G et al (2015) Single-site trinuclear copper oxygen clusters in mordenite for selective conversion of methane to methanol. Nat Commun 6:2553–2556
56. Ipek B, Wulfers MJ, Kim H et al (2017) Formation of $[Cu_2O_2]^{2+}$ and $[Cu_2O]^{2+}$ toward C-H bond activation in Cu-SSZ-13 and Cu-SSZ-39. ACS Catal 7:4291–4303
57. Pappas DK, Borfecchia E, Dyballa M et al (2017) Methane to methanol: structure–activity relationships for Cu-CHA. J Am Chem Soc 139:14961–14975
58. Vanelderen P, Vancauwenbergh J, Tsai ML et al (2014) Spectroscopy and redox chemistry of copper in mordenite. ChemPhysChem 15:91–99
59. Alayon EMC, Nachtegaal M, Kleymenov E et al (2013) Determination of the electronic and geometric structure of Cu sites during methane conversion over Cu-MOR with X-ray absorption spectroscopy. Microporous Mesoporous Mater 166:131–136
60. Vanelderen P, Snyder BER, Tsai M-L et al (2015) Spectroscopic definition of the copper active sites in mordenite: selective methane oxidation. J Am Chem Soc 137:6383−6392
61. Mentzen BF, Bergeret G (2007) Crystallographic determination of the positions of the copper cations in zeolite MFI. J Phys Chem C 111:12512–12516
62. Alayon EM, Nachtegaal M, Ranocchiari M et al (2012) Catalytic conversion of methane to methanol over Cu-mordenite. Chem Commun 48:404–406
63. Alayon EMC, Nachtegaal M, Bodi A et al (2014) Reaction conditions of methane-to-methanol conversion affect the structure of active copper sites. ACS Catal 4:16–22
64. Alayon EMC, Nachtegaal M, Bodi A et al (2015) Bis(μ-oxo) versus mono(μ-oxo)dicopper cores in a zeolite for converting methane to methanol: an *in situ* XAS and DFT investigation. Phys Chem Chem Phys 17:7681–7693
65. Tomkins P, Mansouri A, Bozbag SE et al (2016) Isothermal cyclic conversion of methane into methanol over copper-exchanged zeolite at low temperature. Angew Chem Int Ed 55:5467–5471
66. Sushkevich VL, Palagin D, Ranocchiari M et al (2017) Selective anaerobic oxidation of methane enables direct synthesis of methanol. Science 356:523–527
67. Borfecchia E, Lomachenko KA, Giordanino F et al (2015) Revisiting the nature of Cu sites in the activated Cu-SSZ-13 catalyst for SCR reaction. Chem Sci 6:548–563
68. Li GN, Vassilev P, Sanchez-Sanchez M et al (2016) Stability and reactivity of copper oxo-clusters in ZSM-5 zeolite for selective methane oxidation to methanol. J Catal 338:305–312
69. Markovits MAC, Jentys A, Tromp M et al (2016) Effect of location and distribution of Al sites in ZSM-5 on the formation of Cu-oxo clusters active for direct conversion of methane to methanol. Top Catal 59:1554–1563
70. Palagin D, Knorpp AJ, Pinar AB et al (2017) Assessing the relative stability of copper oxide clusters as active sites of a CuMOR zeolite for methane to methanol conversion: size matters? Nanoscale 9:1144–1153
71. Vilella L, Studt F (2016) The stability of copper oxo species in zeolite frameworks. Eur J Inorg Chem 2016:1514–1520
72. Wulfers MJ, Teketel S, Ipek B et al (2015) Conversion of methane to methanol on copper-containing small-pore zeolites and zeotypes. Chem Commun 51:4447–4450
73. Janssens TVW, Falsig H, Lundegaard LF et al (2015) A consistent reaction scheme for the selective catalytic reduction of nitrogen oxides with ammonia. ACS Catal 5:2832–2845

74. Andersen CW, Borfecchia E, Bremholm M et al (2017) Redox-driven migration of copper ions in the Cu-CHA zeolite as shown by the in situ PXRD/XANES technique. Angew Chem Int Ed 56:10367–10372
75. Lomachenko KA, Borfecchia E, Negri C et al (2016) The Cu-CHA deNO(x) catalyst in action: temperature-dependent NH_3-assisted selective catalytic reduction monitored by operando XAS and XES. J Am Chem Soc 138:12025–12028
76. Martini A, Borfecchia E, Lomachenko KA et al (2017) Composition-driven Cu-speciation and reducibility in Cu-CHA zeolite catalysts: a multivariate XAS/FTIR approach to complexity. Chem Sci 8:6836–6851
77. Beale AM, Gao F, Lezcano-Gonzalez I et al (2015) Recent advances in automotive catalysis for NO_x emission control by small-pore microporous materials. Chem Soc Rev 44:7371–7405
78. Deka U, Juhin A, Eilertsen EA et al (2012) Confirmation of isolated Cu^{2+} ions in SSZ-13 zeolite as active sites in NH_3-selective catalytic reduction. J Phys Chem C 116:4809–4818
79. Ipek B, Lobo RF (2016) Catalytic conversion of methane to methanol on Cu-SSZ-13 using N_2O as oxidant. Chem Commun 52:13401–13404
80. Kulkarni AR, Zhao ZJ, Siahrostami S et al (2016) Monocopper active site for partial methane oxidation in Cu-exchanged 8MR zeolites. ACS Catal 6:6531–6536
81. Perez-Ramirez J, Groen JC, Bruckner A et al (2005) Evolution of isomorphously substituted iron zeolites during activation: comparison of Fe-beta and Fe-ZSM-5. J Catal 232:318–334
82. Capek L, Kreibich V, Dedecek J et al (2005) Analysis of Fe species in zeolites by UV-VIS-NIR, IR spectra and voltammetry. Effect of preparation, Fe loading and zeolite type. Microporous Mesoporous Mater 80:279–289
83. Jisa K, Novakova J, Schwarze M et al (2009) Role of the Fe-zeolite structure and iron state in the N_2O decomposition: comparison of Fe-FER, Fe-BEA, and Fe-MFI catalysts. J Catal 262:27–34
84. Sklenak S, Andrikopoulos PC, Boekfa B et al (2010) N_2O decomposition over Fe-zeolites: structure of the active sites and the origin of the distinct reactivity of Fe-ferrierite, Fe-ZSM-5, and Fe-beta. A combined periodic DFT and multispectral study. J Catal 272:262–274
85. Sobalik Z, Tabor E, Novakova J et al (2012) Role of active oxygen and NO_x species in N_2O decomposition over Fe-ferrierite. J Catal 289:164–170
86. Pieterse JAZ, Pirngruber GD, van Bokhoven JA et al (2007) Hydrothermal stability of Fe-ZSM-5 and Fe-BEA prepared by wet ion-exchange for N_2O decomposition. Appl Catal B Environ 71:16–22
87. Yuranov I, Bulushev DA, Renken A et al (2004) Benzene hydroxylation over FeZSM-5 catalysts: which Fe sites are active? J Catal 227:138–147
88. Snyder BER, Vanelderen P, Bols ML et al (2016) The active site of low-temperature methane hydroxylation in iron-containing zeolites. Nature 536:317–323
89. Perez-Ramirez J, Kapteijn F, Mul G et al (2001) Superior performance of ex-framework FeZSM-5 in direct N_2O decomposition in tail-gases from nitric acid plants. Chem Commun:693–694
90. Perez-Ramirez J, Kapteijn F, Schoffel K et al (2003) Formation and control of N_2O in nitric acid production – where do we stand today? Appl Catal B Environ 44:117–151
91. Panov GI, Uriarte AK, Rodkin MA et al (1998) Generation of active oxygen species on solid surfaces. Opportunity for novel oxidation technologies over zeolites. Catal Today 41:365–385
92. Marturano P, Drozdova L, Kogelbauer A et al (2000) Fe/ZSM-5 prepared by sublimation of $FeCl_3$: the structure of the Fe species as determined by IR, Al-27 MAS NMR, and EXAFS spectroscopy. J Catal 192:236–247
93. Marturano P, Drozdova L, Pirngruber GD et al (2001) The mechanism of formation of the Fe species in Fe/ZSM-5 prepared by CVD. Phys Chem Chem Phys 3:5585–5595
94. Battiston AA, Bitter JH, de Groot FMF et al (2003) Evolution of Fe species during the synthesis of over-exchanged Fe/ZSM5 obtained by chemical vapor deposition of $FeCl_3$. J Catal 213:251–271

95. Feng XB, Hall WK (1997) FeZSM-5: a durable SCR catalyst for NO_x removal from combustion streams. J Catal 166:368–376
96. Marturano P, Kogelbauer A, Prins R (2000) Preparation of overexchanged Fe-ZSM-5 zeolites using the ferrous oxalate method: why does it fail? J Catal 190:460–468
97. Nechita MT, Berlier G, Ricchiardi G et al (2005) New precursor for the post-synthesis preparation of Fe-ZSM-5 zeolites with low iron content. Catal Lett 103:33–41
98. Bordiga S, Buzzoni R, Geobaldo F et al (1996) Structure and reactivity of framework and extraframework iron in Fe-silicalite as investigated by spectroscopic and physicochemical methods. J Catal 158:486–501
99. Perez-Ramirez J, Kapteijn F, Mul G et al (2002) Direct N_2O decomposition over ex-framework FeMFI catalysts. Role of extra-framework species. Catal Commun 3:19–23
100. Pirngruber GD, Roy PK, Prins R (2006) On determining the nuclearity of iron sites in Fe-ZSM-5 – a critical evaluation. Phys Chem Chem Phys 8:3939–3950
101. Shu LJ, Liu Y, Lipscomb JD et al (1996) X-ray absorption spectroscopic studies of the methane monooxygenase hydroxylase component from Methylosinus trichosporium OB3b. J Biol Inorg Chem 1:297–304
102. Shu LJ, Nesheim JC, Kauffmann K et al (1997) An (Fe_2O_2)-O-IV diamond core structure for the key intermediate Q of methane monooxygenase. Science 275:515–518
103. Taboada JB, Overweg AR, Kooyman PJ et al (2005) Following the evolution of iron from framework to extra-framework positions in isomorphously substituted Fe, Al MFI with ^{57}Fe Mossbauer spectroscopy. J Catal 231:56–66
104. Fejes P, Lazar K, Marsi I et al (2003) Isomorphously substituted Fe-ZSM-5 zeolites as catalysts causes of catalyst ageing as revealed by X-band EPR, Mossbauer and ^{29}Si MAS NMR spectra. Appl Catal A Gen 252:75–90
105. Dubkov KA, Ovanesyan NS, Shteinman AA et al (2002) Evolution of iron states and formation of alpha-sites upon activation of FeZSM-5 zeolites. J Catal 207:341–352
106. Kondratenko EV, Kondratenko VA, Santiago M et al (2008) Mechanistic origin of the different activity of Rh-ZSM-5 and Fe-ZSM-5 in N_2O decomposition. J Catal 256:248–258
107. Kondratenko EV, Perez-Ramirez J (2006) Mechanism and kinetics of direct N_2O decomposition over Fe-MFI zeolites with different iron speciation from temporal analysis of products. J Phys Chem B 110:22586–22595
108. Kondratenko EV, Perez-Ramirez J (2007) Micro-kinetic analysis of direct N_2O decomposition over steam-activated Fe-silicalite from transient experiments in the TAP reactor. Catal Today 121:197–203
109. Kondratenko EV, Perez-Ramirez J (2007) Mechanistic peculiarities of the N_2O reduction by CH_4 over Fe-silicalite. Catal Today 119:243–246
110. Ribera A, Arends I, de Vries S et al (2000) Preparation, characterization, and performance of FeZSM-5 for the selective oxidation of benzene to phenol with N_2O. J Catal 195:287–297
111. Kumar MS, Schwidder M, Grunert W et al (2004) On the nature of different iron sites and their catalytic role in Fe-ZSM-5 $DeNO_x$ catalysts: new insights by a combined EPR and UV/VIS spectroscopic approach. J Catal 227:384–397
112. Hensen EJM, Zhu Q, Janssen RAJ et al (2005) Selective oxidation of benzene to phenol with nitrous oxide over MFI zeolites. 1. On the role of iron and aluminum. J Catal 233:123–135
113. Pirngruber GD, Luechinger M, Roy PK et al (2004) N_2O decomposition over iron-containing zeolites prepared by different methods: a comparison of the reaction mechanism. J Catal 224:429–440
114. Jia JF, Sun Q, Wen B et al (2002) Identification of highly active iron sites in N_2O-activated Fe/MFI. Catal Lett 82:7–11
115. Wood BR, Reimer JA, Bell AT et al (2004) Nitrous oxide decomposition and surface oxygen formation on Fe-ZSM-5. J Catal 224:148–155
116. Wood BR, Reimer JA, Bell AG (2002) Studies of N_2O adsorption and decomposition on Fe-ZSM-5. J Catal 209:151–158

117. El-Malki EM, van Santen RA, Sachtler WMH (2000) Active sites in Fe/MFI catalysts for NO_x reduction and oscillating N_2O decomposition. J Catal 196:212–223
118. Mul G, Perez-Ramirez J, Kapteijn F et al (2002) NO adsorption on ex-framework Fe, X MFI catalysts: novel IR bands and evaluation of assignments. Catal Lett 80:129–138
119. Bulushev DA, Renken A, Kiwi-Minsker L (2006) Formation of the surface NO during N_2O interaction at low temperature with iron-containing ZSM-5. J Phys Chem B 110:305–312
120. Berlier G, Lamberti C, Rivallan M et al (2010) Characterization of Fe sites in Fe-zeolites by FTIR spectroscopy of adsorbed NO: are the spectra obtained in static vacuum and dynamic flow set-ups comparable? Phys Chem Chem Phys 12:358–364
121. Roy PK, Prins R, Pirngruber GD (2008) The effect of pretreatment on the reactivity of Fe-ZSM-5 catalysts for N_2O decomposition: dehydroxylation vs. steaming. Appl Catal B Environ 80:226–236
122. Pirngruber GD, Pieterse JAZ (2006) The positive effect of NO on the N_2O decomposition activity of Fe-ZSM-5: a combined kinetic and in situ IR spectroscopic study. J Catal 237:237–247
123. Wood BR, Reimer JA, Bell AT et al (2004) Methanol formation on Fe/Al-MFI via the oxidation of methane by nitrous oxide. J Catal 225:300–306
124. Li C (2003) Identifying the isolated transition metal ions/oxides in molecular sieves and on oxide supports by UV resonance Raman spectroscopy. J Catal 216:203–212
125. Bonino F, Damin A, Piovano A et al (2011) Direct evidence of highly dispersed iron in Fe-silicalite: a Raman spectroscopic study. ChemCatChem 3:139–142
126. Wang JY, Li GN, Ju XH et al (2013) Identification of $Fe_2(\mu\text{-}O)$ and $Fe_2(\mu\text{-}O)_2$ sites in Fe/ZSM-35 by *in situ* resonance Raman spectroscopy. J Catal 301:77–82
127. Knop-Gericke A, Hävecker M, Schedel-Niedrig T et al (2000) High-pressure low-energy XAS: a new tool for probing reacting surfaces of heterogeneous catalysts. Top Catal 10:187–198
128. Perez-Ramirez J, Mul G, Kapteijn F et al (2002) Physicochemical characterization of isomorphously substituted FeZSM-5 during activation. J Catal 207:113–126
129. Pirngruber GD, Grunwaldt JD, Roy PK et al (2007) The nature of the active site in the Fe-ZSM-5/N_2O system studied by (resonant) inelastic X-ray scattering. Catal Today 126:127–134
130. Andrikopoulos PC, Sobalik Z, Novakova J et al (2013) Mechanism of framework oxygen exchange in Fe-zeolites: a combined DFT and mass spectrometry study. ChemPhysChem 14:520–531
131. Hansen N, Heyden A, Bell AT et al (2007) Microkinetic modeling of nitrous oxide decomposition on dinuclear oxygen bridged iron sites in Fe-ZSM-5. J Catal 248:213–225
132. Hansen N, Heyden A, Bell AT et al (2007) A reaction mechanism for the nitrous oxide decomposition on binuclear oxygen bridged iron sites in Fe-ZSM-5. J Phys Chem C 111:2092–2101
133. Heyden A, Hansen N, Bell AT et al (2006) Nitrous oxide decomposition over Fe-ZSM-5 in the presence of nitric oxide: a comprehensive DFT study. J Phys Chem B 110:17096–17114
134. Heyden A, Peters B, Bell AT et al (2005) Comprehensive DFT study of nitrous oxide decomposition over Fe-ZSM-5. J Phys Chem B 109:1857–1873
135. Kiwi-Minsker L, Bulushev DA, Renken A (2003) Active sites in HZSM-5 with low Fe content for the formation of surface oxygen by decomposing N_2O: is every deposited oxygen active? J Catal 219:273–285
136. Perez-Ramirez J, Kumar MS, Bruckner A (2004) Reduction of N_2O with CO over FeMFI zeolites: influence of the preparation method on the iron species and catalytic behavior. J Catal 223:13–27
137. Berlier G, Spoto G, Ricchiardi G et al (2002) IR spectroscopy of adsorbed NO as a useful tool for the characterisation of low concentrated Fe-silicalite catalysts. J Mol Catal A Chem 182:359–366

138. Berlier G, Zecchina A, Spoto G et al (2003) The role of Al in the structure and reactivity of iron centers in Fe-ZSM-5-based catalysts: a statistically based infrared study. J Catal 215:264–270
139. Rivallan M, Berlier G, Ricchiardi G et al (2008) Characterisation and catalytic activity in de-NO_x reactions of Fe-ZSM-5 zeolites prepared via ferric oxalate precursor. Appl Catal B Environ 84:204–213
140. Mul G, Zandbergen MW, Kapteijn F et al (2004) N_2O decomposition over liquid ion-exchanged Fe-BEA catalysts: correlation between activity and the IR intensity of adsorbed NO at 1874 cm^{-1}. Catal Lett 93:113–120
141. Spoto G, Zecchina A, Berlier G et al (2000) FTIR and UV-Vis characterization of Fe-silicalite. J Mol Catal A Chem 158:107–114
142. Berlier G, Bonino F, Zecchina A et al (2003) Anchoring Fe ions to amorphous and crystalline oxides: a means to tune the degree of Fe coordination. ChemPhysChem 4:1073–1078
143. Hammond C, Dimitratos N, Jenkins RL et al (2013) Elucidation and evolution of the active component within Cu/Fe/ZSM-5 for catalytic methane oxidation: from synthesis to catalysis. ACS Catal 3:689–699
144. Forde MM, Armstrong RD, McVicker R et al (2014) Light alkane oxidation using catalysts prepared by chemical vapour impregnation: tuning alcohol selectivity through catalyst pre-treatment. Chem Sci 5:3603–3616
145. Hammond C, Dimitratos N, Lopez-Sanchez JA et al (2013) Aqueous-phase methane oxidation over Fe-MFI zeolites; promotion through isomorphous framework substitution. ACS Catal 3:1835–1844
146. Hammond C, Hermans I, Dimitratos N (2015) Biomimetic oxidation with Fe-ZSM-5 and H_2O_2? Identification of an active, extra-framework binuclear core and an Fe^{III}-OOH intermediate with resonance-enhanced Raman spectroscopy. ChemCatChem 7:434–440
147. Sun KJ, Fan FT, Xia HA et al (2008) Framework Fe ions in Fe-ZSM-5 zeolite studied by UV resonance Raman spectroscopy and density functional theory calculations. J Phys Chem C 112:16036–16041
148. Pidko EA, Degirmenci V, van Santen RA et al (2010) Glucose activation by transient Cr^{2+} dimers. Angew Chem Int Ed 49:2530–2534
149. Pidko EA, Hensen EJM, van Santen RA (2012) Self-organization of extraframework cations in zeolites. Proc R Soc London Ser A Math Phys Eng Sci 468:2070–2086
150. Taramasso M, Perego G, Notari B (1983) Preparation of porous crystalline synthetic material comprised of silicon and titanium oxides. US Patent 4410501A, 18 Oct 1983
151. Lamberti C, Bordiga S, Zecchina A et al (1999) Structural characterization of Ti-silicalite-1: a synchrotron radiation X-ray powder diffraction study. J Catal 183:222–231
152. Millini R, Massara EP, Perego G et al (1992) Framework composition of titanium silicalite-1. J Catal 137:497–503
153. Millini R, Perego G, Berti D et al (2000) Structural characterization of as-synthesized B- and Ti-containing MFI-type molecular sieves. Microporous Mesoporous Mater 35-6:387–403
154. Hijar CA, Jacubinas RM, Eckert J et al (2000) The siting of Ti in TS-1 is non-random. Powder neutron diffraction studies and theoretical calculations of TS-1 and FeS-1. J Phys Chem B 104:12157–12164
155. Lamberti C, Bordiga S, Zecchina A et al (2001) Ti location in the MFI framework of Ti-silicalite-1: a neutron powder diffraction study. J Am Chem Soc 123:2204–2212
156. Scarano D, Zecchina A, Bordiga S et al (1993) Fourier-transform infrared and Raman-spectra of pure and Al-substituted, B-substituted, Ti-substituted and Fe-substituted silicalites – stretching-mode region. J Chem Soc Faraday Trans 89:4123–4130
157. Ricchiardi G, Damin A, Bordiga S et al (2001) Vibrational structure of titanium silicate catalysts. A spectroscopic and theoretical study. J Am Chem Soc 123:11409–11419
158. Bordiga S, Damin A, Bonino F et al (2002) Effect of interaction with H_2O and NH_3 on the vibrational, electronic, and energetic peculiarities of Ti^{IV} centers in TS-1 catalysts: a spectroscopic and computational study. J Phys Chem B 106:9892–9905
159. Tozzola G, Mantegazza MA, Ranghino G et al (1998) On the structure of the active site of Ti-silicalite in reactions with hydrogen peroxide: a vibrational and computational study. J Catal 179:64–71

160. Li C, Xiong G, Xin Q et al (1999) UV resonance Raman spectroscopic identification of titanium atoms in the framework of TS-1 zeolite. Angew Chem Int Ed 38:2220–2222
161. Bordiga S, Damin A, Bonino F et al (2002) The structure of the peroxo species in the TS-1 catalyst as investigated by resonant Raman spectroscopy. Angew Chem Int Ed 41:4734–4737
162. Bordiga S, Damin A, Bonino F et al (2003) Resonance Raman effects in TS-1: the structure of Ti(IV) species and reactivity towards H_2O, NH_3 and H_2O_2: an in situ study. Phys Chem Chem Phys 5:4390–4393
163. Guo Q, Feng ZC, Li GN et al (2013) Finding the "missing components" during the synthesis of TS-1 zeolite by UV resonance Raman spectroscopy. J Phys Chem C 117:2844–2848
164. Bordiga S, Coluccia S, Lamberti C et al (1994) XAFS study of Ti-silicalite – structure of framework Ti(IV) in the presence and absence of reactive molecules (H_2O, NH_3) and comparison with ultraviolet-visible and IR results. J Phys Chem 98:4125–4132
165. Geobaldo F, Bordiga S, Zecchina A et al (1992) DRS UV-Vis and EPR spectroscopy of hydroperoxo and superoxo complexes in titanium silicalite. Catal Lett 16:109–115
166. Bolis V, Bordiga S, Lamberti C et al (1999) A calorimetric, IR, XANES and EXAFS study of the adsorption of NH_3 on Ti-silicalite as a function of the sample pre-treatment. Microporous Mesoporous Mater 30:67–76
167. Bordiga S, Bonino F, Damin A et al (2007) Reactivity of Ti(IV) species hosted in TS-1 towards H_2O_2-H_2O solutions investigated by ab initio cluster and periodic approaches combined with experimental XANES and EXAFS data: a review and new highlights. Phys Chem Chem Phys 9:4854–4878
168. Gallo E, Bonino F, Swarbrick JC et al (2013) Preference towards five-coordination in Ti silicalite-1 upon molecular adsorption. ChemPhysChem 14:79–83
169. Gallo E, Lamberti C, Glatzel P (2011) Investigation of the valence electronic states of Ti(IV) in Ti silicalite-1 coupling X-ray emission spectroscopy and density functional calculations. Phys Chem Chem Phys 13:19409–19419
170. Zecchina A, Spoto G, Bordiga S et al (1991) Framework and extraframework Ti in titanium-silicalite – investigation by means of physical methods. In: Jacobs PA, Jaeger NI, Kubelkova L, Wichterlova B (eds) Zeolite chemistry and catalysis. Elsevier, Amsterdam, pp 251–258
171. On DT, LeNoc L, Bonneviot L (1996) Electron transfer bands of titanium sites in dehydrated silicalites and in TiO_2-SiO_2 gel. Chem Commun:299–300
172. Astorino E, Peri JB, Willey RJ et al (1995) Spectroscopic characterization of silicalite-1 and titanium silicalite-1. J Catal 157:482–500
173. Bonino F, Damin A, Ricchiardi G et al (2004) Ti-peroxo species in the TS-1/H_2O_2/H_2O system. J Phys Chem B 108:3573–3583
174. Zecchina A, Bordiga S, Lamberti C et al (1996) Structural characterization of Ti centres in Ti-silicalite and reaction mechanisms in cyclohexanone ammoximation. Catal Today 32:97–106
175. Blasco T, Camblor MA, Corma A et al (1993) The state of Ti in titanoaluminosilicates isomorphous with zeolite-beta. J Am Chem Soc 115:11806–11813
176. Su J, Xiong G, Zhou JC et al (2012) Amorphous Ti species in titanium silicalite-1: structural features, chemical properties, and inactivation with sulfosalt. J Catal 288:1–7
177. Xiong G, Cao YY, Guo ZD et al (2016) The roles of different titanium species in TS-1 zeolite in propylene epoxidation studied by in situ UV Raman spectroscopy. Phys Chem Chem Phys 18:190–196
178. Zecchina A, Spoto G, Bordiga S et al (1991) IR-spectra of CO adsorbed at low-temperature (77 K) on titanium-silicalite, H-ZSM5 and silicalite. In: Ohlmann G, Pfeifer H, Fricke R (eds) Catalysis and adsorption by zeolites. Elsevier, Amsterdam, pp 671–680
179. Munakata H, Oumi Y, Miyamoto A (2001) A DFT study on peroxo-complex in titanosilicate catalyst: hydrogen peroxide activation on titanosilicalite-1 catalyst and reaction mechanisms for catalytic olefin epoxidation and for hydroxylamine formation from ammonia. J Phys Chem B 105:3493–3501

180. Amtout A, Leonelli R (1995) Optical-properties of rutile near its fundamental-band gap. Phys Rev B 51:6842–6851
181. Tang H, Levy F, Berger H et al (1995) Urbach tail of anatase TiO_2. Phys Rev B 52:7771–7774
182. Zecchina A, Bordiga S, Spoto G et al (1992) Silicalite characterization. 2. IR spectroscopy of the interaction of CO with internal and external hydroxyl-groups. J Phys Chem 96:4991–4997
183. Zecchina A, Bordiga S, Spoto G et al (1992) Low-temperature Fourier-transform infrared investigation of the interaction of CO with nanosized ZSM5 and silicalite. J Chem Soc Faraday Trans 88:2959–2969
184. Li C, Xiong G, Liu JK et al (2001) Identifying framework titanium in TS-1 zeolite by UV resonance Raman spectroscopy. J Phys Chem B 105:2993–2997
185. Behrens P, Felsche J, Vetter S et al (1991) A XANES and EXAFS investigation of titanium silicalite. J Chem Soc Chem Commun:678–680
186. Schultz E, Ferrini C, Prins R (1992) X-ray absorption investigations on Ti-containing zeolites. Catal Lett 14:221–231
187. Pei S, Zajac GW, Kaduk JA et al (1993) Reinvestigation of titanium silicalite by X-ray-absorption spectroscopy – are the novel titanium sites real. Catal Lett 21:333–344
188. Bolis V, Bordiga S, Lamberti C et al (1999) Heterogeneity of framework Ti(IV) in Ti-silicalite as revealed by the adsorption of NH_3. Combined calorimetric and spectroscopic study. Langmuir 15:5753–5764
189. Lamberti C, Bordiga S, Arduino D et al (1998) Evidence of the presence of two different framework Ti(IV) species in Ti-silicalite-1 in vacuo conditions: an EXAFS and a photoluminescence study. J Phys Chem B 102:6382–6390
190. Prestipino C, Bonino F, Usseglio S et al (2004) Equilibria between peroxo and hydroperoxo species in the titanosilicates: an in situ high-resolution XANES investigation. ChemPhysChem 5:1799–1804
191. Ricchiardi G, de Man A, Sauer J (2000) The effect of hydration on structure and location of Ti-sites in Ti-silicalite catalysts. A computational study. Phys Chem Chem Phys 2:2195–2204
192. Tabacchi G, Gianotti E, Fois E et al (2007) Understanding the vibrational and electronic features of Ti(IV) sites in mesoporous silicas by integrated ab initio and spectroscopic investigations. J Phys Chem C 111:4946–4955
193. Lin WY, Frei H (2002) Photochemical and FT-IR probing of the active site of hydrogen peroxide in Ti silicalite sieve. J Am Chem Soc 124:9292–9298
194. Jacobs PT, Lin SM, Chen X (1998) US Patent 5785934A
195. Bellussi G, Perego C, Carati A et al (1994) Amorphous mesoporous silica-alumina with controlled pore size as acid catalysts. Stud Surf Sci Catal 84:85–92
196. Carati A, Ferraris G, Guidotti M et al (2003) Preparation and characterisation of mesoporous silica-alumina and silica-titania with a narrow pore size distribution. Catal Today 77:315–323
197. Guo Q, Sun KJ, Feng ZC et al (2012) A thorough investigation of the active titanium species in TS-1 zeolite by in situ UV resonance Raman spectroscopy. Chem Eur J 18:13854–13860
198. Pavel CC, Park SH, Dreier A et al (2006) Structural defects induced in ETS-10 by postsynthesis treatment with H_2O_2 solution. Chem Mater 18:3813–3820
199. Zuo Y, Liu M, Zhang T et al (2015) Role of pentahedrally coordinated titanium in titanium silicalite-1 in propene epoxidation. RSC Adv 5:17897–17904
200. Henderson GS, Liu X, Fleet ME (2002) A Ti L-edge X-ray absorption study of Ti-silicate glasses. Phys Chem Miner 29:32–42